technische universität
dortmund

Structure determination of silicon nano-ribbons by means of photoelectron spectroscopy and photoelectron diffraction

Dissertation

zur Erlangung des Doktorgrades

der Naturwissenschaften

(Dr. rer. nat.)

der Fakultät Physik

der Technischen Universität Dortmund

vorgelegt von

Philipp Espeter

geboren in Lünen

- 2017 -

1. Gutachter: Prof. Dr. Carsten Westphal
2. Gutachter: Prof. Dr. Dr. Wolfgang Rhode

Contents

1 Introduction

Low-dimensional materials are a recently discovered class of materials. They are described as material that can exist in crystalline configurations as thin as a single atom. In 2004 Novoselov and Geim, who are known to be the pioneers in the field of low-dimensional materials, reported the successful isolation of a sheet of carbon from a graphite sample [1]. This isolated sheet of carbon was as thin as a single atom and was called graphene, opening a new chapter of science in the field of condensed matter. They reported on extraordinary electronic, mechanical, and optical properties of graphene that were unrivalled by any bulk material or even thin films. Graphene revealed an ultra-high carrier mobility of roughly 200,000 $\frac{\mathrm{cm}^2}{\mathrm{Vs}}$ [2], an elastic modulus of about 1 TPa [3], and an optical transmission coefficient which is nearly constant for a large range of wavelengths [4], to name only a few. Thus, great expectations were associated with the discovery of graphene due to its outstanding properties, and consequently, the Nobel Prize was awarded jointly to Novoselov and Geim in 2010. The scientific community started exploring the unique properties and possible applications of graphene. Although diverse applications based on graphene-related materials are proposed, for example the use in touchscreens [5], micro-processing [6], or sensors [7, 8], only very few commercially available products exist so far for mainly two reasons: The extraordinary properties of graphene are solely reported for ideal and nearly defect-free sheets of graphene and there is less effort put in scientific studies focussing on commercially available graphene sheets. Further, due to its semi-metal properties like the vanishing bandgap graphene can not simply replace silicon, rather newly tailored concepts need to be developed [9]. These issues hampered the development of graphene based products and the search for alternative low-dimensional materials started. Within only a few years a variety of different low-dimensional structures were found [10–12]. Famous examples are so called van-der-Waals materials which possess a strong in-plane bonding but only weak

van-der-Waals forces in the out-of-plane direction. These van-der-Waals materials can be obtained by mechanical exfoliation, for instance from naturally occurring minerals. Transitionmetal-dichalcogenides are common examples composed of a transitionmetal atom like molybdenum or tungsten and two chalcogen atoms like sulfur, selenium, or tellurium. Another class of low-dimensional materials is built from group IV elements like silicon, germanium, and tin. Together with graphene these materials are the so-called Dirac materials. Their names are often adjusted with the ending 'ene' in the low-dimensional limit, for example silicene or germanene. In contrast to graphene which can be pulled off from the graphit bulk material, other Dirac materials of the fourth group need to be artificially synthesized. All of these low-dimensional materials have in common that they open new perspectives from a fundamental as well as technological point of view.

From the fundamental point of view, the discovery of low dimensional materials allows to study the substantial consequences due to confinement in the one- or two-dimensional limit. For instance, the semiconducting molybdenum disulfide changes from an indirect bandgap in the bulk structure to a direct bandgap in the limit of two dimensions [13]. Another example are nano-ribbons built of silicon. In bulk configuration silicon is a semiconductor, whereas it is supposed to reveal metallic behaviour in the one-dimensional limit [14]. Further, the actual existence of one- and two-dimensional materials enables the exploration of one- and two-dimensional electron gases (DEG) without artificially creating them by the stacking of semiconductors, or semiconductors and isolators [15].

From the technological point of view, low-dimensional materials offer functionalities as broad as sensing, energy, photonics, or electronics. Low-dimensional materials are inherently flexible, thus nearly every conceivable geometry can be covered with these materials. Flexible and transparent solar cells, for instance, have been successfully manufactured [16]. Especially in electronics the advantage of the potential of low-dimensional materials is of great interest. Recently, transistors were realized that use one-dimensional carbon-based nano-structures. This is possible due to the opening of a bandgap in one-dimensional carbon-based structures because of their lateral confinement of very few Ångstrom [17]. These transistors are smaller and have a higher normalized current density than state-of-the-art silicon technology [18]. According to Moore's law, silicon based transistors shrunk every 12 to 24 months. Since current transistors belong to the so called

14 nm semiconductor device fabrication node further shrinking is hardly possible. This is caused by quantum mechanical effects, for example the tunnel effect. Thus, new concepts including the use of the properties of low-dimensional materials need to be considered for meeting Moore's law in future [19, 20]. This is, for example, the development of spintronic or valleytronic devices that use the spin information of the electrons [19, 21]. For example, functionalized silicon nano-ribbons are reported to be a candidate in spintronic devices for efficient spin injection [22, 23]. Further, ultra-thin links made from one-dimensional structures with metallic properties for contacting shrunken electronic devices are conceivable.

This thesis is dedicated to the structure determination of nano-ribbons built of silicon atoms and their interaction with the substrate beneath. Silicon nano-ribbons are the one-dimensional representative of low-dimensional silicon structures. Their structure is a long-debated issue and a large number of more than 30 structure models are proposed [24–37]. Most of these proposed structure models are based on scanning tunnelling microscopy measurements [24, 26, 27, 32, 33] or *ab initio* calculations [25, 35, 36]. A complementary method for an encompassing evaluation of the validity of the proposed structure models is not reported yet. The precise structure determination is of highest interest since it is one of the main characteristics that influences electronic, mechanical, and optical properties. Theoretical calculations which are necessary for the development of prospective devices built of new materials are based on the structural characteristics of the used material. By determining the structure the effect on the electronic, mechanical, and optical properties can be predicted. For instance, several theoretical studies indicate an exceptional electronic and magnetic behavior for silicon nano-ribbons, depending on the assumed crystal structure [38–41].

Further, the interaction between the nano-ribbon and the substrate is of importance. Typically silver is a well suited template for the growth of silicon nano-ribbons, but not appropriate for electronic devices. Thus, the nano-ribbons need to be removed from the conducting silver template and transferred to a suitable insulating substrate. The transfer process is basically mediated by the chemical bonding and the interface between substrate and adsorbate, thus, the knowledge of the interaction will pave the way for developing effective transfer processes. Hiraoka *et al* reported on the decoupling of a silicon nano-ribbon from a silver substrate by a scanning tunnelling tip (STM) [42, 43]. The interaction between

the silver substrate and the impinging silicon atoms during the growth of silicon nano-ribbons was reported by Prevot *et al* recently [44]. They observed a displacement of silver atoms due to the impinging silicon atoms. Though, they could not provide information on the interaction between substrate and nano-ribbons in the equilibrium state.

In this thesis photoelectron-based techniques are utilized to clarify the local structure of silicon nano-ribbons and the bonding forces between the nano-ribbons and the silver substrate. Photoelectron spectroscopy (XPS) and photoelectron diffraction (XPD) are well-suited tools due to their surface sensitivity. XPS provides information regarding the chemical environment of emitting atoms, and XPD provides information on the local order of the emitting atoms. Both tools are proven to be excellently suited for addressing the above raised questions of structure determination and bonding forces [45–47] as proven by XPS and XPD studies providing structural information in the sub-Ångstrom range of two-dimensional materials like ordered organic molecules on metal surfaces [48, 49] and graphene on silicon carbide [50–53].

This thesis is structured into seven chapters. Following the introduction, a thematically classification of silicon nano-ribbons within the field of low-dimensional silicon structures is given. Primarily, this chapter deals with the different atomic structures that are proposed to describe the structure of silicon nano-ribbons. Since the substrate is of relevance for the formation of silicon nano-ribbons, further attention is given to the silver surface.

Chapter three deals with the theoretical principles of the photoelectric effect as it is the fundamental effect for both used methods, more precisely photoelectron spectroscopy and photoelectron diffraction. Particular consideration is given to the basics of photoelectron diffraction and the simulation of photoelectron diffraction patterns.

The experimental setup is described in chapter four. The characteristics of the used ultra-high vacuum (UHV) chamber, including all components which are necessary for the preparation and analysis of the system, are discussed. Further, two photon providing light-sources, Beamline 11 located at the synchrotron facility DELTA and a conventional X-ray tube, are introduced.

Chapter five deals with the process of preparation of the silver substrate. A detailed analysis of the silver surface based on LEED and XPS measurements is

performed since a clean and well reconstructed surface is of utmost importance for the growth of silicon nano-ribbons. Following, details of the growth process of the silicon nano-ribbons themselves are given. The growth of those nano-ribbons is verified by LEED, XPS, and UPS measurements since these tools are appropriate to evaluate the successful growth of silicon nano-ribbons.
In chapter six an encompassing analysis concerning the silicon and silver XPS measurements is performed providing first information about the bonding between the silver substrate and the adsorbed silicon nano-ribbons. This is followed by a discussion of the mentioned structure models by comparing simulated XPD pattern of a variety of structure models to the experimental XPD pattern.
The thesis is summarized in chapter seven and an outlook towards future studies is given.

2 Low-dimensional silicon structures

Silicon is the earth's second most abundant element with a percentage of about 28 % by mass. As a semiconductor it is probably best known for its application in integrated circuits but still, it has further applications in chemical industry as well as in metallurgy. Silicon is a chemical element with the atomic number 14 and classified in group IV within the periodic table, which is commonly known as the carbon group. The electronic configuration of silicon is $[\mathrm{Ne}]3\mathrm{s}^2 3\mathrm{p}^2$ what makes bulk silicon a famous representative for the sp^3 hybridization. Silicon is tetragonally coordinated with a nearest neighbour distance of $d_{\mathrm{nn}} = \frac{\sqrt{3} \times d}{4}$ Å and typically crystallizes in diamond structure with a lattice constant of $d = 5.43\,\text{Å}$, which can be described by two face-centred cubic structures shifted by half of the space diagonal. The unit cell of bulk silicon is illustrated in figure 2.1. Next to the diamond structure a lot of silicon allotropes are subject of current research, for example Si_{24} in zeolite structure forming six- and eight-membered rings [54], S_{136} in clathrate II structure forming five- and six-membered rings [55], or hexagonal silicon in lonsdalite structure [56]. Silicon allotropes in zeolite and clathrate II structure exist in bulk structure, whereas the hexagonal silicon in lonsdalite structure grows in so-called nano-wires. These nano-wires are several hundreds of nanometers in length but only a few nanometers in width [57, 58]. This limitation in width is a first step towards reducing the dimensionality of structures. However, the size of several nanometers is too large for observing a change of physical properties due to lateral confinement. Indeed, structures exist that are restricted to only a few Ångstrom in their lateral size, thus they are called low-dimensional materials. Low-dimensional materials are classified into three categories: 0D, 1D, and 2D materials. The 2D representative called silicene was the first proven low-dimensional material after graphene that consists only of one atom species. Silicene has been

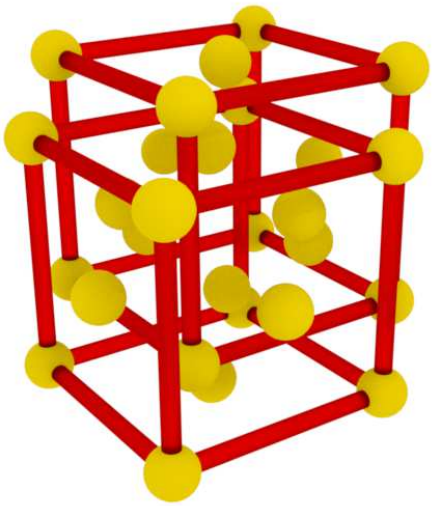

Figure 2.1: Unit cell of tetragonally coordinated silicon as found in diamond structure.

investigated from both the theoretical [59, 60] and the experimental [61] point of view already. Reports of the successful growth of silicene on a supporting silver substrate from five different groups were independently published as late as 2012 [62–66]. The structure of silicene can be easily described by a buckled sheet of hexagonally arranged silicon atoms [62]. Since then, the interpretation of the electronic band structure of silicene became a hot debate and a matter of current discussion. The origin of the linear bands resulting in a Dirac cone could not be explicitly assigned to either the substrate or the silicene itself [67].
Besides, the formation of the 0D representative, so-called nano-dots, was reported [24]. Nano-dots with lateral sizes of approximately $10 \times 15\,\text{Å}^2$ are observed on a Ag(110) surface [28]. Little is known about this configuration. No successful preparation of a sample solely covered with nano-dots is reported yet since nano-dots act as buildung blocks during the assembly of silicon nano-ribbons.
Consequently, the growth of silicon nano-ribbons, the 1D representative, on a Ag(110) substrate was reported [24]. Scanning tunnelling microscopy (STM) measurements showed perfectly aligned stripes when silicon was deposited onto a cleaned silver surface. Several works reported on the growth along the $[\bar{1}10]$ direction, the height of roughly 0.2 nm, the width of approximately 1.6 nm, and the length of about 30 nm [24, 68, 69]. Further, a $(\times 2)$-periodicity parallel and

a ($\times$5)-periodicity perpendicular to the [$\bar{1}$10] direction of the silver unit cell was observed by STM and low energy electron diffraction (LEED) [14].
Only little is known about the electronic properties of silicon nano-ribbons and their reactivity. There are first indications given by XPS and STM measurements that predict a metallic behaviour of silicon nano-ribbons [68, 70], and further, four new states near the Fermi level have been reported due to the lateral confinement within the narrow nano-ribbons [24, 71]. Though, a comprehensive analysis of the bandstructure is not reported yet.
First studies analyzing the reactivity of nano-ribbons towards oxygen and hydrogen exposure have been reported [72]. The oxidation process starts at the extremities of the nano-ribbons and develops along the elongated nano-ribbons [73]. The internal structure of the oxidized nano-ribbons changes, whereas the alignment along the [$\bar{1}$10] direction regarding the silver substrate is preserved. Further, it was observed that the oxidation process of silicon nano-ribbons starts at a higher oxygen exposure compared to the (7×7)-reconstructed Si(111) surface. More precisely, the reactivity towards oxidation is decreased by a factor of 10^4 [73]. In contrast, hydrogenation of the nano-ribbons due to molecular hydrogen exposure is not a site selective process [74, 75]. Covalent bonds between hydrogen and silicon atoms are formed leading to the destruction of the nano-ribbons into small nano-clusters. Nevertheless, depending on the careful selection of the deposited material, silicon nano-ribbons can be used as a template for the growth of perfectly aligned superstructures. For example, this was observed for the adsorption of 9,10-phenanthrenequinone, cobalt, or manganese deposition [22, 33, 76].
For an in-depth understanding of the above reported findings it is of highest importance to know the local order within the nano-ribbons and their position relative to the substrate. For this reason several theoretical and experimental works have been published addressing the question of the local order within the nano-ribbons. In contrast to sheets of silicene on silver, the structure of silicon nano-ribbons is still unknown. A multiplicity of proposed structure models exists which needs to be carefully evaluated. In total more than 30 different structure models are proposed. All of the so far reported structure models have been evaluated in this thesis. Since the silver substrate plays an important role during the nano-ribbon's growth it is discussed initially. Then, a selection of the proposed structure models is presented in more detail in section 2.2.

2.1 Crystal structure of Ag(110)

Silver is a chemical element with the atomic number 47 and classified in group eleven of the periodic table together with copper and gold. It belongs to the class of noble metals and exhibits one of the highest thermal and electrical conductivity due to its electron configuration $[Kr]4d^{10}5s^1$ [77]. Silver is a relatively inert metal, therefore main-contaminations from carbon or oxygen are only weakly bonded to the surface. The sole noteworthy strongly bonded contamination is sulfur causing a black tarnish when stored under ambient atmosphere.
Silver crystallizes in a face-centered cubic (fcc) structure as shown in figure 2.2 with eight atoms located in the corners of a cube, and six atoms located at the faces of the cube. Therefore, the coordination number is twelve, with a nearest neighbour distance of $d_{\mathrm{nn}} = \frac{a}{\sqrt{2}}$, and with a lattice constant of $a = 4.09\,\text{Å}$. From this infinitely extended fcc crystal structure a surface is generated by cutting the crystal along a lattice plane, typically determined by the Miller indices. The Miller indices are determined by three integer numbers (hkl) which are calculated by the reciprocal intersections of a spanned plane with the lattice vectors. Crystal directions are denoted as $[hkl]$. Consequently, $[hkl]$ is always perpendicular to (hkl). In figure 2.2 the plane characterized by the Miller indices (110) is shown in blue with the perpendicular crystal direction [110].

The result of cutting a perfect crystal in fcc structure along the (110) plane is shown in figure 2.3. Since the symmetry of bonding forces is broken at the surface due to the absence of neighbouring atoms in one direction, the modification of the equilibrium atom locations is likely. This modification is typically categorized as relaxation and reconstruction, thereby reconstruction is assigned to a change of periodicity parallel to the surface and relaxation is assigned to a change of periodicity normal to the surface. Strongly covalent bonded systems with highly oriented bondings form complex distortions at the surface. For example, semiconducting samples exhibit the tendency of saturating the dangling bonds generated by truncation of the bulk structure. This results in a shift of atom locations compared to the bulk position, or in the creation of missing rows. Metals on the other hand mostly rearrange in a simpler way since the undirected chemical bondings arise from the strongly delocalized metallic bonding. A relaxation of the topmost layers in metals can be explained by the transfer of electronic charge. Electric

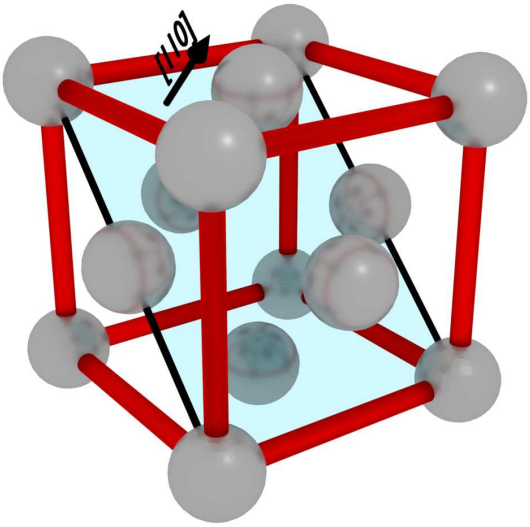

Figure 2.2: Unit cell of a face-centred cubic crystal structure with the (110) plane indicated by the blue area.

dipoles are formed at the surface due to smearing out of the electronic charge density. The electric field of this surfaces dipoles results in an electrostatic force on the metal ions. Thus, the topmost layers shift perpendicular to the surface plane. These layer shifts and the previously discussed surface reconstructions are mostly accompanied by surface defects like terraces, kinks, adatoms, vacancies, and ledges.
In the present case a (1×1)-reconstruction for Ag(110) is reported, meaning no shift or distortion parallel to the surface is observed. Indeed, relaxation of the two topmost layers was observed in previous studies by LEED measurements [78, 79].

2.2 Structure models of silicon nano-ribbons

The description of the silicon nano-ribbon structure models is a qualitative description for two reasons: The main reason is that most publications only report qualitative structure models and do not give precise information of bonding lengths, bonding distances, not to mention specific atom locations. The second reason is, that the characteristics of each evaluated structure model need to be identified in order to perform an encompassing XPD analysis. The necessity for

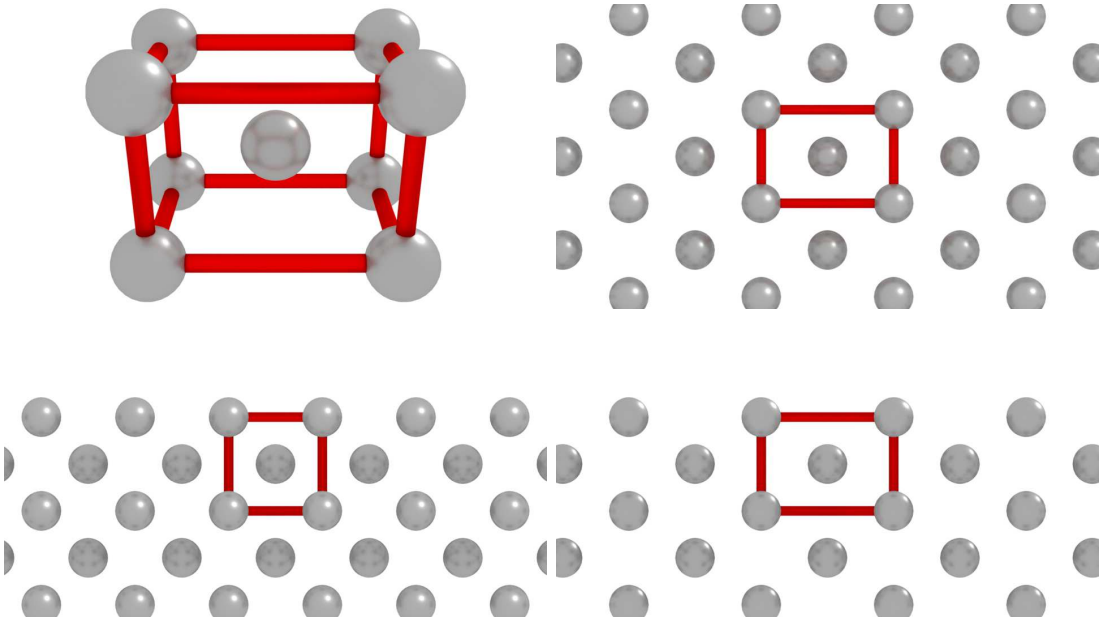

Figure 2.3: top row: Perspective view of the Ag(110) unit cell (left) and top view onto the Ag(110) surface in [110] direction (right). bottom row: Side view in [001] direction (left) and side view in [$\bar{1}$10] direction (right).

identification of the structural characteristics is presented in more detail in section 3.3.2.

Model proposed by Leandri

The first proposed structure model was reported by Leandri [24]. She proposed a hexagonal arrangement of the silicon atoms with zig-zag terminated edges as shown in figure 2.4 due to the perfect match between three unit cells of Si(111) orientation in [10$\bar{1}$] direction ($3 \times 3.84\,\text{Å} = 11.52\,\text{Å}$) and four unit cells of Ag(110) in [$\bar{1}$10] direction ($4 \times 2.89\,\text{Å} = 11.56\,\text{Å}$). The assumption of a hexagonal arrangement seems to be quite reasonable due to the analogy between silicon and carbon, since carbon nano-ribbons reveal a hexagonal structure [80]. Hence, a lot of proposed structure models are based on a hexagonal arrangement. Aufray *et al* performed density functional theory (DFT) calculations based the hexagonal structure proposed by Leandri. As a result they present a model that preserves the honeycomb structure but reveals strong corrugation along the [001] direction [26].

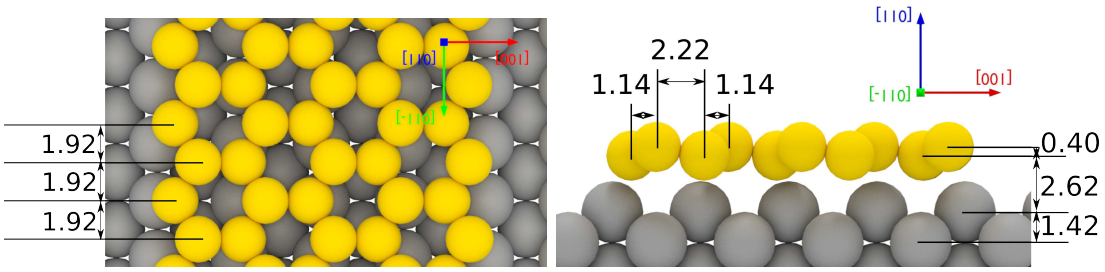

Figure 2.4: Hexagonal structure model as proposed by Leandri with zig-zag terminated edges [24]. Top view in [110] direction(left) and side view in [$\bar{1}$10] direction (right). Silicon atoms are displayed in yellow, silver atoms are displayed in grey.

Model proposed by He

The first theoretical approach for a structural determination was reported by He in 2006 [25]. He reported an *ab initio* study based on the determination of the adsorption energy, while taking the observed (5 × 2)-periodicity regarding the silver substrate into account. He calculated the adsorption energy for 18 different structures. He concluded, that twelve silicon atoms stacked into two layers within a unit cell are the most stable structure. The bottom layer consists of eight atoms that are placed in the hollow sites of of the silver substrate. The top layer consists of four atoms that build silicon dimers that are oriented perpendicular to the [$\bar{1}$10] direction regarding the silver substrate. A structure model is shown in figure 2.5.

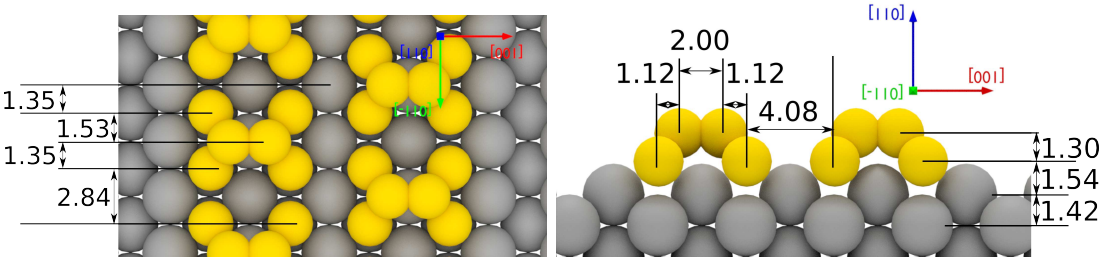

Figure 2.5: Most stable structure model as proposed be He [25]. Top view in [110] direction(left) and side view in [$\bar{1}$10] direction (right).

Model proposed by Tchalala

Next to the honeycomb based structure models given by Leandri and Aufray *et al*, further honeycomb based structure models are reported that are rotated by 30° regarding the models proposed by Leandri and Aufray *et al*. This results in an arm-chair terminated honeycomb structure as shown in figure 2.6. Two unit cells of Ag(110) in $[\bar{1}10]$ direction ($2 \times 2.89\,\text{Å} = 5.78\,\text{Å}$) perfectly match three unit cells of silicon (111) in $[\bar{2}11]$ direction ($3 \times 1.86\,\text{Å} = 5.58\,\text{Å}$) as reported by several authors [31, 32].

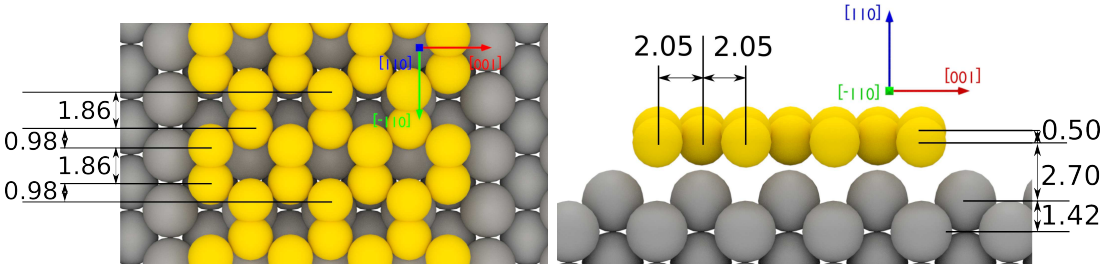

Figure 2.6: Hexagonal structure model as proposed by Tchalala *et al* with arm-chair terminated edges [32]. Top view in [110] direction(left) and side view in $[\bar{1}10]$ direction (right).

Model proposed by Hogan

Further proposed structure models are modifications of the models reported by He [33, 81], and modifications of the arm-chair and zig-zag terminated honeycomb structures [34]. Then, Bernard *et al* reported on their grazing incidence X-ray diffraction study predicting the formation of a two missing row reconstruction beneath the nano-ribbons [29]. As a consequence, even more complex structures are proposed [27, 30]. For example Hogan *et al* predicted a zig-zag chain of silicon atoms bonded to silicon dimers located within the missing row reconstruction of the silver substrate as shown in figure 2.7 [27].

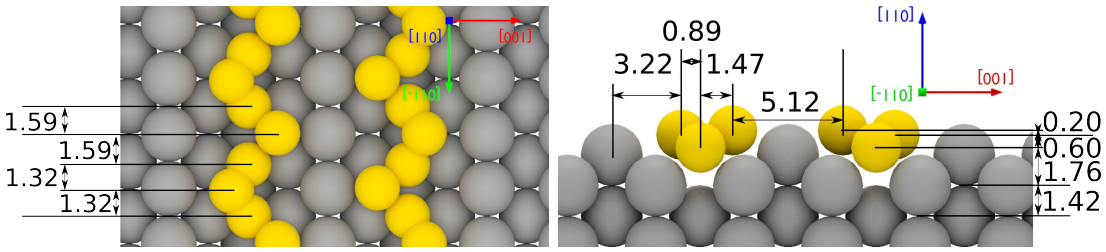

Figure 2.7: Structure model as proposed by Hogan *et al* [27]. Top view in [110] direction(left) and side view in [$\bar{1}$10] direction (right).

Model proposed by Prevot and Cerda

The latest approach for describing the structure of silicon nano-ribbons on Ag(110) is reported by Cerda *et al* [28] and Prevot *et al* [37]. They propose a structure model consisting of two buckled pentagonal silicon chains stabilized within two missing rows. A structure model is shown in figure 2.8.

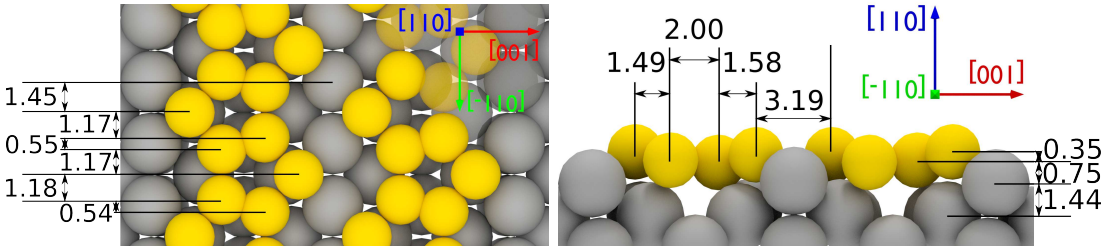

Figure 2.8: Pentagonal structure model as proposed by Prevot *et al* [37]. Top view in [110] direction(left) and side view in [$\bar{1}$10] direction (right) [82].

In total, there are more than 30 structure models predicted. Since almost all of them are solely based on one experimental technique, or at least only based on theoretical calculations, an encompassing evaluation has to be performed.

3 Theoretical principles

Surface sensitive tools are necessary for the analysis of the structural properties of silicon nano-ribbons on a Ag(110) substrate. X-ray photoelectron spectroscopy (XPS) and X-ray photoelectron diffraction (XPD) offer the requested specification of surface sensitivity and are versatile tools based on the photoelectric effect. The fundamentals of these methods are described in this section, and therein, the individual strengths of providing chemical as well as structural information are pointed out.

3.1 Photoelectric effect

The first experimental finding that can be attributed to the photoelectric effect was reported by Alexandre Edmond Becquerel in 1839. He documented an electrical current flowing between two electrodes in a electrolytic solution by illuminating one electrode with ultraviolet light [83, 84]. Subsequently, systematic studies exploring the effects of illuminating metal electrodes by ultraviolet light were conducted by Heinrich Hertz and Wilhelm Hallwachs in 1887 [85–87]. They observed the change of charge density at the metal electrode induced by irradiation with ultraviolet light. Finally, after considering the pioneering works from Philipp Lenard [88] and Max Planck [89, 90], the theoretical description of the photoelectric effect was given by Albert Einstein in 1905 [91]. In 1914 Milikan proved Einsteins theory by determining the Planck constant via a retarding field experiment [92].
The photoelectric effect describes the interaction between a photon and a bonded electron. The photon is described as a particle with an energy $E_{\mathrm{Photon}} = h\nu$ and a momentum $p = \hbar k$. The momentum of the incoming photon can be neglected

for the following considerations due to its low value. In case the photon energy $h\nu$ is larger than the work function Φ_S and binding energy of an electron E_bin, i.e. $h\nu \geq \Phi_\mathrm{S} + E_\mathrm{bin}$, a core-level electron can be ejected due to energy transfer from the photon to the bonded electron. The work function Φ_S defines an element specific energy distance between the Fermi level E_F and the vacuum level E_vac, and the binding energy is defined by the energy distance between the Fermi level and the initial electron orbital. The ejected electrons are referred to as photoelectrons. Since a photon can transfer only its entire energy the photoelectric effect can be described by the photoelectric equation

$$h\nu = E_\mathrm{kin} + E_\mathrm{bin} + \Phi_S \tag{3.1}$$

where E_kin describes the kinetic energy of the photoelectron. In case the photon energy of an incoming photon is larger than the work function Φ_S and smaller than the binding energy of the highest core-level E_bin, i.e. $\Phi_\mathrm{S} \leq h\nu \leq E_\mathrm{bin}$, an electron from the valence band can be ejected. If the photon energy is larger than the binding energy E_bin but smaller than the binding energy and the work function $E_\mathrm{bin} + \Phi_\mathrm{S}$, i.e. $E_\mathrm{bin} \leq h\nu \leq E_\mathrm{bin} + \Phi_\mathrm{S}$, an electron can be excited from a bonded state into the conduction band or from the valence band into the continuum. Since the photoelectric effect leaves unoccupied hole-states relaxation effects occur. The typical lifetime τ of such a hole-state is about $\tau = 1\,\mathrm{fs}$ [93]. Weaker bonded electrons from the initial energy level E_i relax into the unoccupied hole-state E_f. The energy difference $E_\mathrm{f} - E_\mathrm{i}$ can be released in either of two different ways, namely the Auger-Meitner effect [94, 95] or fluorescence [96, 97].
For the Auger-Meitner effect the energy difference $E_\mathrm{f} - E_\mathrm{i}$ is transferred to another bonded electron which is either lifted into the valence band or ejected into the vacuum. The ejected electrons due to the Auger-Meitner effect are termed Auger-electrons. Their kinetic energy $E_{\mathrm{Auger,\,kin}}$ only depends on the involved core-levels

$$E_{\mathrm{Auger,\,kin}} = E_\mathrm{f} - E_\mathrm{i} - E_{\mathrm{Auger,\,k}}, \tag{3.2}$$

where $E_{\mathrm{Auger,\,k}}$ denotes the initial binding energy of the emitted Auger-electron. The second possible relaxation process is fluorescence. In this relaxation process

the energy difference $E_\mathrm{f} - E_\mathrm{i}$ is emitted by fluorescence radiation as a photon

$$h\nu_\mathrm{fluorescence} = E_\mathrm{f} - E_\mathrm{i}. \tag{3.3}$$

Both of these processes occur parallel. The probability of the individual processes depends on the atomic number of the involved elements, with the Auger-Meitner effect dominating for elements with atomic numbers $Z \leq 30$, and fluorescence dominating for atomic numbers of $Z \geq 60$. The scheme of photoemission and its corresponding relaxation processes is displayed in figure 3.1.

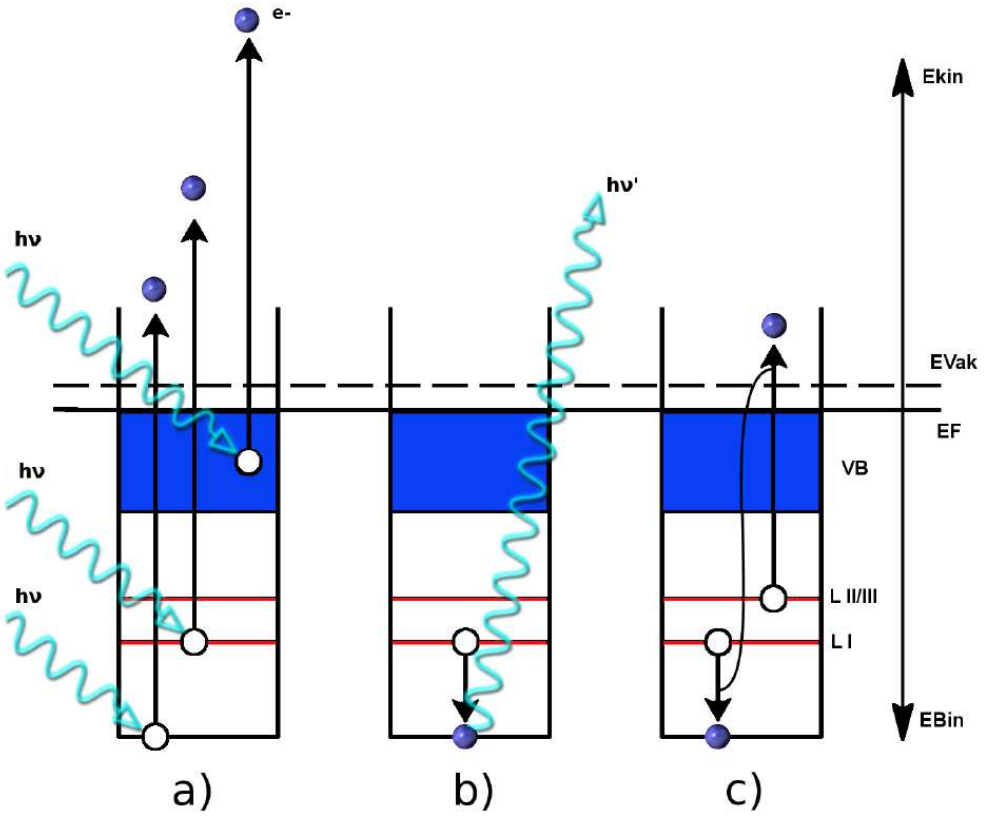

Figure 3.1: Scheme of the photoemission (a), Auger-Meitner (b), and fluorescence (c) relaxation [98].

3.2 Photoelectron spectroscopy

Photoelectron spectroscopy is a versatile tool for the analysis of the elemental composition of a solid and the existent chemical bondings. Depending on the energy of the incoming photons photoelectron spectroscopy can historically be subdivided in UPS (Ultraviolet Photoelectron Spectroscopy) for $5 < E_{\mathrm{Ph}} < 50\,\mathrm{eV}$, XPS (X-ray Photoelectron Spectroscopy) for $100 < E_{\mathrm{Ph}} < 1500\,\mathrm{eV}$, and HAXPES (Hard X-ray Photoelectron Spectroscopy) for $1500\,\mathrm{eV} < E_{\mathrm{Ph}}$. In photoelectron spectroscopy the intensity of electrons is recorded depending on their kinetic energy after excitation with a x-ray source.
There is a certain probability that an incoming photon generates a photoelectron. This probability is termed the differential cross section $\frac{\mathrm{d}\sigma}{\mathrm{d}\Omega}$ and depends on the investigated element, orbital and photon energy.
While travelling through the crystal the photoelectrons get scattered at the remaining electron system. Elastic scattering without energy transfer and inelastic scattering causing a loss in kinetic energy of the photoelectron occur. The latter one results in attenuation of the intensity of photoelectrons, described by the inelastic mean free path (IMFP) $\lambda_m(E_{\mathrm{kin}})$. The IMFP describes the distance an electron beam travelled before it is attenuated to $1/e$ of its initial intensity. The probability for an inelastic scattering event strongly depends on the kinetic energy of the electron and weakly depends on the element. Thus, due to simplicity reasons the so called "universal curve" was assumed to describe the inelastic mean free path in the early times of photoelectron spectroscopy [99]. Today, the more sophisticated "TPP2M" formula is utilized to determine the IMFP [100]. The "TPP2M" formula was deduced by Tanuma, Powell, and Penn from the Bethe-Bloch equation corrected by two modifications by Inokuti and Ashley who took additional loss mechanisms of electrons compared to heavy charged particles into account [101–103]. The IMFP for non-relativistic electrons is given by

$$\lambda_m(E_{\mathrm{kin}}) = \frac{E_{\mathrm{kin}}}{E_{\mathrm{p}}\left[\beta \ln(\gamma E_{\mathrm{kin}}) - (C/E_{\mathrm{kin}}) + (D/E_{\mathrm{kin}}^2)\right]}. \tag{3.4}$$

where β, γ, C, and D are determined by empirical expressions, and E_{p} is the free electron plasmon energy. Two excitation processes exist that characterize the shape of the IMFP. Inelastic electron-electron scattering generating secondary

electrons is the dominant contribution to the IMFP below a kinetic energy of 50 eV. Above 70 eV, the IMFP is limited mainly by the quantized excitations of plasmons. These plasmons need to be distinguished into bulk and surface plasmons and their excitation energy is typically of the order of several eV [104, 105]. The IMFPs for different materials, including silicon and silver, are shown in figure 3.2. Despite small differences in the shape of the IMFP for various materials, the basic shape of the IMFP remains almost unchanged. The minimum value of the IMFP is about 5 Å for kinetic energies between 30 eV and 100 eV, and thus only photoelectrons from the topmost 5 Å to 10 Å can escape into the vacuum. This very low IMFP makes photoelectron spectroscopy and diffraction very surface sensitive techniques, and subsequently well suited for the analysis of low-dimensional structures that present themselves as a surface.
The effect of elastic scattering on the photoelectron intensity will be discussed in chapter 3.3 with respect to photoelectron diffraction.

A typical XPS survey spectrum is shown in figure 3.3. It is recorded at a kinetic

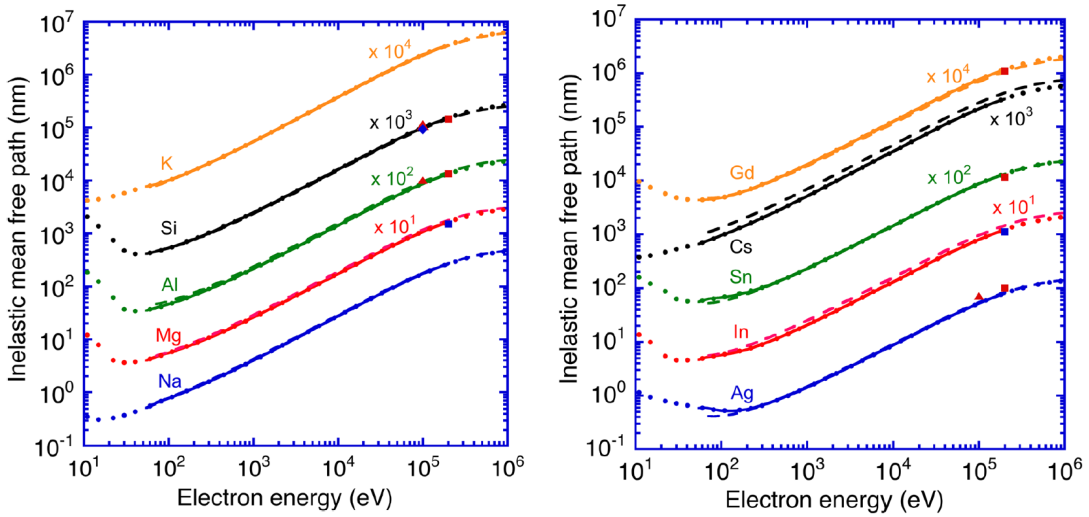

Figure 3.2: Inelastic mean free path in nm as a function of energy above the fermi level as calculated by the "TPP2M" formula. The solid line results from a least square fit of the modified Bethe-Bloch equation, adopted from [100].

energy of $h\nu = 650$ eV under normal emission. The Ag 3d, Ag 4s, and Ag 4p core-levels are indicated as well as the Ag Auger signals. A detailed analysis procedure

containing background subtraction, line shape, shifting of core-level signals due to chemical bonding, and splitting of core-level signals due to spin-orbit coupling is discussed below.

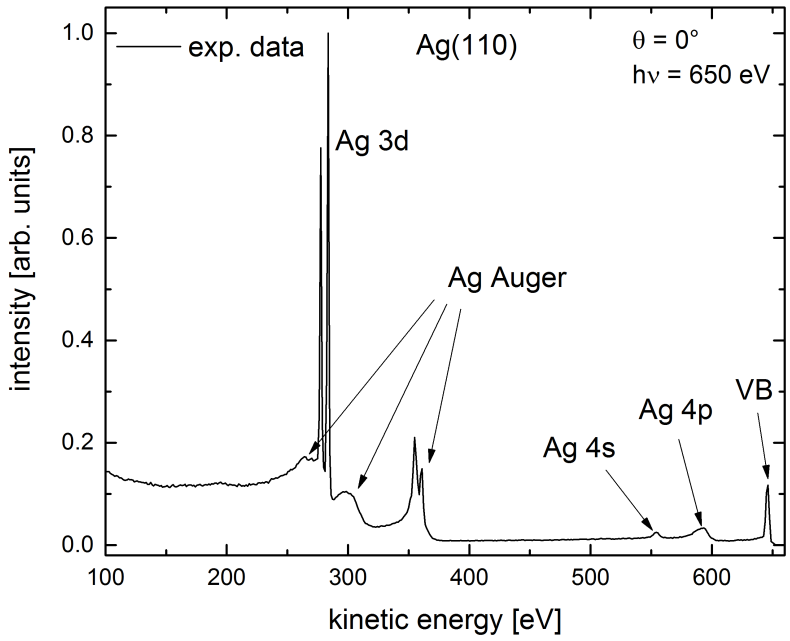

Figure 3.3: Survey spectrum of a sputter-cleaned Ag(110) sample. All characteristic features of the spectrum are labelled.

3.2.1 Background

While propagating through the sample the photoelectrons get inelastically scattered as described above. This causes a continuous background contribution to the XPS spectrum. The excitation of secondary electrons generates a continuous background signal and the excitation of plasmons generate a discrete background signal. The discrete background signal originating from the plasmon excitations can be removed by peak fitting, whereas the removal of the continuous background signal remains challenging. There are mainly two different possibilities of background subtraction. One possibility is applying the so-called Shirley background.

The Shirley background B_{S} is a deterministic approach based on an uniform energy loss function for the background removal [106].
The second possible approach of background determination is the so-called Tougaard background. The determination of the Tougaard background B_{T} is based on the previously mentioned IMFP $\lambda(E)$, see equation (3.4), and the assumption of a non-uniform energy loss cross section $K(E, T = E - E')$ where E denotes the kinetic energy of an electron and T the energy loss per path length [107]. Thereby, the background can now be calculated by

$$B_{\mathrm{T}}(E) = \lambda(E) \int_{E}^{\infty} K(E', E' - E) \times I(E') \, \mathrm{d}E'. \tag{3.5}$$

Analyzing typical shapes of the functions $\lambda(E)$ and $K(E, T)$ show that each of them strongly depends on E. Still, the product $\lambda(E) \times K(E, T)$ is rather independent of E [107] and can be approximated by the universal inelastic scattering cross section

$$\lambda(E) \times K(E, T) = \frac{BT}{\left(C + C'T^2\right)^2 + DT^2} \tag{3.6}$$

with well known parameters B, C, C', D. Substituting $K(E, T)$ in equation (3.5) [108] yields

$$B_{\mathrm{T}}(E) = \lambda(E) \int_{E}^{\infty} \frac{BT}{\left(C + C'T^2\right)^2 + DT^2} \times \frac{1}{\lambda(E')} \, \mathrm{d}E'. \tag{3.7}$$

Since the Tougaard background is advantageous for asymmetric photoelectron lines, the background subtraction is performed by applying the Tougaard background instead of the Shirley background [109, 110].

3.2.2 Line shape

The line shape observed for XPS-signals is a convolution of different types of contributions. There is a Lorentzian contribution due to the finite lifetime of the generated core-hole, as well as a Gaussian contribution $G(E, \sigma_{\mathrm{G}})$ with σ_{G} denoting the full width at half maximum (FWHM) of the Gaussian profile G due to instrumental influences like the x-ray line shape and spectrometer properties [111, 112]. If the experimental line shape reveals an asymmetry, a contribution described by a Doniach-Sunjic profile $D(E, \Gamma, \alpha, E_{\mathrm{c}})$ has to be considered instead of the Lorentzian-profile [111, 113]:

$$D(E, \sigma_D, \alpha, E_{\mathrm{c}}) = \frac{\cos\left[\frac{\pi\alpha}{2} + (1-\alpha)\arctan\left(\frac{E-E_{\mathrm{c}}}{\Gamma}\right)\right]}{((E-E_{\mathrm{c}})^2 + \Gamma^2)^{(1-\alpha)/2}}. \tag{3.8}$$

Here, Γ corresponds to the FWHM of the Doniach-Sunjic profile, α to the asymmetry parameter and E_{c} is related to the kinetic energy location. Asymmetric line shapes are typically observed if metals with a high density of occupied states below the fermi level and unoccupied states above the fermi level are probed. If a core-hole is generated by photoemission the electrons from the conduction band screen the core-hole. In detail, screening describes the excitation of an electron-hole pair within the conduction band. This excitation is induced by the spontaneously switched-on local potential of the generated core-hole. The matrix element M describing the electron-hole excitation is approximately proportional to $\frac{1}{\Delta E}$, i.e. $M \propto \frac{1}{\Delta E}$, and thus M is the stronger, the smaller the energy transfer ΔE. Hence, the screening leads to a tail at the low kinetic energy side [93, 112, 113]. Since the Doniach-Sunjic profile converts into a Lorentzian-profile for an asymmetry parameter $\alpha = 0$ it represents the more general approach for describing the line shape [105]. Consequently, the line shape $f(E)$ with its amplitude A is determined by

$$f(E) = A \cdot (G(\sigma_G) * D(\Gamma, \alpha, E_c))\,(E). \tag{3.9}$$

3.2.3 Chemical shift

The analysis of the kinetic energy of the photoelectrons emitted from the solid allows the determination of their binding energies. The binding energy is characteristic for an orbital and an element. The difference in electronegativity between bonding partners affects the binding energy. The more electronegative bonding partner attracts the involved valence electrons and in turn the electron density is more localized at the more electronegative atom. Accordingly, its relative atomic number decreases and the binding energy is decreased, too. In contrast, the relative atomic number of the less electronegative bonding partner is increased, as well as its binding energy is increased. The first clear evidence for a chemical shift was observed within the S 2p core-level signal from sodium-thiosulfate [114]. The most famous example of a chemical shift in XPS signals was given by Nobel laureates K. Siegbahn analyzing the chemical shift of the C1s signal in ethyltrifluoroacetate [115, 116] as shown in figure 3.4. The binding energy of the carbon atoms with three hydrogen bonding partners is $E_{\text{bin, CH3}} = 291.2\,\text{eV}$, while the binding energy of the carbon atom with three fluorine bonding partners is $E_{\text{bin, CF3}} = 299.4\,\text{eV}$. This large energy shift is due to the large difference in electronegativity between hydrogen and fluorine. If the difference in electronegative is small the resulting energy shift of the binding energy is small. This makes it more difficult to separate the individual components in an XPS spectrum. Still, analysis of the chemical shift yields unique information concerning distributions of chemical and structural sites near the surface [117].

3.2.4 Multiplet splitting

Photoelectron lines split into multiplets caused by the interaction of the spin s of the electron and the orbital angular momentum l [118]. This effect is called spin-orbit coupling (SOC) and an initial state phenomenon. The spin $s = \pm\frac{1}{2}$ can be either parallel or anti-parallel regarding the orbital angular momentum l resulting in a total angular momentum $j = l \pm s$. As an example, the six electrons from a p-type subshell are split into $p_{1/2}$ with $m_J = \pm\frac{1}{2}$ and $p_{3/2}$ with $m_J = \pm\frac{3}{2}, \pm\frac{1}{2}$.

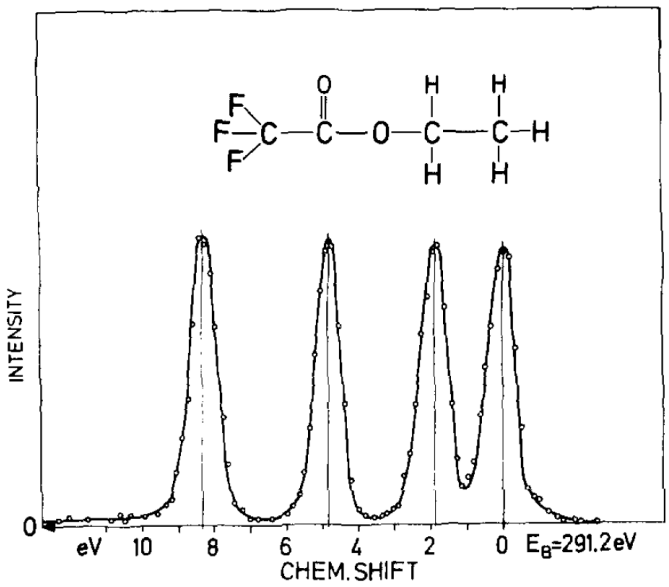

Figure 3.4: High-resolution XPS spectrum of the C 1s core-level of gaseous ethyltrifluoroacetate [115,116]. Four well separated chemically shifted components of the C 1s core-level are visible, according to four carbon atoms with each having different bonding partners.

There is no spin-orbit coupling in the case of $l = 0$ [119]. The ratio of the two distinct spin-orbit components is determined by their degree of degeneracy

$$\frac{I_{j=l+s}}{I_{j=l-s}} = \frac{2(j = l + s) + 1}{2(j = l - s) + 1}. \tag{3.10}$$

The emission of a photoelectron from a core-level leaves an unfilled subshell. Thus, due to changes in the angular momentum of the remaining electron system there might exist more than one final state. This results in an additional splitting in an XPS spectrum [117]. However, this final-state splitting can be neglected while probing silicon and silver [120, 121].

3.3 Photoelectron diffraction

Photoelectron diffraction is a powerful technique for gaining structural information from surfaces and interfaces. It is based on photoelectron spectroscopy and

developed from a phenomenon that was observed by Siegbahn *et al* for the first time. They reported that the intensity of electrons expelled from core-levels of a NaCl single crystal shows a strong angular dependence [122]. Further essential works report on the observation of the phenomenon on metal single crystals and adsorbates on surfaces [123–126].

The generated photoelectrons can get elastically scattered at the neighbouring atoms and the evolved diffraction pattern can be recorded by an angular resolved measurement. In figure 3.5 the basic process of photoelectron diffraction is schematically shown. The local environment of the emitting atoms can be concluded from such a diffraction pattern [45, 127–129].

A photoelectron excited from a localized core-level state propagates as a primary

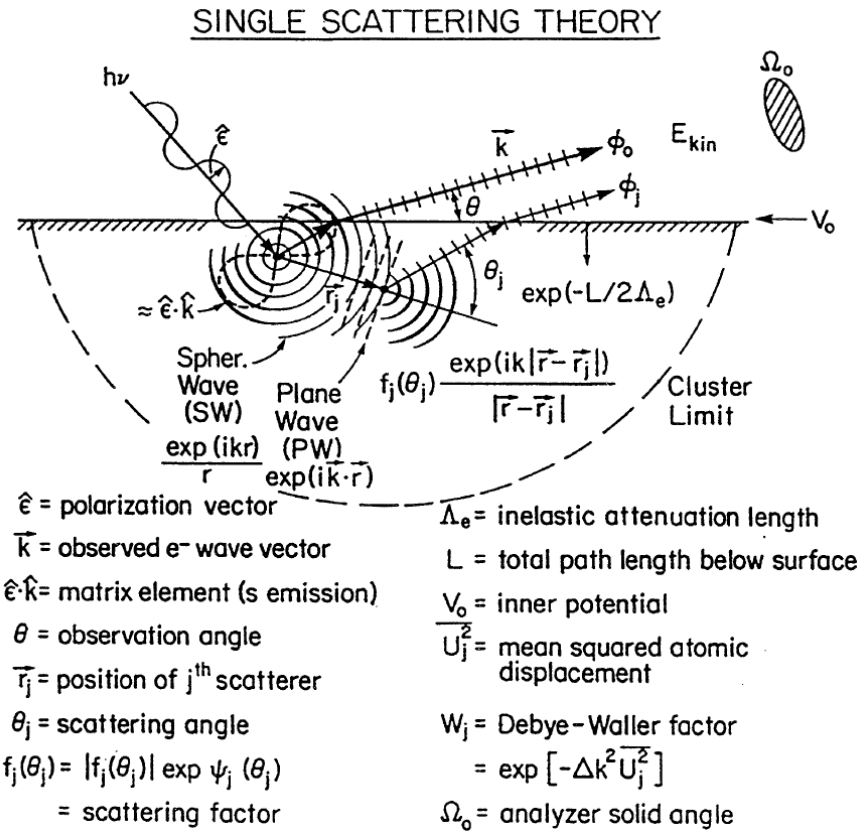

Figure 3.5: Illustration of the photoelectron diffraction process based on the simplified assumption of single-scattering. Various essential variables are indicated [47].

spherical wave through the crystal. The amplitude of the electron wave decreases

with the inverse distance from the emitting atom:

$$\Psi_0(\vec{r}) \propto \frac{e^{ik|\vec{r}|}}{|\vec{r}|}. \tag{3.11}$$

Due to this proportionality XPD is highly sensitive for the short-range order and less sensitive for the long-range order [45, 47]. The primary wave gets scattered at neighbouring atoms generating secondary waves. The primary and all generated secondary waves interfere due to their locked phase and locked amplitude. This interference pattern can be detected. Though, the phase information gets lost during the recording process due to squaring the final wave-function [127]

$$I(\vec{k}) = \left| \Psi_0(\vec{k}) + \sum_l \Psi_l(\vec{k}) \right|^2, \tag{3.12}$$

where $I(\vec{k})$ accounts for the measured intensity dependent on direction and energy, Ψ_0 accounts for the primary electron wave, and Ψ_l accounts for all secondary scattered electron waves. As shown in equation (3.12), intensity modulations can be observed for the variation of the excitation energy $h\nu$ and thus the kinetic energy of the expelled photoelectrons, as well as for variation of the detection angle [45, 128]. In the following the focus will solely be on the angle-scanned mode.

For a reliable analysis of a diffraction pattern effects of multiple-scattering have to be considered. Though, due to simplicity reasons, the theory of photoelectron diffraction is described by a single-scattering formalism.

The primary and secondary electron waves from equation (3.12) are given more explicitly by [127]

$$I(\vec{k}) \propto \left| (\hat{\epsilon} \times \hat{k})\, e^{-\frac{L_0}{2\lambda}} + \sum_l \frac{(\hat{\epsilon} \times \hat{r_l})}{r_l} f_l(\Theta_l, k)\, e^{\Phi(\Theta_l,k)} W_l\, e^{-\frac{L_l}{2\lambda}}\, e^{ikr_l(1-\cos(\Theta_l))} \right|^2. \tag{3.13}$$

In equation (3.13) $\hat{\epsilon}$ denotes the polarization vector of the incoming photons, $(\hat{\epsilon} \times \hat{k})$ and $(\hat{\epsilon} \times \hat{r_l})$ denote the dipole-matrix element in direction of $\vec{k}$ and $\vec{r_l}$, respectively.

Attenuation of the electron wave due to inelastic scattering is introduced by the exponential decay factor $e^{-\frac{L_l}{2\lambda}}$ with L_l corresponding to the entire covered distance below the surface and λ corresponding to the IMFP. Attenuation of the interference pattern due to vibrational effects is introduced by the Debye-Waller factor W_l. The complex scattering factor consists of an amplitude $f_l(\Theta_l, k)$ and a phase shift $\Phi(\Theta_l, k)$ as shown in figure 3.6. Finally, the phase shift due to geometric path length differences is introduced by the factor $e^{ikr_l(1-\cos(\Theta_l))}$. The photoelectrons

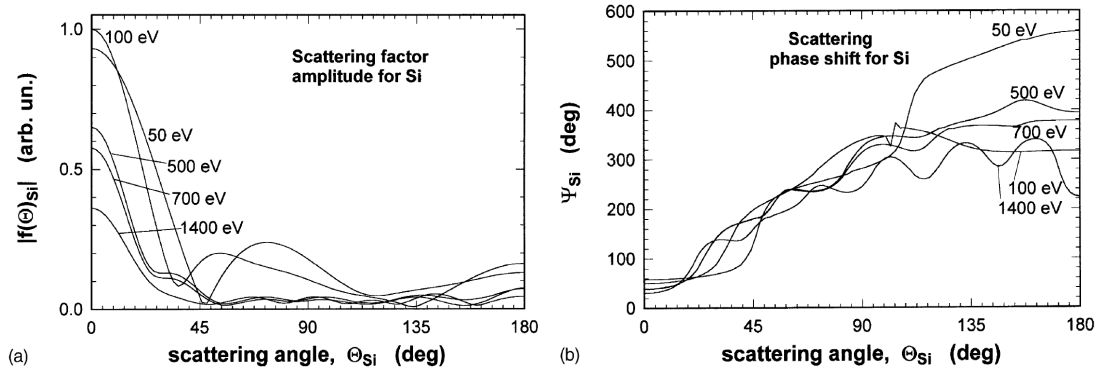

Figure 3.6: Scattering factor amplitude (a) and phase shift (b) as an function of the scattering angle for various kinetic energies [45].

suffer diffraction while escaping from the solid into the vacuum due to the inner potential of the solid V_0 [130, 131]:

$$\frac{\sin(\Theta_{\text{solid}})}{\sin(\Theta_{\text{vacuum}})} = \sqrt{\frac{E_{\text{kin}} + V_0}{E_{\text{kin}}}}. \tag{3.14}$$

In equation (3.14) Θ_{vacuum} denotes the polar angle inside the crystal and Θ_{vacuum} denotes the polar angle after escaping the crystal.
In figure 3.6 the scattering factor amplitude and phase of a silicon scatterer are shown. It is obvious that the kinetic energy of the photoelectron is of highest significance for the resulting diffraction pattern. For high kinetic energies $E_{\text{kin}} > 500\,\text{eV}$ the scattering factor amplitude is strongly focused at low polar angles around $\Theta_l = 0$. This results in a strongly forward focussed diffraction pattern with distinct maxima along linear ordered chains of atoms. For large inelastic mean free paths as it is the case for kinetic energies $E_{\text{kin}} > 500\,\text{eV}$ a linear atomic chain can be found in multiple crystal directions. This results in forward focused in-

tensity maxima in these distinct crystal directions. Due to the large number of linear atomic chains in a single crystal some of the forward focussed intensity maxima merge into line-type maxima. These line-type maxima are called Kickuchi lines [132–134]. These maxima provide information about structural properties of the sample between the emitter and the detector and yield information about the orientation of the sample. In contrast, for lower kinetic energies $E_{\mathrm{kin}} < 300\,\mathrm{eV}$ the scattering factor amplitude is more complex including a strong contribution in backward direction [135,136]. This results in a diffraction pattern that provides additional information about the structure behind the emitting atom.
Since photoelectron diffraction is based on photoelectron spectroscopy it is sensitive to both different emitting elements in one sample and differently bonded emitters from the same element due to the chemical shift. Thus, photoelectron diffraction is a versatile tool for probing the local environment of surfaces as well as interfaces.

3.3.1 Data treatment

This work solely focusses on the angle-scanned mode. In this case the energy of the incoming photons is kept constant. Recording the photoelectron intensities in the hemisphere above the sample at various polar angles Θ and azimuthal angles φ, more accurately polar angles $0° \leq \Theta \leq 80°$ and azimuthal angles $0° \leq \varphi < 360°$, result in a XPD pattern. Therein, the polar angle Θ is defined as the angle between the surface normal and the direction to the spectrometer. The azimuthal angle φ describes the rotation of the sample around the surface normal. The step widths of the polar and azimuthal angle while scanning the hemisphere are by default $\Delta\Theta = 2°$ and $\Delta\varphi = 1.8°$, respectively. As a result a typical XPD pattern consists of about 7200 individual XPS spectra.
The transformation of the 7200 individual XPS spectra into one XPD pattern is as follows: first, the background signal of each spectrum has to be determined by the procedure given in section 3.2.1. Then, the intensities are normalized by a polynomial function that corresponds to the number of incoming photons. Second, the intensities are determined by the enveloped peak area. In order to compare the experimental to the simulated XPD pattern it is necessary to normalize each.

For normalization the anisotropy function is introduced:

$$\chi(\Theta, \varphi) = \frac{I(\Theta, \varphi) - I(\Theta)}{I(\Theta)}, \tag{3.15}$$

where $I(\Theta, \varphi)$ denotes the measured intensity at (Θ, φ), and $I(\Theta)$ denotes the averaged intensity for one polar angle, Θ. For a more demonstrative presentation the anisotropy is displayed in a grey scale polar plot. In case the recorded spectrum shows rotational and/or mirror symmetry, a symmetry averaged diffraction pattern is calculated to reduce statistical fluctuations. Last, the diffraction pattern is blurred by a gaussian distribution. This serves as a low-pass filter and statistical errors can be removed [98]. Every processing step is displayed in figure 3.7 using the example of a Si 2p diffraction pattern.

As shown in section 3.2.3 a core-level signal of one element species can consist

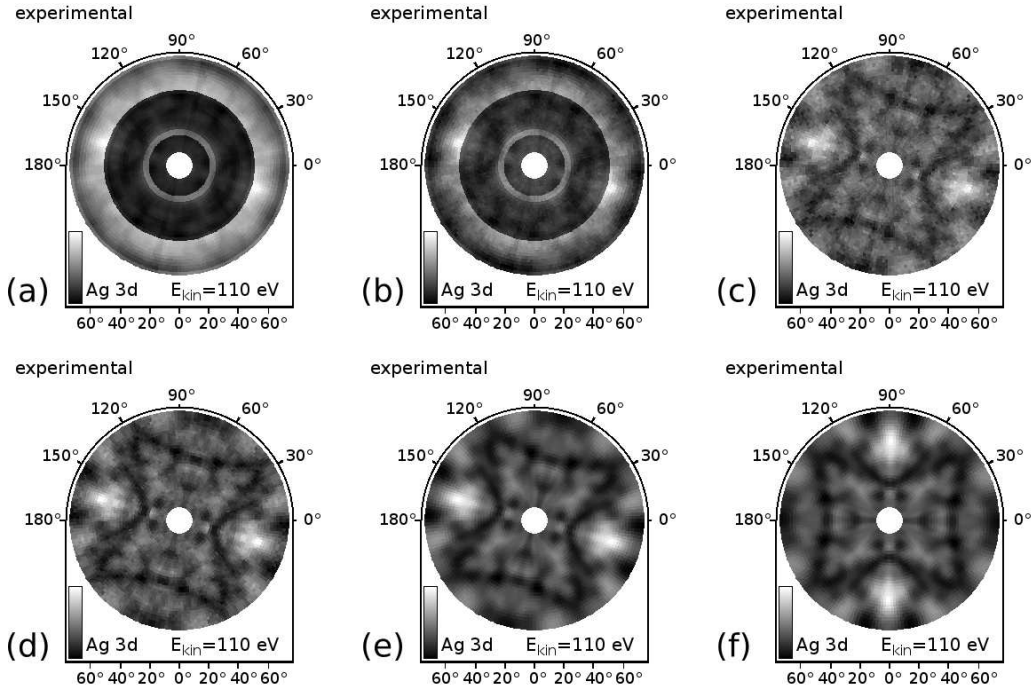

Figure 3.7: Transformation steps for a measured photoelectron diffraction pattern: (a) raw pattern, (b) background subtraction, (c) anisotropy function applied, (d) symmetrizing, (e) gaussian blurring, and (f) aligning.

of more than one component due to different chemical environments. Within this

thesis it will be shown that if the chemical shift of two components is at least about 0.2 eV it is possible to deconvolve all 7200 individual XPS spectra into the chemically shifted components. Consequently, it is possible to obtain different XPD pattern, each corresponding to one chemically shifted component [120, 137]. Since the FWHM and the kinetic energy location of the peak maximum does not change while varying the polar and the azimuthal angle, only the amplitudes of the chemically shifted components are chosen as fitting-parameters. This enables the deconvolution of an XPD pattern by an automated fitting routine applied to thousands of XPS spectra.

3.3.2 Simulation

Due to the loss of the phase information during the measuring process it is not possible to directly conclude on the atomic sites from an XPD pattern. This means, the atomic locations can only be determined indirectly by comparing the measured data to an XPD pattern gained from simulations. For this reason there is a multi-step analysis procedure: First, a possible structure model has to be assumed. Second, the corresponding XPD pattern has to be simulated. Third, the measured XPD pattern has to be compared to the simulated one. If the simulated XPD pattern does not match the experimental one, a rearrangement of the atom positions on the condition that the fundamental characteristics of the structure model are preserved has to be performed.
For the generation of a structure model it is necessary to specify the location of every individual atom inside a unit cell, and to specify the length and directions of the lattice vectors. For simulating the corresponding XPD pattern there are two tools available: Electron Diffraction in Atomic Clusters (EDAC) and Full Multiple Scattering Code for Low Energy Photoelectron Diffraction (MSPHD) for high- and low-energy photoelectron diffraction patterns, respectively [131, 138]. Both simulation tools consider multiple electron scattering. For the simulation of an XPD pattern, the process of photoelectron diffraction is divided into three steps: First, generation of a photoelectron, second, propagation of the photoelectron through the crystal including elastic and inelastic scattering, and third, escaping of the photoelectron from the solid into the vacuum. The resulting differential cross-section gained by the multiple scattered final state wavefunction in

angular momentum representation with $L = (l, m)$ for a distinct emitting atom in a piecewise potential is [131, 138]

$$\frac{\mathrm{d}\sigma}{\mathrm{d}\vec{k}} = F(\vec{k}, \nu) \sum_{m_0=-l_0}^{l_0} \left| \sum_{L,L'} M_L^{L_0} S_{LL'} i^{l'} Y_{L'}(\vec{k}) e^{i\vec{k}\cdot\vec{R}_{j0}} \right|^2 . \tag{3.16}$$

$F(\vec{k}, \nu)$ is a constant for a given photon energy resulting from normalization and from the oscillator strength of the relaxed channel of the final state [139]. $M_L^{L_0}$ represents the electric matrix dipole operator that describes the transition from the one-electron initial state wavefunction with angular momentum L_0 to the final state wavefunction in continuum with angular momentum L. The term $i^l Y_{L'}(\vec{k})$ originates from the series expression of the Green's operator describing the propagation of the photoelectron as a spherical wave outside the muffin-tin radius. $S_{LL'}$ denotes the scattering path operator including all scattering events of the propagating electron wave. The degeneracy of L_0 is obeyed by summing up all degenerated initial states m_0 with $-l_0 \leq m_0 \leq l_0$. Due to possible changes of the angular momentum during scattering and propagation summation over L' is executed.

The essential difference between the EDAC and the MSPHD simulation tool is the calculation of the scattering path operator $S_{LL'}$. Both simulation tools are based on a Green's-function approach describing the propagation of the electron wave between two scattering events. Further, both tools are based on the cluster approach. This means, no long-range order is required. It is an intuitive approach, since excited photoelectrons travel short distances before suffering inelastic losses, thus only the region surrounding the emitting atom contributes to the elastic scattering process [140]. The size of the region contributing to the elastic scattering processes is specified by the scattering sphere r_{scatter}, typically one or two times the IMFP [131, 138]. A description for the specific calculations of the scattering path operator for the two available tools EDAC and MSPHD is given:

EDAC The determination of the scattering path operator $S_{LL'}$ is realized by an iterative process. The determination of the actual scattering processes is based on the assumption of a muffin-tin potential [141]. Further assumptions are, that the scattering process at atom i within the muffin-tin sphere is described by the atomic-cluster matrix element $T_{LL'}^{ii}$, and the propagation of

the scattered photoelectron wave from atom i to atom j is described by the Green's operator $G^{ij}_{LL'}$. The series expansion of the scattering path operator is a subsequent summation of all scattering paths $\Lambda^i_{LL'}$

$$S_{LL'} = \sum_i^N \Lambda^i_{LL'}, \tag{3.17}$$

with

$$\Lambda^i_{LL'} = T^{ii}_{LL'} + \sum_{j\neq i} T^{jj}_{LL'} G^{ij}_{LL'} T^{ii}_{LL'} + \sum_{k\neq j}\sum_{j\neq i} T^{kk}_{LL'} G^{jk}_{LL'} T^{jj}_{LL'} G^{ij}_{LL'} T^{ii}_{LL'} + ... \tag{3.18}$$

describing multiple scattering paths with the first event of scattering taking place at atom i, and the subsequent scattering events taking place at atom j, and k.
The time needed for the iterative evaluation of $S_{LL'}$ is roughly proportional to $N^2(l_{\max}+1)^3$ with N being the number of atoms in the atom cluster, and $l_{\max}$ representing the maximum angular momentum quantum number that is taken into account. The maximum angular momentum $l_{\max}$ can be estimated by $l_{\max} \approx k r_{\text{muffin-tin}}$ with k being the wave number of the photoelectron, and $r_{\text{muffin-tin}}$ representing the radius of the non-constant part of the muffin-tin potential around every atom. Diffraction due to the inner potential V_0 is considered by the diffraction rule stated in equation (3.14).

MSPHD The MSPHD tool is especially designed for low-energy photoelectron diffraction in the range of $30 \leq E_{\text{kin}} \leq 100\,\text{eV}$. In contrast to the EDAC tool, the MSPHD tool provides an exact representation of the scattering path operator to any order $l_{\max}$. The tool determines the scattering path operator $\tau^{0j}_{LL'}$ from the emitting atom 0 to all atoms j within the cluster before escaping from the solid, and subsequently sums up the scattering path operators for all atoms j within the cluster:

$$S_{LL'} = \sum_{j\neq 0}^N \tau^{0j}_{LL'} \tag{3.19}$$

with the analytical expression

$$\tau_{LL'}^{0j} = \left[(T^{-1} - G)^{-1}\right]_{LL'}^{0j} \tag{3.20}$$

taking all scattering events in the solid to any order $l_{\max}$ into account [142]. The damping of the photoelectron wave is considered by adding a complex term to the muffin-tin potential, thus the potential is of Hedin-Lundqvist type [143]. The time for inversion of the matrix $\tau_{LL'}^{0j}$ roughly scales with $N^3(l_{\max}+1)^6$. Thus, applying the MSPHD tool is only advantageous in case of $l_{\max} \leq 8$, and small atom clusters. The refraction rule from equation (3.14) is not taken into account, thus only internal polar angles are calculated [138]. Indeed, it has been shown that in case of silicon based systems the MSPHD tool yields reliable results [98, 120].

In practice, the beam diameter has a size of about $70 \times 30\,\mu\text{m}^2$, thus the number of illuminated atoms is of the order of 10^{12}. The number of photons is of the order of $10^{10}\,\frac{1}{\text{s}}$ [144]. Therefore, simultaneously excited photoelectrons originate from emitting atoms are statistically separated by a multiplicity of the IMFP. Thus, the probability for an inelastic scattering event is much higher than the probability for an interaction of two photoelectrons simultaneously excited at different emitters. Further, the temporal difference between excitation of two photoelectrons at the same emitting atom is that large, that the interaction of these two photoelectrons can be neglected also.
If emitting atoms with a different chemical environment are present, the resulting multiple scattering final state wavefunction for every different atom is calculated, and subsequently incoherently summed up with their relative weight given by their distance to the surface.

For a quantitative comparison the Reliability-factor (R-factor) is utilized [145–147]:

$$R = \frac{\sum_i \left(\chi_{\text{sim},i} - \chi_{\text{exp},i}\right)^2}{\sum_j \left(\chi_{\text{sim},j}^2 + \chi_{\text{exp},j}^2\right)}, \tag{3.21}$$

where χ_{sim} and χ_{exp} denote the anisotropies of the simulated and the experimental XPD pattern, respectively. The R-factor ranges from $R = 0$ to $R = 2$, where $R = 0$ corresponds to perfect correlation, $R = 1$ means there is no correlation, and $R = 2$ corresponds to perfect anti-correlation between the experimental and simulated XPD pattern. An example for different degrees of accordance is given in figure 3.8. If the R-factor is approximately $R \approx 0.1$ the accordance between

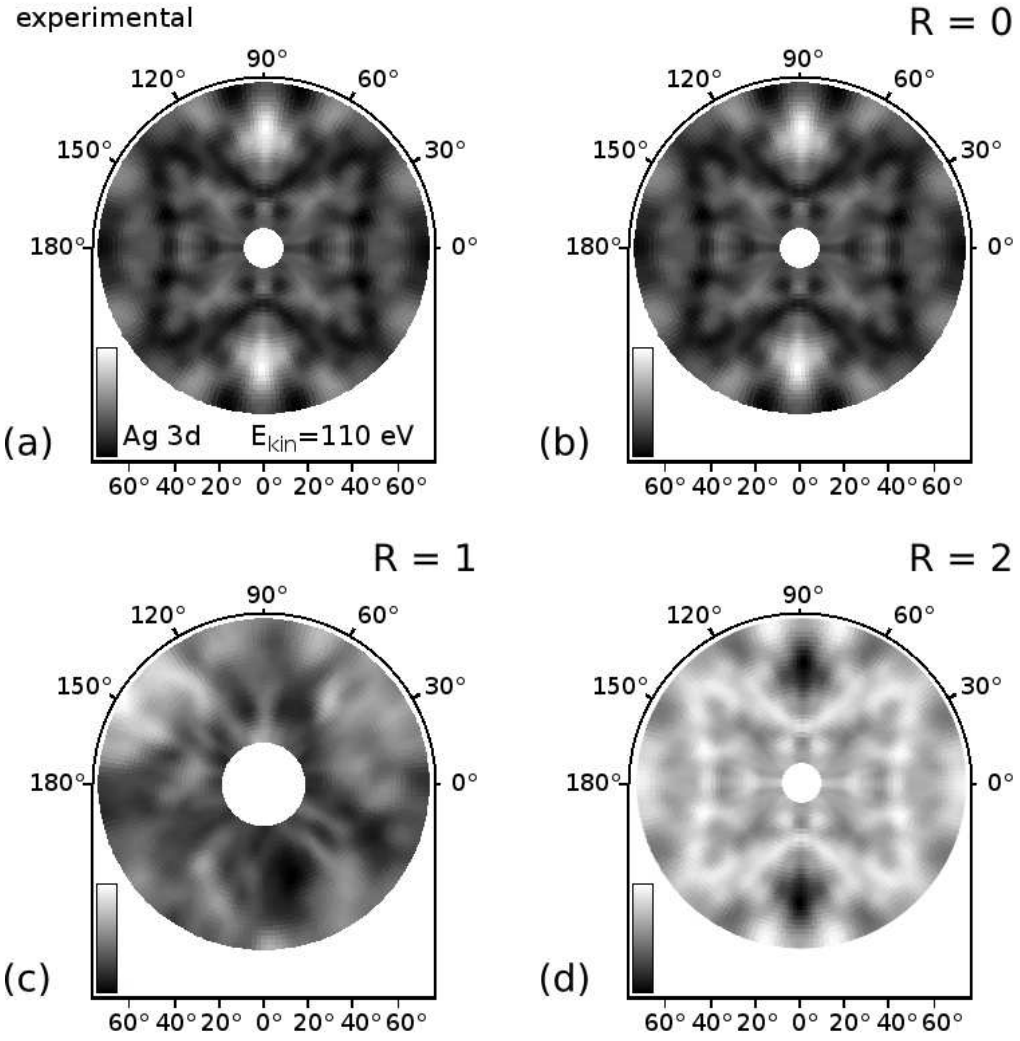

Figure 3.8: Examples given for different degrees of accordance between XPD pattern: measured pattern (a), XPD pattern with R-factors of $R = 0$ (b), $R \approx 1$ (c), and $R = 2$ (d).

experimental and simulated data is sufficient. If the R-factor is much larger than

0.1 the structure model needs to be rearranged, or a completely different structure model has to be presumed.
Possible rearrangements of the structure model include rotation, scaling, and translation in distinct directions for both individual atoms and groups of atoms. These rearrangements from the initial positions $\vec{r}$ to the modified positions $\vec{r}'$ are described by affine transformations [148]:

$$\text{rotation} : \vec{r}' = \underline{\underline{R}}(\alpha_i) \cdot \vec{r}, \tag{3.22}$$

$$\text{scaling} : \vec{r}' = \underline{\underline{S}}(\alpha_i) \cdot \vec{r}, \tag{3.23}$$

$$\text{translation} : \vec{r}' = \underline{\underline{1}} \cdot \vec{r} + \alpha_i \vec{T}. \tag{3.24}$$

The matrices $\underline{\underline{R}}$, $\underline{\underline{S}}$, and $\underline{\underline{1}}$, and the vector $\vec{T}$ describe the transformation process. The range of variation is limited by boundaries and represented by a floating number $0 \leq \alpha_i \leq 1$. This leads to a large number of different possible resulting structures, which makes a systematic scan of all variations impractical. Instead, a genetic algorithm inspired by biological evolution, such as selection, mutation, and combination, is applied. Each resulting structure is now characterized by one gene, consisting of an array of α_i. A set of genes is called generation [149]. The genetic algorithm combines different genes from one generation or mutates individual genes, depending on the general selection rules given in [148], aiming at R-factor minimization. The entire process of the genetic algorithm is given by the flow chart in figure 3.9. It has been shown that utilizing a genetic algorithm is much more promising than other algorithms since it does not converge towards local minima [149]. Still, it is a time-consuming and computationally intense process since a single simulation last between 5 and 20 minutes. The number of generations is typically in the range of 200, resulting in a total computing time for one run of the genetic algorithm of about two days. The results are reliable, although it is a non-deterministic approach. This is proven by the fact that several runs of the genetic algorithm with the same initial structure and the same permitted variations yield resulting structures with deviations as small as 0.1 %. Besides, it has been shown by various experimental works that utilizing the genetic algorithm for structure determination is a reliable tool [98, 149, 150].

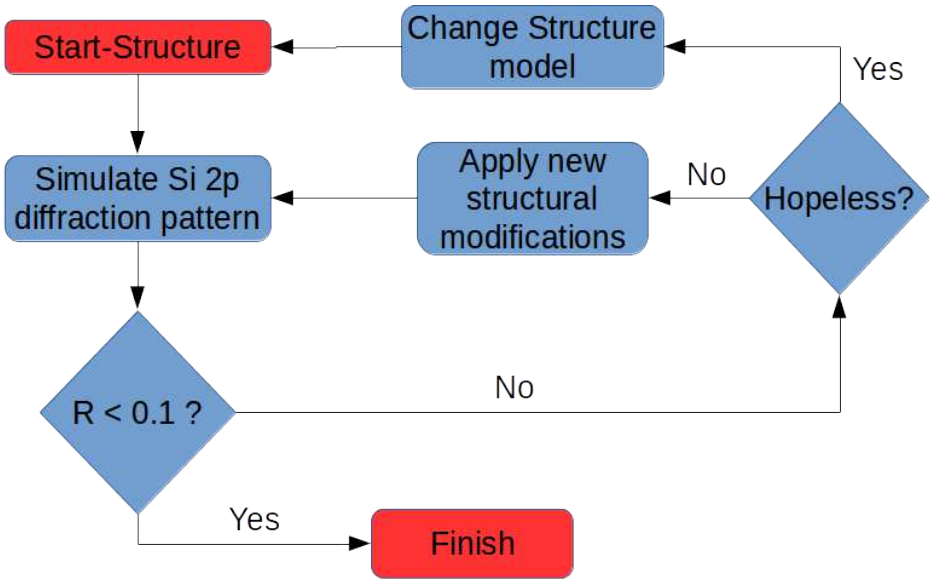

Figure 3.9: Flow chart representing the procedure of generating structure models, simulating the corresponding XPD pattern, comparing simulated and experimental data, and the decision process.

4 Experimental aspects

4.1 UHV-chamber

All of the measurements are performed in an ultra-high vacuum (UHV) chamber. This is of prime importance due to the surface sensitivity of photoelectron spectroscopy and diffraction. A freshly cleaned sample surface is completely covered with one monolayer of residual gas atoms in about 10^{-5} s at ambient pressure. At UHV conditions with a base pressure of about 5×10^{-11} mbar it takes about 10^5 s to cover the entire surface. These values are derived under the assumption of a sticking coefficient $S = 1$ [118, 151]. For the more realistic case, for example molecular oxygen, the sticking coefficient is about $S \approx 0.25$, subsequently the time to cover the entire surface increases by factor 4 [152]. This is enough time for performing even very time-consuming photoelectron diffraction measurements. These vacuum conditions are achieved after baking out the permalloy chamber. It is equipped with a multi-stage vacuum system, consisting of several scroll- and turbo-molecular pumps as well as an ion pump and a titanium sublimation pump. A single-level loadlock is available for sample transfer.
Further, the UHV chamber shown in figure 4.1 is equipped with a 5-axes manipulator, a sputter-gun, a LEED system, an evaporator, and a hemispherical spectrometer with a channeltron detector. These components are introduced in the following.

4.1.1 Manipulator and sampleholder

Measuring an XPD pattern in the hemisphere above the sample is achieved by moving the sample instead of moving the spectrometer. The sample manipulator

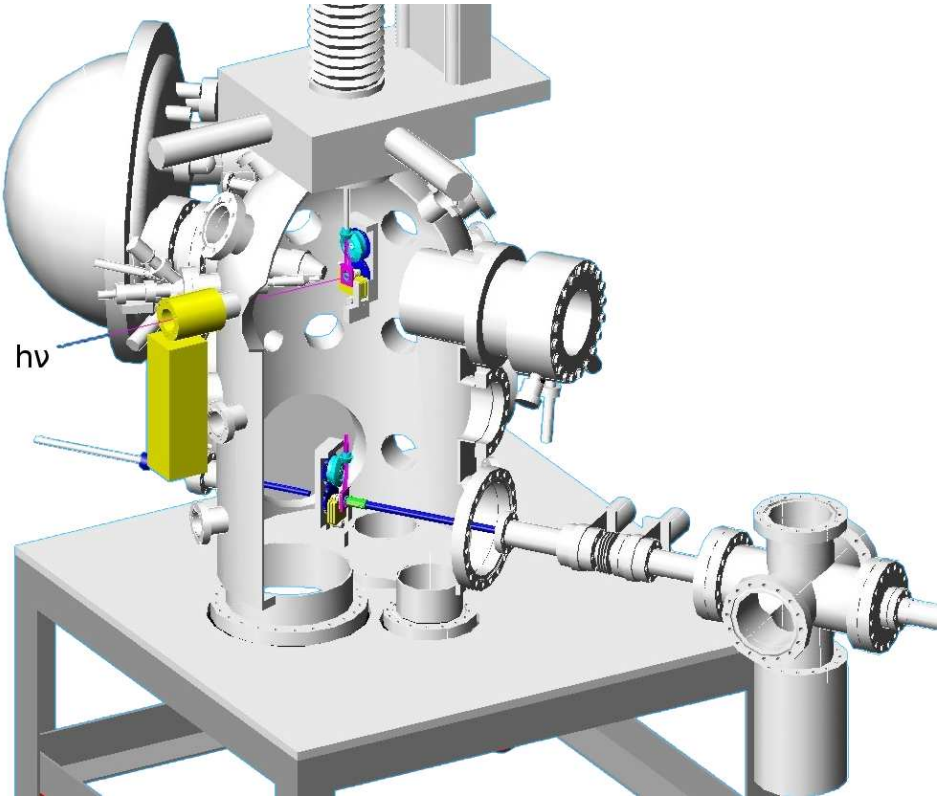

Figure 4.1: Illustration of the UHV chamber. The positions of the manipulator for the sample transfer and XPS/XPD measurements are indicated.

has in total five degrees of freedom. It allows linear motion in three spatial directions and rotation about two axes. In particular, one rotation axis is the surface normal and the corresponding rotation angle is called the azimuthal angle φ. The other rotation is described by the polar angle Θ which inclines the surface normal and the direction to the detector.

The axially symmetric sample holder shown in figure 4.2 is mounted onto the manipulator. Its main part is the base frame build of a Al_2O_3-ceramic with a cylindrical bordering for the sample. After placing the sample inside the bordering it is fixed with a thin tantalum retainer. Beneath the sample bordering a tungsten filament and a contact wire is mounted. The electrical connection to the tungsten filament and the contact wire is established by three copper rings designed as sliding contacts.

Heating of the sample can be done by simply injecting a current into the filament. Due to thermal radiation the sample heats up. Typically, the filament is powered

with 11 W for a sample temperature of 500 K, and 25 W for a sample temperature of 670 K.

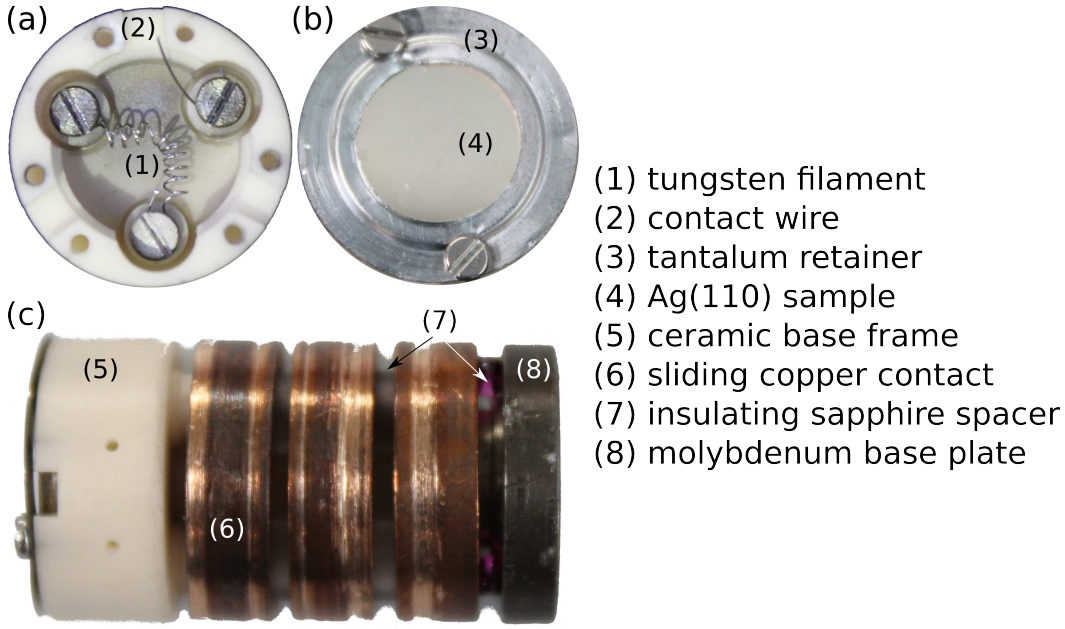

Figure 4.2: Photograph of the mounted sample holder: top view without sample (a), top view with mounted Ag(110) sample (b), and side view (c).

4.1.2 Sputtergun

A common method to remove contaminants from the surface of a sample is sputtering. Within this process, the sample surface is bombarded by noble gas ions. In detail, the sputter-gun is flooded with a noble gas generating noble gas ions by electron impact. The charged ions are accelerated towards the sample by a voltage U in the range of $500\,\mathrm{V} \leq U \leq 1500\,\mathrm{V}$. Typically argon or neon is used as a noble gas. Depending on the energy of the bombarding ions and the inclined angle between the bombarding ions and the surface normal the ions either get implanted into the sample or they remove contaminants from the surface. In both cases, after the bombardment the surface is rough and needs to get smoothed. For this process of rearrangement the sample is annealed as described in chapter 4.1.1. Due to this annealing process the diffusion coefficient increases and and the surface is smoothed. Further, impurities can diffuse from the bulk to the surface.

Therefore, it is necessary to perform repeated sputter- and annealing cycles to clean the sample surface [151, 153].

4.1.3 Evaporator

The deposition of adsorbate layers is conventionally performed by evaporation of the material onto the sample. In order to evaporate silicon a direct current heater is used. The design of such an evaporator is shown in figure 4.3. The evaporator material is contacted by two tantalum sheets and a voltage is applied. If the breakdown voltage is attained, a current begins to flow. Due to the high resistance of the silicon wafer it quickly heats up and starts to evaporate. The precise amount of evaporated material is calibrated by a quartz crystal microbalance (QCM).

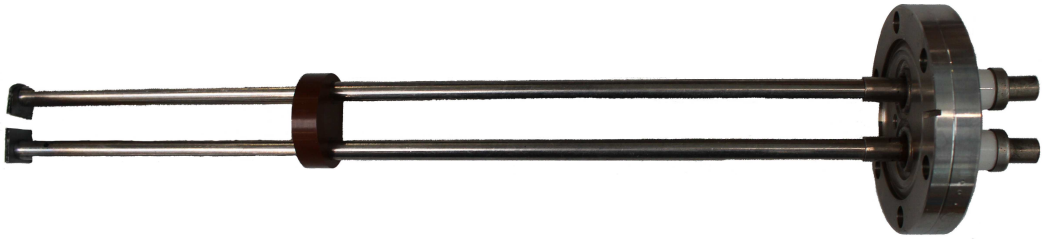

Figure 4.3: Photograph of the direct current evaporator as used for the evaporation of silicon.

4.1.4 Low Energy Electron Diffraction

First observations of scattered electrons were reported by Davisson and Germer, and by Thomson and Reid in 1927 [154]. In 1960 Germer *et al* developed the first modern LEED system [155]. Nowadays, LEED became a commonly used technique for the investigation of the long-range order of surfaces [128]. A schematic diagram of a conventional LEED system is shown in figure 4.4. A typical LEED system consists of an electron gun, a grid system and a luminescent screen. The electron gun is composed of a cathode, a wehnelt cylinder, a double anode, three electrostatic lenses and a drift tube. The electron gun ensures the generation of an electron beam with a kinetic energy in the range from 0 to 1000 eV with a

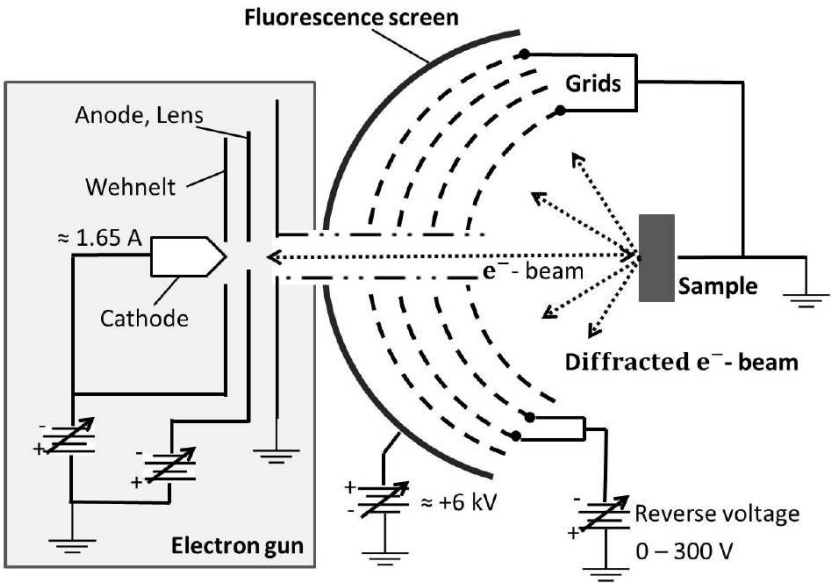

Figure 4.4: Scheme of the used LEED system, adopted from [156].

small energy spread. The electron beam propagates through the grounded drift tube and is focussed onto the sample. The impinging electrons with a wave vector $\vec{k}_0$ get backscattered by two different mechanisms. The electrons get either inelastically backscattered with $\left|\vec{k}_{\text{inelastic}}\right| \neq \left|\vec{k}_0\right|$ making up 99% of the total flux or elastically backscattered with $\left|\vec{k}_{\text{elastic}}\right| = \left|\vec{k}_0\right|$ satisfying the Laue condition in the 2D form [128]:

$$\vec{k}_{0,||} - \vec{k}_{\text{elastic},||} = \vec{G}_{\text{h,k}}, \tag{4.1}$$

where $\vec{k}_{0,||}$ and $\vec{k}_{\text{elastic},||}$ denote the wave vectors parallel to the sample surface, and $\vec{G}_{\text{h,k}} = h\vec{a} + k\vec{b}$ denotes the primitive translation vector of the reciprocal surface lattice [157]. The electrons get backscattered onto a retarding field analyzer consisting of four grids and a phosphor screen as shown in figure 4.4. The grid G1 is grounded enabling undisturbed propagation of the electrons towards the grid system. The grids G2 and G3 are on a negative potential in such a way that only elastically scattered electrons pass these grids. At last, the electrons are accelerated from the grounded grid G4 to the phosphor screen by a voltage of about 5.5 kV causing luminescence.

Referring to equation (4.1) it becomes clear that a LEED pattern reveals the

periodicity of a sample surface. Therefore, a LEED pattern with sharp and bright spots is a proof of a clean and ordered surface. Further, by comparing the LEED pattern of a substrate and a adsorbate-covered substrate the relative size and orientation of the adsorbate unit cell with respect to the substrate unit cell can be concluded [158].

4.1.5 Spectrometer

The UHV chamber is equipped with a spectrometer for energy-dependent electron detection, consisting of a concentric hemispherical analyzer and a channeltron detector as shown in figure 4.5. After being ejected from the sample the photoelectrons are focussed by electrostatical lenses onto the entrance slit. Next, the electrons are decelerated by a retarding voltage $U_{\text{retarding}}$. Only electrons with kinetic energies E_{kin} larger than the applied retarding voltage enter the hemispherical analyzer. Due to the applied voltages to the inner and outer hemisphere only electrons with the energy E_{pass} can pass the hemispheres. Electrons with a kinetic energy $E_{\text{kin}} \neq E_{\text{pass}}$ get sidetracked as shown in figure 4.5. By tuning the retarding voltage $U_{\text{retarding}}$ electrons with different kinetic energies are detected.
A channeltron detector is mounted at the exit of the hemispheres for multiplying the number of electrons. The inner wall of the channeltron is coated with a high-resistance film with a potential difference of about 2.3 kV. The impinging electrons generate secondary electrons. These secondary electrons are accelerated by the potential difference, imping again, and generate an avalanche of electrons. The electron avalanche generates a current proportional to the number of primary electrons that are detected by electronics and interpreted as a counting rate.

As stated in chapter 3.1 the kinetic energy of the photoelectrons after being emitted from the sample can be calculated by equation 3.1. Still, referring to figure 4.6, the measured kinetic energy at the analyzer has to be corrected by the contact potential $\Phi_{\text{S}} - \Phi_{\text{A}}$, where Φ_{A} denotes the work function of the analyzer [105, 159]:

$$E_{\text{kin}} = h\nu - E_{\text{bin}} - \Phi_{\text{S}} + (\Phi_{\text{S}} - \Phi_{\text{A}}) \tag{4.2}$$

$$= h\nu - E_{\text{bin}} - \Phi_{\text{A}}. \tag{4.3}$$

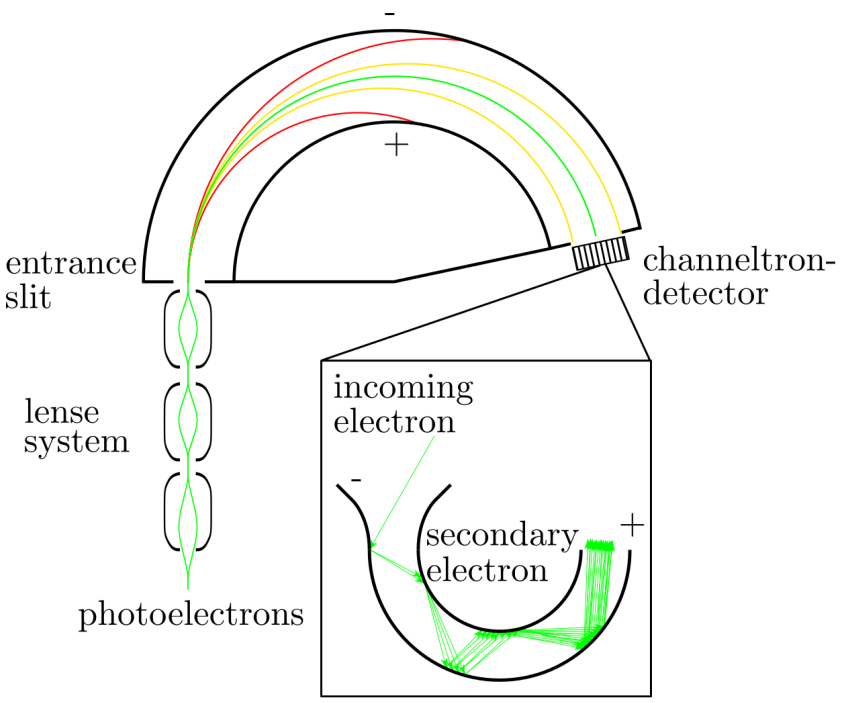

Figure 4.5: Scheme of a concentric hemispherical analyzer utilized for selecting electrons with a distinct kinetic energy. The inset shows the scheme of a single channeltron multiplying the number of incoming electrons.

4.2 Light sources

For the above elucidated techniques based on the photoelectric effect the samples need to be illuminated with photons in the soft x-ray regime. For this purpose two light sources are available: the synchrotron light source Dortmunder Elektronenspeicherring Anlage (DELTA) located at the TU Dortmund, Germany and a conventional x-ray tube.

4.2.1 Beamline 11

DELTA is an electron storage ring with several dipoles and insertion devices providing synchrotron radiation [161]. One of this insertion devices is the undulator U55 supplying synchrotron radiation in the soft x-ray regime between $h\nu = 55\,\mathrm{eV}$ and $1500\,\mathrm{eV}$ to beamline 11. This undulator is composed of alternating arranged

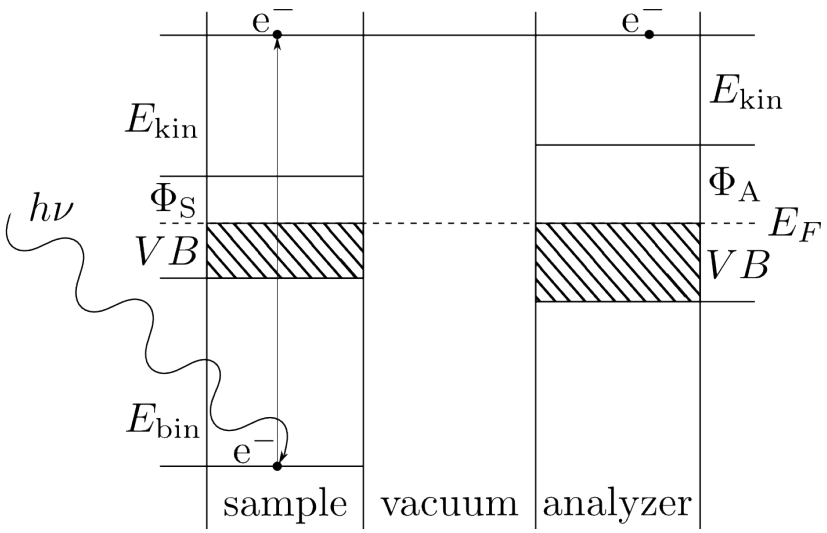

Figure 4.6: Energy scheme of photoemission and subsequent transport from the sample to the analyzer. The measured kinetic energy of the photoelectron at the analyzer is not equivalent to the kinetic energy of the photoelectron directly after photoemission.

permanent magnets with a periodic length of 55 mm supplying linearly polarized light. The electrons passing the undulator are forced by the alternating magnetic field onto a sinusoidal path, hence, they emit electromagnetic radiation. Due to their velocity of almost speed of light $v \approx c$ the emitted synchrotron radiation transforms to a strongly forward shaped cone [162]. After being separated from the electron beam the synchrotron radiation propagates through beamline 11 which consists of several mirrors, slits, and gratings. The mirrors focus the beam onto the sample, the slits mainly function as an aperture, and the gratings as dispersive elements are responsible for selecting a distinct energy from the emitted undulator radiation. By tuning the undulator gap and the grating position the energy of the impinging photons onto the sample can be varied. The beamspot at the sample is in the size of about $70 \times 30\,\mu\mathrm{m}^2$. For a photon energy of $h\nu = 400\,\mathrm{eV}$ the energy resolution is about $\frac{E}{\Delta E} = 20000$ and the photon flux is about $3 \times 10^{10}\,\frac{\mathrm{photons}}{\mathrm{s}\times 100\,\mathrm{mA}}$ in high-resolution mode [144, 163].

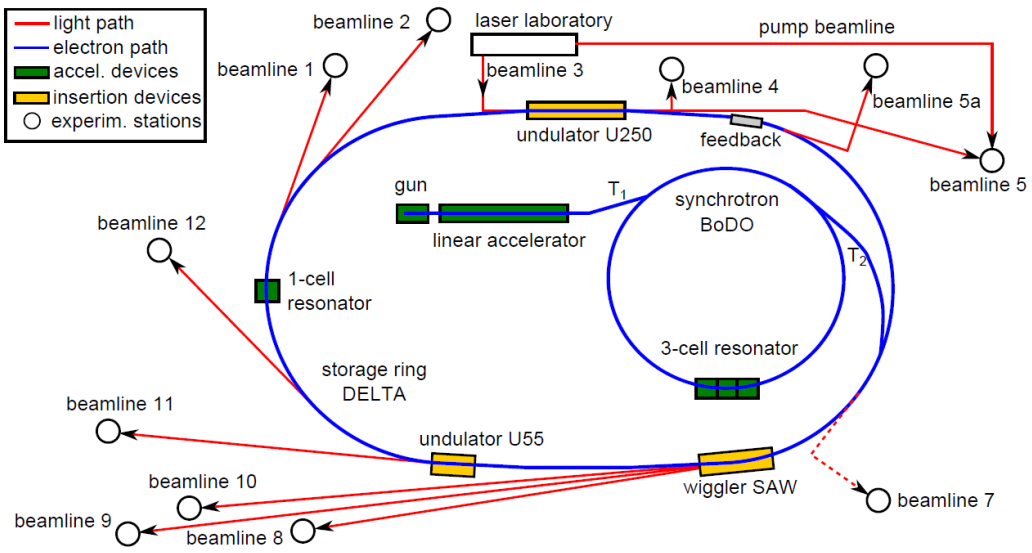

Figure 4.7: Schematic illustration of DELTA. The electrons are generated at the electron gun, accelerated by the LINAC up to 80 MeV, and transferred via T1 to the BoDo synchrotron. Inside BoDo the electrons are accelerated up to 1492 MeV. Subsequently, the electrons are transferred via T2 to the Delta storage ring [160].

4.2.2 X-ray tube

A conventional X-ray tube is additionally mounted to the UHV-chamber. Electrons emitted from a tungsten filament by thermionic emission are accelerated by a high voltage towards a water cooled anode. Depending on the voltage and the anode material a typical spectrum of x-rays is emitted. Such a typical spectrum consists of a continuous contribution determined by bremsstrahlung, and characteristic emission lines. The intensity of the main characteristic emission lines is typically two orders of magnitude larger than the bremsstrahlung. In this experimental setup an x-ray tube with a magnesium and an aluminium anode is available, providing characteristic $K_{\alpha 1,2}$ x-ray radiation of $h\nu_{Mg} = 1253\,eV$, and $h\nu_{Al} = 1486\,eV$. Further characteristic emission lines are either negligible in intensity or well separated in energy. In comparison to synchrotron radiation the energy width of the emission lines of aluminium and magnesium is much larger with values of $\Delta E_{Mg} = 0.68\,eV$ and $\Delta E_{Al} = 0.85\,eV$. The photon flux density is in the range of about $10^{10}\,\frac{photons}{s \cdot cm^2}$ [164].

5 Preparation

In order to investigate the local order within the silicon nano-ribbons and the interaction between them and the silver substrate beneath, the sample system needs to be prepared carefully. This means, first the pristine Ag(110) sample has to be cleaned and well reconstructed since only this preconditioning facilitates the subsequent growth of silicon nano-ribbons by evaporation of silicon onto the Ag(110) surface. Both the preparation of the pristine Ag(110) sample and the growth of the nano-ribbons is conducted in situ. Concerning the Ag(110) surface LEED and XPS measurements are given verifying the (1×1)-reconstruction. In total three independent proofs ensuring the successful growth of silicon nano-ribbons are given, in particular these proofs are based on LEED, XPS, and valence band spectroscopy measurements.
Initially, the successful preparation of a clean and highly ordered Ag(110) surface is reported. Following, a detailed description of the preparation of silicon nano-ribbons is given.

5.1 Preparation of Ag(110)

Preparation of a clean and well ordered sample surface is processed as described in chapter 4.1.2 by several cycles of sputtering and annealing. The surface was sputtered with argon ions with a kinetic energy of about $E_{\text{sputter}} = 1000\,\text{eV}$, followed by annealing to $T_{\text{anneal}} = 670\,\text{K}$ for about $t_{\text{anneal}} = 30\,\text{min}$. The inclined angle between the bombarding argon ions and the surface normal was set to 45°. After five repeated cycles of sputtering and annealing the XPS spectrum reveals a surface with residual contamination from oxygen, and carbon as shown in figure 5.1. After five further cycles of sputtering and annealing the contaminants were removed from

the sample surface, also shown in 5.1. The XPS spectra were recorded with an incoming photon energy of $h\nu = 650\,\mathrm{eV}$ at normal emission. The core-level signals originating from the C1s core-level at a kinetic energy of $E_{\mathrm{kin,\ C1s}} \approx 360\,\mathrm{eV}$, and from the O1s core-level at a kinetic energy of $E_{\mathrm{kin,\ O1s}} \approx 110\,\mathrm{eV}$ have vanished. All further signals correspond to the Ag(110) substrate as indicated in the spectrum. The XPS signal at a kinetic energy of $E_{\mathrm{kin,\ Ag3d}} \approx 310\,\mathrm{eV}$ originating from the Ag 3d core-level is the one with highest intensity owing to its differential cross section. For this reason only the Ag 3d core-level signal will be focussed when analyzing the high-resolution XPS spectra of the substrate.

Despite concluding on a clean surface from the XPS signal, optical inspection

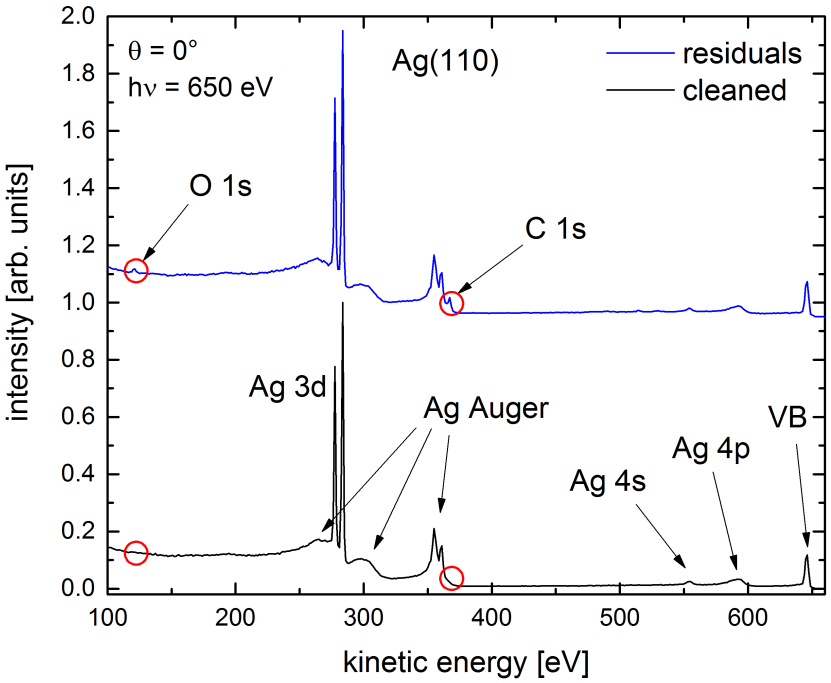

Figure 5.1: Survey spectrum of the Ag(110) sample after five consecutive cycles of sputtering and annealing were performed pictured in blue. Still, residual contaminants from oxygen and carbon are detected. After five further cycles no contamination can be detected.

reveals a milky haze of the Ag(110) substrate. This milky haze empirically arise for three main reasons: first, annealing the substrate at high temperatures close

to the melting point can cause such haze. This is caused by massive amounts of evaporated silver from the surface. Second, due to high ion flux and momentum transfer during sputtering and too little annealing faceting and surface roughness can occur. Third, accidentally sputter-deposited contaminants from the vicinity of the crystal onto the surface below the detection limit of x-ray photoemission spectroscopy can cause a haze. The first and second mentioned explanation have in common that the roughness typically develops simultaneously and homogeneously. In contrast, the roughness due to the third reason starts to appear at the position where the contaminants are deposited first and then progressing across the sample from there with further sputtering.

The first mentioned reason for roughness is precluded, since the temperature value for annealing of $T_{\text{anneal}} = 670\,\text{K}$ is in the same range as reported by several published studies. Thus, the implications of the second mentioned issue of a too high sputter dose is analyzed. The ion species was changed from argon to neon, the energy of the bombarding ions was reduced from $E_{\text{sputter}} = 1000\,\text{eV}$ to $E_{\text{sputter}} = 600\,\text{eV}$, and the inclined angle between the bombarding ions and the surface normal was increased from 45° to 70°. Precautionary, the beam of bombarding ions was solely focussed onto the Ag(110) crystal, and subsequently, avoiding transferring contaminants from the tantalum retainer to the surface. As a result the sample surface has no milky haze after ten further cycles of sputtering and annealing. The resulting LEED pattern is shown in figure 5.2. The LEED pattern is acquired at an incoming electron energy of $E_{\text{el}} = 50\,\text{eV}$. The two-dimensional reciprocal lattice observed in the LEED pattern is of a primitive rectangular type. The lattice vectors $\vec{b}_1$ and $\vec{b}_2$ are indicated in the figure. After measuring the length of the reciprocal lattice vectors the ratio $\frac{|\vec{b}_1|}{|\vec{b}_2|}$ can be estimated as 1.42. This value fits to the expected ratio value of $\sqrt{2}$ and proves the (1×1)-reconstructed Ag(110) surface. After the successful preparation of the Ag(110) sample the surface is feasible for the growth of silicon nano-ribbons.

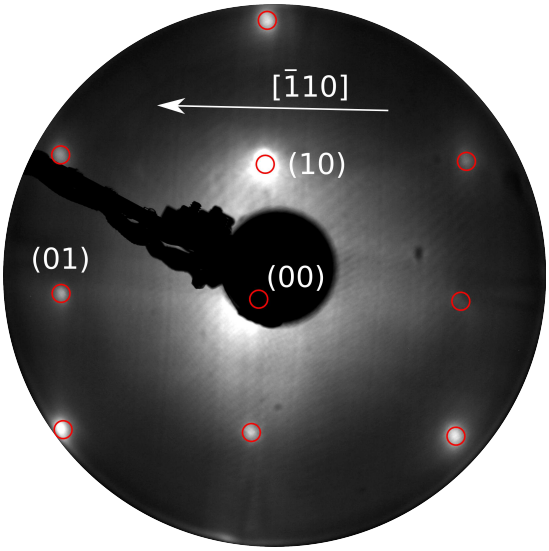

Figure 5.2: LEED pattern of the sputter-cleaned and (1×1)-reconstructed Ag(110) surface. The energy of the electron beam is 50 eV [82].

5.2 Preparation of (5×2)-reconstructed silicon nano-ribbons

For the successful growth of silicon nano-ribbons on a Ag(110) substrate the temperature of the substrate during growth has to be approximately 500 K. Therefore, the tungsten filament is powered with 4 V × 2.7 A = 10.8 W. The temperature of the Ag(110) substrate is monitored by a pyrometer. Silver is one of the materials with highest thermal conductivity, thus the sample is in thermal equilibrium after only a few minutes. The heated Ag(110) sample is placed in a distance of about 25 cm from the direct current silicon evaporator described in chapter 4.1.3. For evaporating a sufficient amount of silicon the silicon wafer needs to be heated to more than 1300 K. This temperature is reached when the current is set to about 16 A at a voltage of 4.5 V corresponding to a deposited power of about 70 W. In figure 5.3 the time-dependent deposited amount of silicon for different power values is shown. Obviously, a minimum power of about 70 W is necessary to actually generate a significant amount of evaporated silicon. Due to the high temperature of the silicon wafer during the evaporation process the surrounding UHV chamber heats up, subsequently the desorption rates of the walls

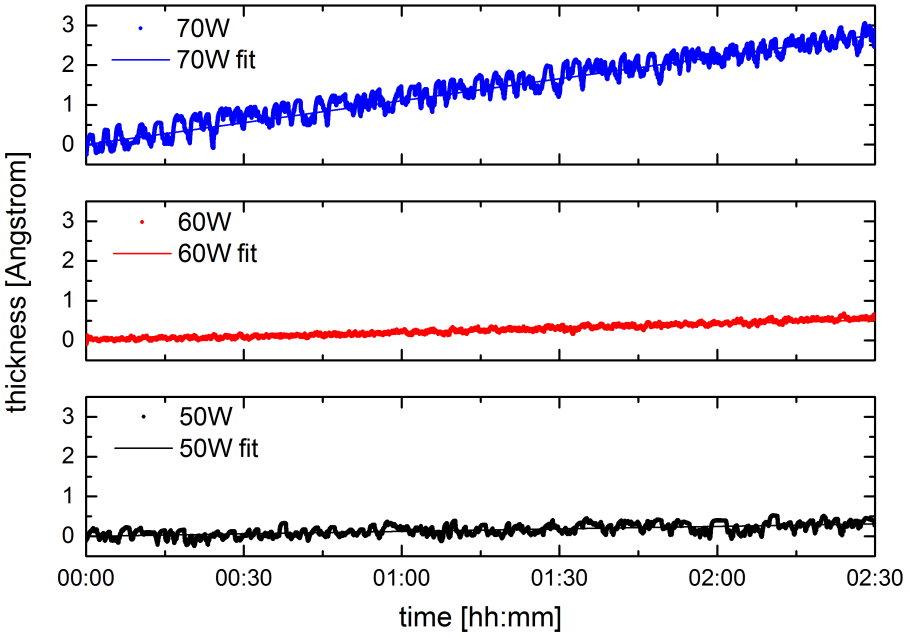

Figure 5.3: Monitored thickness of a silicon film measured by the QCM recorded at different power values heating the silicon wafer.

of the UHV chamber increase. The desorbed material is able to contaminate the (1×1)-reconstructed Ag(110) surface, thus heating of the UHV chamber needs to be prevented. To counteract this heating and desorption, a copper cooling unit is installed keeping the temperature of the UHV chamber at ambient temperature. After evaporation of silicon for 120 min a LEED pattern shown in figure 5.4 is acquired. The energy of the electron beam is 25 eV. The lattice vectors of the rectangular structure, and thus spots originating from the Ag(110) substrate can be identified and are indicated by red circles. Further, between the spots (00) and (10) four additional spots can be seen, and between the spots (00) and (01) one additional spot can be seen. Thus, the surface reconstruction can be identified as the characteristic (5×2)-reconstruction due to the growth of silicon nano-ribbons on the (1×1)-reconstructed Ag(110) substrate. The deposited amount of silicon is about $120\,\text{min} \times 0.018 \frac{\text{Å}}{\text{min}} \approx 2.2\,\text{Å}$ as determined by the evaporation time and the growth rate which was estimated by the QCM. Assuming a silicon growth along the honeycomb Si(111) plane the deposited amount of silicon corresponds

to a coverage of about 0.45 monolayer (ML). This convention was introduced in literature and is widely used [30,44]. As shown by STM measurements a coverage of 0.43 ML corresponds to a Ag(110) surface that is entirely covered with silicon nano-ribbons [44].

A high resolution XPS spectrum of the Si 2p signal after silicon deposition

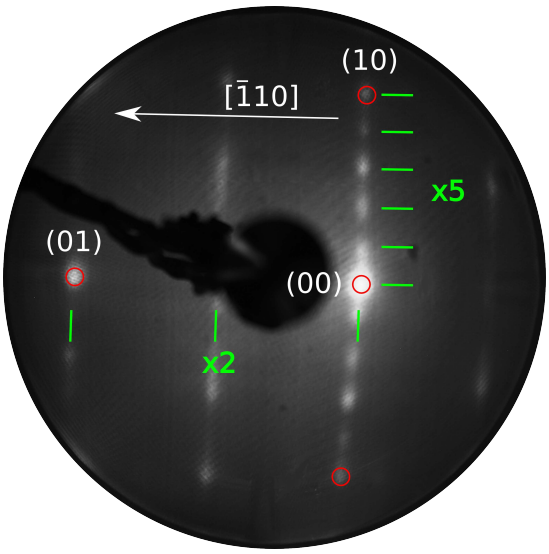

Figure 5.4: LEED pattern after silicon evaporation onto the (1×1)-reconstructed Ag(110) surface. The energy of the electron beam is 25 eV. The LEED pattern clearly shows a (5×2)-reconstruction as indicated by the green lines [82].

is shown in figure 5.5. The incoming photon energy was $h\nu = 180\,\text{eV}$ and the spectrum was recorded at normal emission. Due to spin-orbit coupling the signal splits into to components shifted by $\Delta E_{\text{SO, Si 2p}} = 0.605\,\text{eV}$ with a height ratio of $h_{\text{LS, p-orbital}} = \frac{1}{2}$. A further splitting due to different chemical environments can be recognized. The observed shape is characteristic for the growth of silicon nano-ribbons on Ag(110) [14].

Further, an angle integrated spectrum of the valence band of the sample was recorded after silicon deposition and is shown in figure 5.6. The individual spectra were recorded at an incoming photon energy of $h\nu = 80\,\text{eV}$ in azimuthal and polar angle ranges of $0° \leq \varphi \leq 358.2°$ and $22° \leq \Theta \leq 60°$ with step widths of $\Delta\varphi = 1.8°$ and $\Delta\Theta = 2°$, respectively. There are four expected states S_1, S_2, S_3, and S_4 as indicated in figure 5.6 with a shift in binding energy of $\Delta E_{S1} = 0.92\,\text{eV}$,

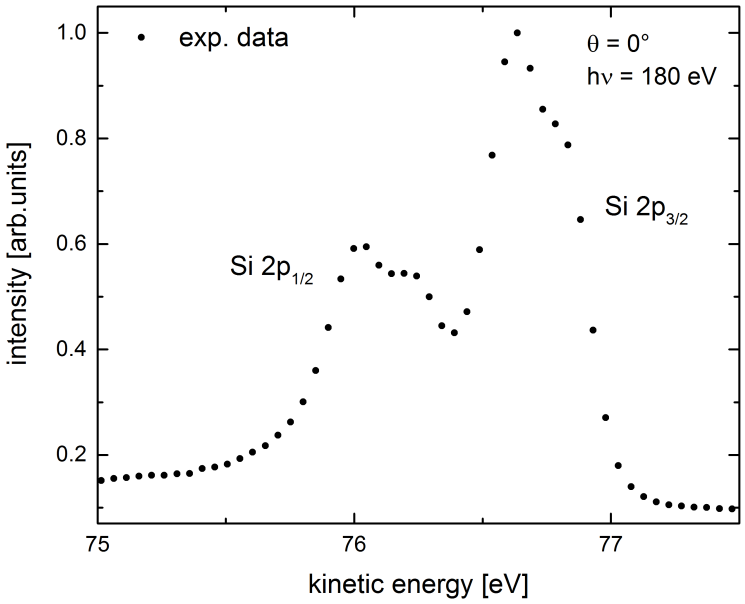

Figure 5.5: High resolution XPS spectrum of the Si 2p signal after growth of silicon nano-ribbons. The energy of the incoming photons is $h\nu = 180\,\mathrm{eV}$ and the spectrum is recorded at a polar angle of $\Theta = 0°$.

$\Delta E_{\mathrm{S2}} = 1.45\,\mathrm{eV}$, $\Delta E_{\mathrm{S3}} = 2.37\,\mathrm{eV}$, and $\Delta E_{\mathrm{S4}} = 3.12\,\mathrm{eV}$, respectively. The states S_1, S_2, merge into a broad maximum, whereas S_3 can be clearly identified in the recorded angle integrated spectrum. The state S_4 can not clearly be resolved. This is due to the overlapping of S_4 with the increasing Ag(110) state for relative binding energy larger than 3 eV.

In conclusion, three independent proofs for the successful preparation of silicon nano-ribbons on a (1×1)-reconstructed Ag(110) surface are presented. Despite, until now no information concerning the interaction of the nano-ribbons and the Ag(110) substrate are obtained. Nor information on the local order within the silicon nano-ribbons are obtained. This questions will be addressed in the following chapters 6.1 and 6.2.

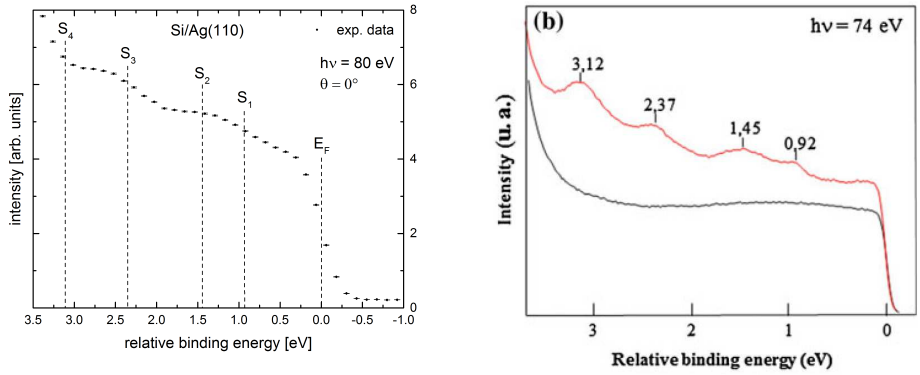

Figure 5.6: High resolution spectrum of the valence band of silicon nano-ribbons on Ag(110). Energy of the incoming photons is 80 eV (left). The spectrum is an angle-integrated spectrum with 200 azimuthal angles ranging from $0° \leq \varphi \leq 358.2°$, and 20 polar angles ranging from $22° \leq \Theta \leq 60°$. The reported states S_1, S_2, S_3, and S_4 due to the growth of silicon nano-ribbons are indicated by the dashed lines. Angle-integrated valence band spectra of pristine Ag(110) surface and silicon nano-ribbons on Ag(110) (right) as reported in literature [14, 24].

6 Results

On the basis of the successful preparation of the nano-ribbons a detailed XPS and XPD analysis is presented evaluating the chemical interaction between the Ag(110) substrate and silicon nano-ribbon, and subsequently the local order within the nano-ribbons. The XPS analysis directly reveals information concerning the presence of different chemical environments. The analysis of the XPD pattern is less straight forward since simulations are necessary for extracting the entire information from an XPD pattern.
The range of suggested structure models describing the local order within the silicon nano-ribbons is broad as already shown in chapter 2.2. Since almost no publication provides the precise atom locations, the characteristics of every structure models were extracted. In a next step, structure models are build reproducing the characteristics of each model. Subsequently, the genetic algorithm is applied while preserving the characteristics of the structure model to find the best match between the simulated XPD pattern of each structure model and the experimental XPD pattern.
After evaluating the structure model that describes the experimentally gained data best, a deconvolution process is performed revealing the origin of the two chemically shifted components in the XPS spectra of the Si 2p signal.

6.1 (1×1)-reconstructed Ag(110)

6.1.1 XPS analysis

A high-resolution spectrum of the Ag 3d signal is shown in figure 6.1. It is recorded at an incoming photon energy of $h\nu = 450\,\mathrm{eV}$. This photon energy is chosen since

the cross section is increased from 1 Mbarn to 2 Mbarn in comparison to the survey spectrum recorded at an incoming energy of $h\nu = 650\,\mathrm{eV}$. Further, the surface sensitivity is enhanced due to the minimum of the inelastic mean free path for electrons with kinetic energies in the range from $E_{\mathrm{kin}} = 30\,\mathrm{eV}$ to $E_{\mathrm{kin}} = 100\,\mathrm{eV}$. The spin-orbit coupling causes the Ag 3d signal to split into two components shifted by $\Delta E_{\mathrm{SOC,\ Ag\ 3d}} = 6.05\,\mathrm{eV}$ with a height ratio of $h_{\mathrm{SOC,\ d\text{-}orbital}} = \frac{2}{3}$. The signals at $E_{\mathrm{kin,\ P1}} \approx 73.0\,\mathrm{eV}$, $E_{\mathrm{kin,\ P2}} \approx 69.3\,\mathrm{eV}$, and $E_{\mathrm{kin,\ P3}} \approx 67.0\,\mathrm{eV}$ account to three plasmon excitations. The signals at E_{P1} and E_{P2} correspond to the first and second plasmon excitation of the Ag $3d_{5/2}$ component. They are shifted by 4.0 eV, and 7.8 eV regarding the Ag $3d_{5/2}$ signal. The signal at E_{P3} corresponds to the first plasmon excitation of the Ag $3d_{3/2}$ component and is shifted by 3.9 eV regarding the Ag $3d_{3/2}$ signal [165–167]. The asymmetry parameter is $\alpha = 0$. It is not possible to resolve whether these plasmon excitations arise from electron oscillations in the bulk material or at the surface since it is known from Electron Energy Loss Spectroscopy (EELS) measurements that the energy difference between bulk and surface plasmons is about 0.1 eV [168].

A second high-resolution Ag 3d core-level spectrum recorded at an polar angle of $\Theta = 60°$ is shown in figure 6.1. The higher polar angle provides an even smaller information depth than for normal emission. This makes the spectrum more sensitive to surface effects. Again, the splitting of the Ag 3d core-level signal and the three plasmon excitations are observed. The shape of the Ag 3d signal remains unchanged. This is an additional proof that no contaminants are present at the surface. Likewise, the shape of the plasmon excitations remains the same with their relative intensity rising in comparison to the Ag 3d core-level signal. From the rise of the plasmon signal with increasing polar angle it is concluded on the surface plasmon nature of the plasmon signal [169, 170]. This is the final proof of a sample surface cleaned from contaminants, since surface plasmons are only observable in case of perfectly cleaned sample surfaces [171].

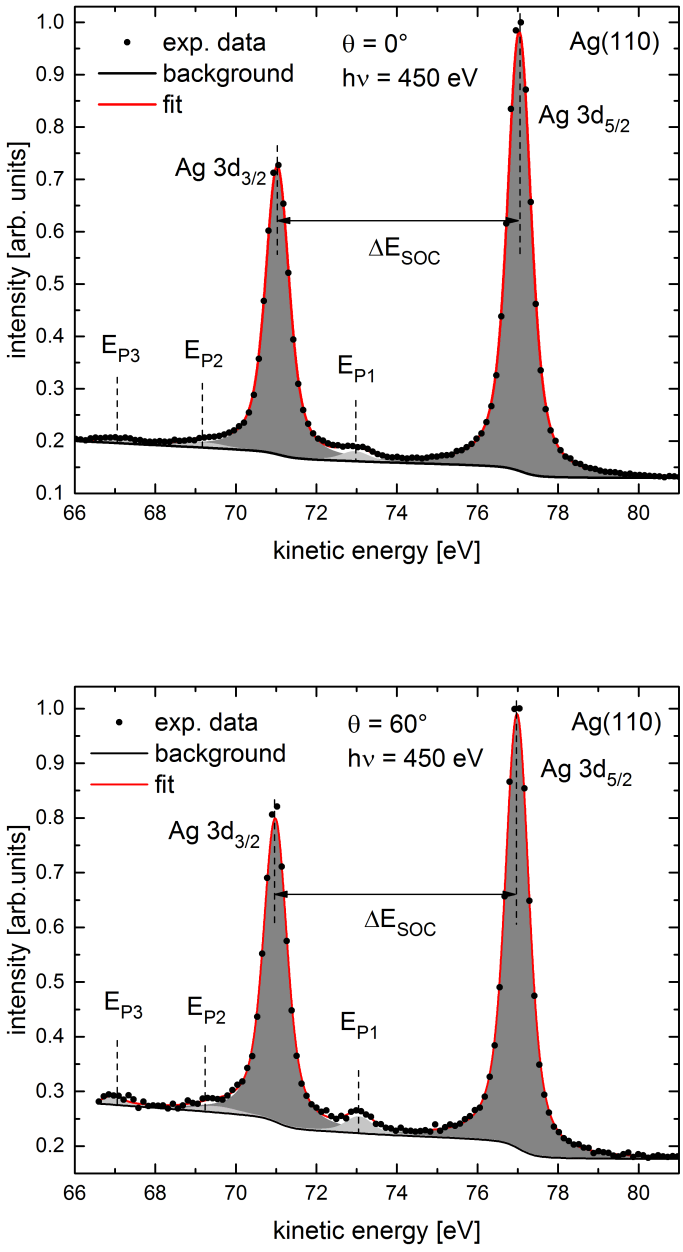

Figure 6.1: High-resolution XPS spectra of the Ag 3d signal after careful preparation as shown in chapter 5.1 for normal emission (top) and a high polar angle of $\Theta = 60°$ (bottom). The energy of the incoming photons was $h\nu = 450\,\mathrm{eV}$ [82].

6.1.2 XPD analysis

Two XPD patterns of the cleaned and (1×1)-reconstructed Ag(110) sample were recorded. One pattern was recorded at an incoming photon energy of $h\nu_{\mathrm{Al}} = 1486\,\mathrm{eV}$ and a second pattern was recorded at an incoming photon energy of $h\nu = 480\,\mathrm{eV}$. Figure 6.2 shows the XPD pattern of the Ag 3d signal measured at an incoming photon energy of $h\nu = 1486\,\mathrm{eV}$ corresponding to a kinetic energy of $E_{\mathrm{kin}} = 1131\,\mathrm{eV}$, with a corresponding IMFP path of about 20 Å. Due to the high IMFP this pattern is solely sensitive to bulk atoms within the IMFP, thus the pattern is dominated by forward scattering, resulting in strong maxima along distinct crystal orientations and the blurred Kikuchi lines. The pattern exhibits a two-folded symmetry and two mirror axes according to the symmetry properties of the Ag(110) lattice structure. The features due to scattering at the three nearest neighbours in the directions [010], [011], and [112] are indicated by the green, red, and yellow circles and are shown additionally in figure 6.2 with their corresponding polar angles $\Theta(\measuredangle([110],[010]) = 45°$, $\Theta(\measuredangle([110],[011]) = 60°$, and $\Theta(\measuredangle([110],[112]) = 54{,}7°$. Calculating a pattern by geometric projection along the crystallographic axes reveals the pattern shown in 6.2 (bottom row, left). The main features can be identified and also the Kickuchi lines are visible, though the intensities are not well reproduced. A more sophisticated pattern is simulated by the EDAC simulation package as shown in figure 6.2 (bottom row, right). The simulation is based on the lattice structure reported in chapter 2.1 and shown in figure 2.3. The cluster size includes about 5000 atoms and the scattering sphere is $r_{\mathrm{scattering}} = 20\,\mathrm{Å}$. The angular momentum cutoff was set to $l_{\mathrm{max}} = 6$, the inner potential is $V_{\mathrm{inner}} = 22\,\mathrm{eV}$ [172]. As iteration method the recursive method is chosen with an iteration order of 20. The measured XPD pattern, see figure 6.2 top row (left), and the XPD pattern simulated with the EDAC package, see figure 6.2 bottom row (right), are in excellent agreement as indicated by an R-factor of $R = 0.08$. All features and the Kickuchi lines are well reproduced, in location as well as in intensity.

Figure 6.3 shows an XPD pattern of the Ag 3d signal measured in the surface sensitive regime at an incoming photon energy of $h\nu = 480\,\mathrm{eV}$ corresponding to a kinetic energy of $E_{\mathrm{kin}} = 110\,\mathrm{eV}$. From the analysis of the LEED pattern it was already concluded on a (1×1)-reconstructed surface. Still, possible relaxa-

tion effects were not considered yet. The XPD pattern of a bulk-like terminated Ag(110) surface without consideration of any relaxation effects is shown in figure 6.3. The accordance between the measured and simulated pattern is not very high, as specified by an R-factor of $R = 0.55$. Thus, relaxation of the topmost layers needs to be considered. In detail, the topmost layers are allowed to individually relax in [110] direction by values d_i ranging from $-0.5\,\text{Å} \leq d_i \leq 0.5\,\text{Å}$. In order to determine the correct values the genetic algorithm was applied. The simulation parameters and iteration method are the same as for the simulation of the high energy XPD pattern, solely the scattering sphere can be reduced to a value of $r_{\text{scattering}} = 9\text{Å}$ due to the small IMFP. The XPD pattern of the resulting structure after applying the genetic algorithm is shown in figure 6.3 (bottom row, left) with the corresponding structure model also in figure 6.3 (bottom row, right). An R-factor of $R = 0.11$ indicates a very good accordance between the experimental and simulated XPD pattern. The values describing the relaxation of the three topmost layers estimated by the genetic algorithm are $d_1 = 1.73\,\text{Å}$ between the topmost and second topmost layer, $d_2 = 1.36\,\text{Å}$ between the second and third topmost layer, and $d_3 = 1.35\,\text{Å}$ between the third and fourth topmost layer. Relaxation of the layers beneath are considered as well, but it turned out that they these are in bulk configuration. The observed relaxation effects are in agreement with previous works, who reported an relaxation of the topmost layers by analyzing LEED patterns [78, 79].

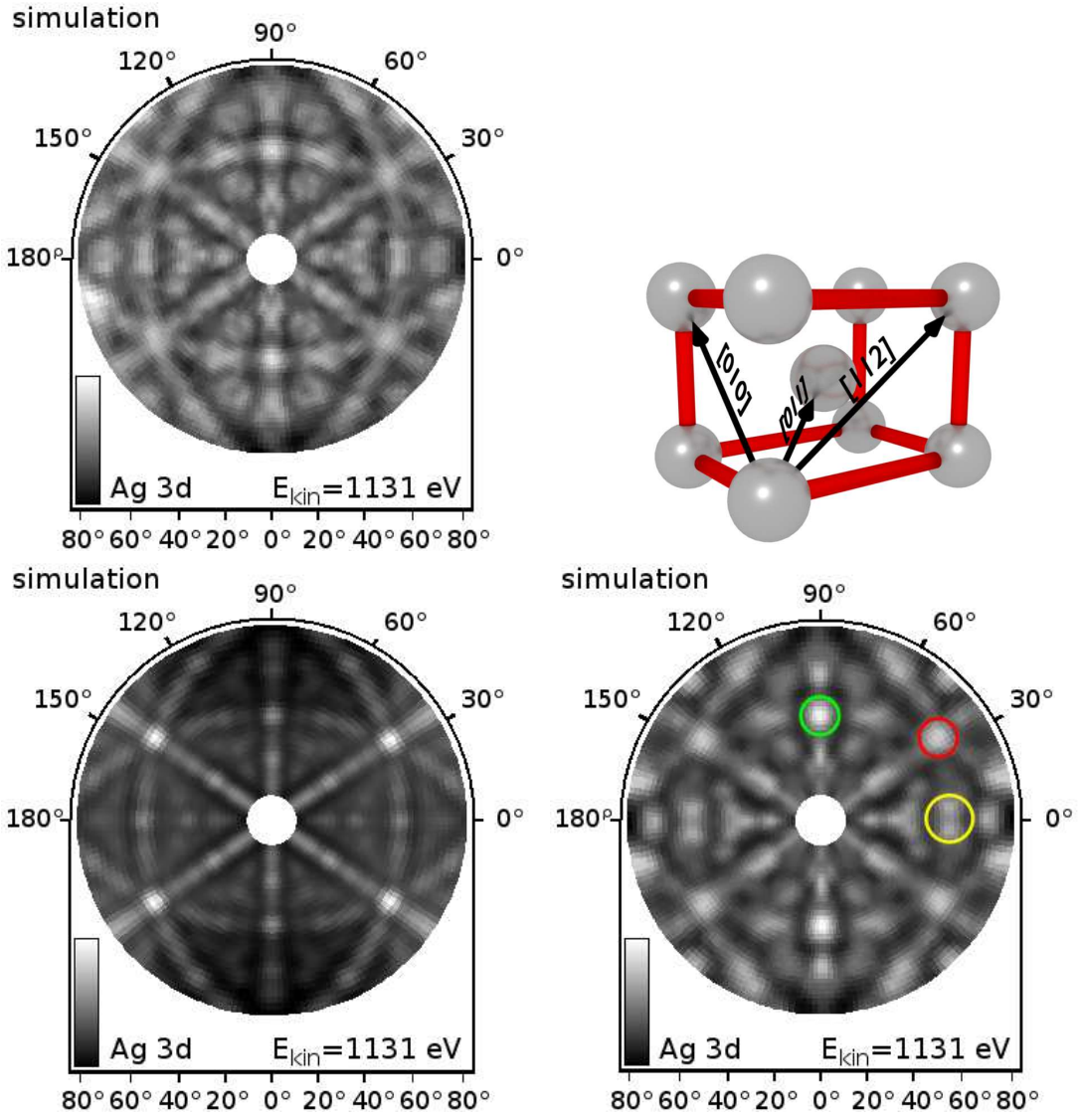

Figure 6.2: top row: Experimental XPD pattern of the Ag 3d signal of the (1×1)-reconstructed Ag(110) surface recorded at a kinetic energy of $E_{\mathrm{kin}} = 1131\,\mathrm{eV}$ (left). The energy of the incoming photon was $h\nu = 1486\,\mathrm{eV}$. Structure model of the truncated Ag(110) crystal (right) with three directions [010], [011], and [112] indicated. bottom row: Calculated XPD pattern by geometric projection along the crystallographic axes (left). Simulated XPD pattern of the Ag 3d signal at a kinetic energy of 1131 eV by utilizing the EDAC package (right). The R-factor between this simulated pattern and the experimental XPD pattern is $R = 0.08$.

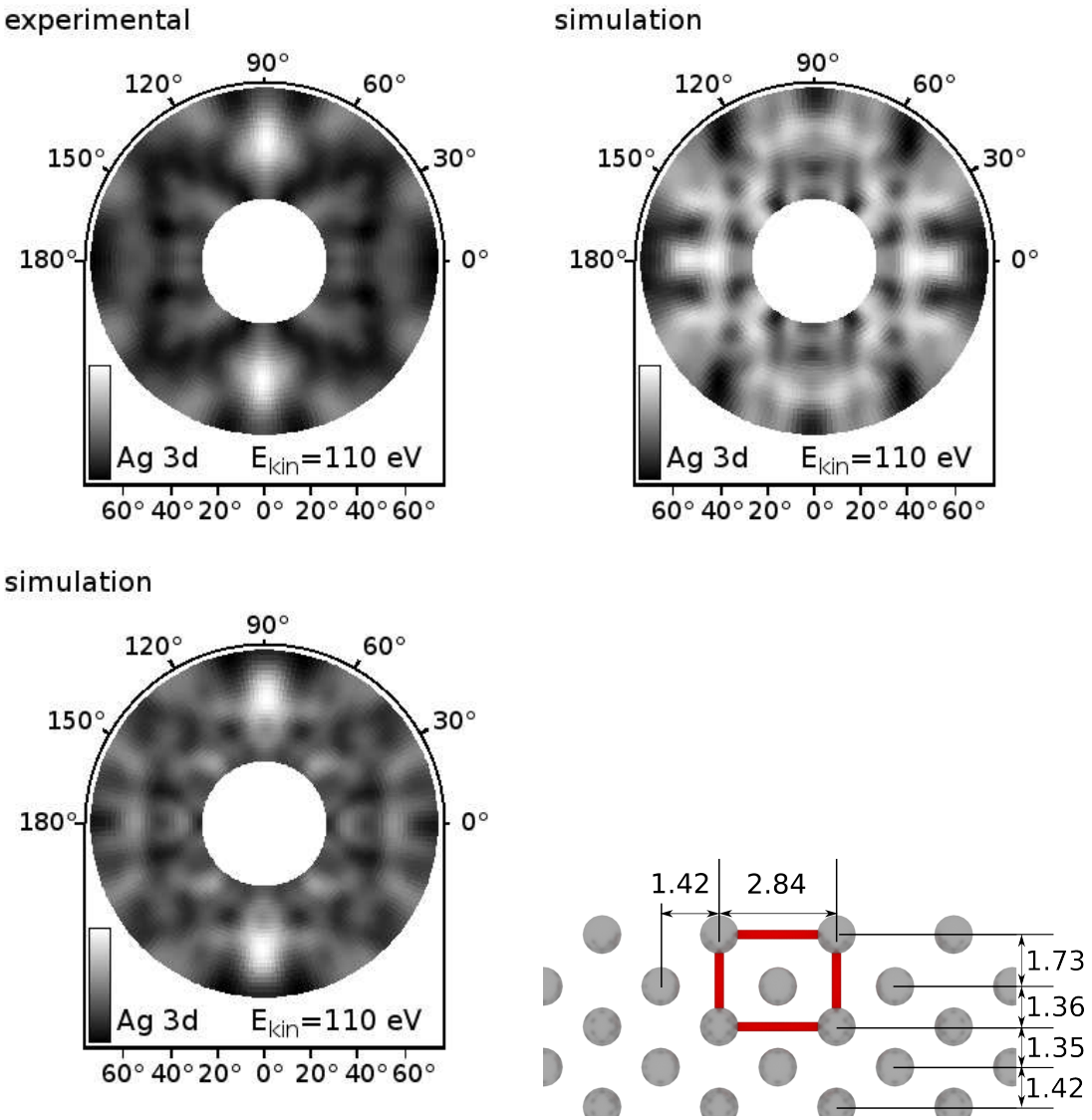

Figure 6.3: top row: Experimental XPD pattern of the Ag 3d core-level signal of the (1×1)-reconstructed Ag(110) surface taken at a kinetic energy of $E_{\mathrm{kin}} = 110\,\mathrm{eV}$ (left). The energy of the incoming photon was $h\nu = 480\,\mathrm{eV}$. Simulated XPD pattern of the Ag 3d signal for the truncated and not relaxed Ag(110) surface at kinetic energy of 110 eV by utilizing the EDAC package (right). bottom row: Simulated XPD pattern of the Ag 3d signal at a kinetic energy of 110 eV by utilizing the EDAC package (left). The R-factor between this simulated pattern and the experimental XPD pattern is $R = 0.11$. (right) Side view of the resulting structure model. In comparison to the truncated Ag(110) structure the two topmost layers of silver atoms are relaxed.

6.2 (5×2)-reconstructed silicon nano-ribbons

6.2.1 XPS analysis

The results from the XPS analysis of the clean Ag(110) substrate were already discussed in chapter 6.1.1. High resolution XPS spectra of the Ag 3d core-level signal after the growth of silicon nano-ribbons are shown in figure 6.4. The energy of the incoming photons was $h\nu = 450\,\mathrm{eV}$. The high resolution spectra were recorded at normal emission $\Theta = 0°$ and at a polar angle of $\Theta = 60°$ for a more surface sensitive measurement. The signals E_{P1}, E_{P2}, and E_{P3} corresponding to the plasmon excitations vanished. From the absence of the plasmon excitations it is concluded that these excitations are caused by surface plasmons since bulk plasmons are not expected to vanish if the substrate is covered with an adsorbate. A fitting procedure reveals that the shape and position of the Ag 3d core-level signal remain unchanged. Even a surface sensitive measurement at a polar angle of $\Theta = 60°$ yielded no evidence for additional components in the XPS spectrum that are caused by the ordered growth of silicon nano-ribbons. As in the case of the clean Ag(110) surface the asymmetry parameter of the Ag 3d signal is $\alpha = 0$. Since silver is a well conducting metal its XPS signal is assumed to reveal an intrinsic asymmetry, which is not observed in the recorded XPS spectra. This is due to the impact of instrumental broadening that conceals the asymmetry. The instrumental broadening due to the energy spread of the incoming photon energy and the pass-energy of the hemispherical analyzer is larger than in the later reported XPS spectra of silicon. Thus, the concealment of the asymmetry of the Ag 3d signal is likely. A summary of the resulting fitting parameters for the Ag 3d signal before and after deposition is given in table 6.1. Comparable systems like two-dimensional germanene on a Au(111) substrate or silicon nano-ribbons on a Au(110) undoubtedly give rise to a substrate-adsorbate interaction. This was evidenced by high resolution XPS spectra of the Au 4f core-level signal before and after the growth of germanene [173] and silicon nano-ribbons [174] which clearly indicated the rise of a new chemically shifted component. It is concluded from the here reported XPS data, that there is no strong chemical bond between the Ag(110) substrate and the silicon nano-ribbon.

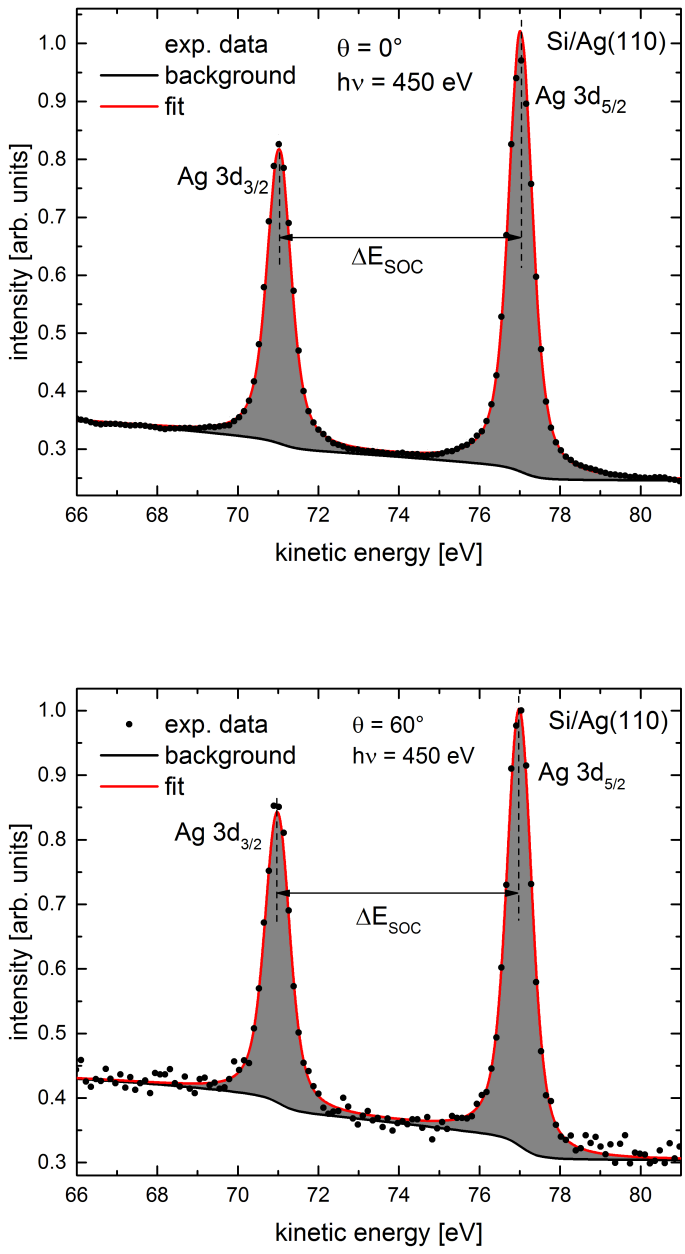

Figure 6.4: High-resolution XPS spectra of the Ag 3d signal after the ordered adsorption of silicon for normal emission (top) and a more surface sensitive polar angle of $\Theta = 60°$ (bottom). The energy of the incoming photons was $h\nu = 450\,\mathrm{eV}$ [82].

system	component	polar angle	E_{kin} (eV)	FWHM (eV)	SOC (eV)	height
	Ag $3d_{5/2}$	0	77.03	0.71	6.05	0.86
	plasmon 1	0	72.91	0.79		0.02
	plasmon 2	0	69.22	1.01		0.01
before	plasmon 3	0	67.00	0.78		0.01
deposition	Ag $3d_{5/2}$	60	77.01	0.71	6.05	0.81
	plasmon 1	60	73.00	0.79		0.03
	plasmon 2	60	69.40	1.01		0.01
	plasmon 3	60	66.91	0.78		0.02
after	Ag $3d_{5/2}$	0	77.01	0.71	6.05	0.74
deposition	Ag $3d_{5/2}$	60	77.02	0.71	6.05	0.68

Table 6.1: Summary of the resulting fitting parameters for the Ag 3d signal before and after deposition of silicon.

A XPS spectrum of the Si 2p core-level signal after the deposition of silicon and the formation of silicon nano-ribbons is already shown in figure 5.5. In figure 6.5 the results of a least-square-fitting procedure are shown. The incoming photon energy was $h\nu = 180\,\mathrm{eV}$ and the spectrum was recorded at normal emission. An XPS spectrum recorded at an emission angle of $\Theta = 60°$ is also given. For the Si 2p core-level signal an asymmetric line shape based on the Doniach-Sunjic profile as described in chapter 3.2.2 is presumed. The measured spectrum is characterized by two distinct chemically shifted components with a relative energy shift of $\Delta E_{\mathrm{chem}} = 0.22\,\mathrm{eV}$. The component displayed in dark grey is termed component C1, and the component displayed in light grey is termed component C2 in the following. The full width at half maximum (FWHM) of both components is FWHM $= 0.24\,\mathrm{eV}$. The ratio of spin-orbit coupling is $h_{\mathrm{Si\,2p}} = \frac{1}{2}$ since the electrons originate from a p-type subshell with an angular momentum $l = 1$, and the energy shift due to spin-orbit coupling is $E_{\mathrm{SOC}} = 0.61\,\mathrm{eV}$ in agreement with literature [68]. The asymmetry parameter is determined to be $\alpha = 0.11$. A summary of the resulting fitting parameters for the Si 2p core-level signal is given in table 6.2. The asymmetric line-shape indicates that the excited photoelectrons interact with a metallic part of the sample before being expelled from the crystal. There are two possible explanations. The first explanation is that the silicon nano-ribbons

are metallic, thus an electron-hole pair in the conductance band is excited. This conclusion is drawn in literature [14]. A second possible explanation is that the asymmetric line shape is caused by the excitation of electron-hole pairs in the conduction band of the silver substrate beneath the nano-ribbons. In order to finally determine whether the asymmetry arises from the metallic Ag(110) substrate or from intrinsically metallic silicon nano-ribbons, they need to be transferred to an isolating substrate.

The existence of two chemically shifted components proves that there are silicon atoms with two distinct chemical environments present. In literature there are Si 2p signals reported which consist of four distinct signals if the Ag(110) surface is not entirely covered with nano-ribbons [68]. Two out of the four signals reported in literature are assigned to the two chemically shifted components as shown in figure 6.5. One of the two further reported signals is dedicated to the extremities of the elongated nano-ribbons. The remaining component is dedicated to the fundamental 0-dimensional building block known as nano-dot, see chapter 2, that did not merged into nano-ribbons. The XPS signal dedicated to the extremities is only observable if the nano-ribbons are only a few nanometers in length. From the absence of this signal it is deduced that the nano-ribbons on the here reported Ag(110) surface are extremely elongated with lengths of several hundreds of nanometers. An XPS signal of the fundamental building blocks is only observable if these are not merged into nano-ribbons. Thus, from the absence of the signal related to fundamental building blocks it is deduced that all nano-dots on the surface merged into nano-ribbons.

The XPS spectrum recorded at a high polar angle of $\Theta = 60°$ reveals a slightly different height ratio between component C1 and C2. Since it is known from the measurements by the QCM that the amount of deposited silicon corresponds to a height of approximately 2 Å the change in height of the distinct XPS components can be related to diffraction effects. Thus, it is not possible to assign the components C1 and C2 to individual emitting silicon atoms from the analysis of the XPS spectra. The analysis of two XPD patterns of the Si 2p core-level signal for precise structure determination is conducted in the following chapter.

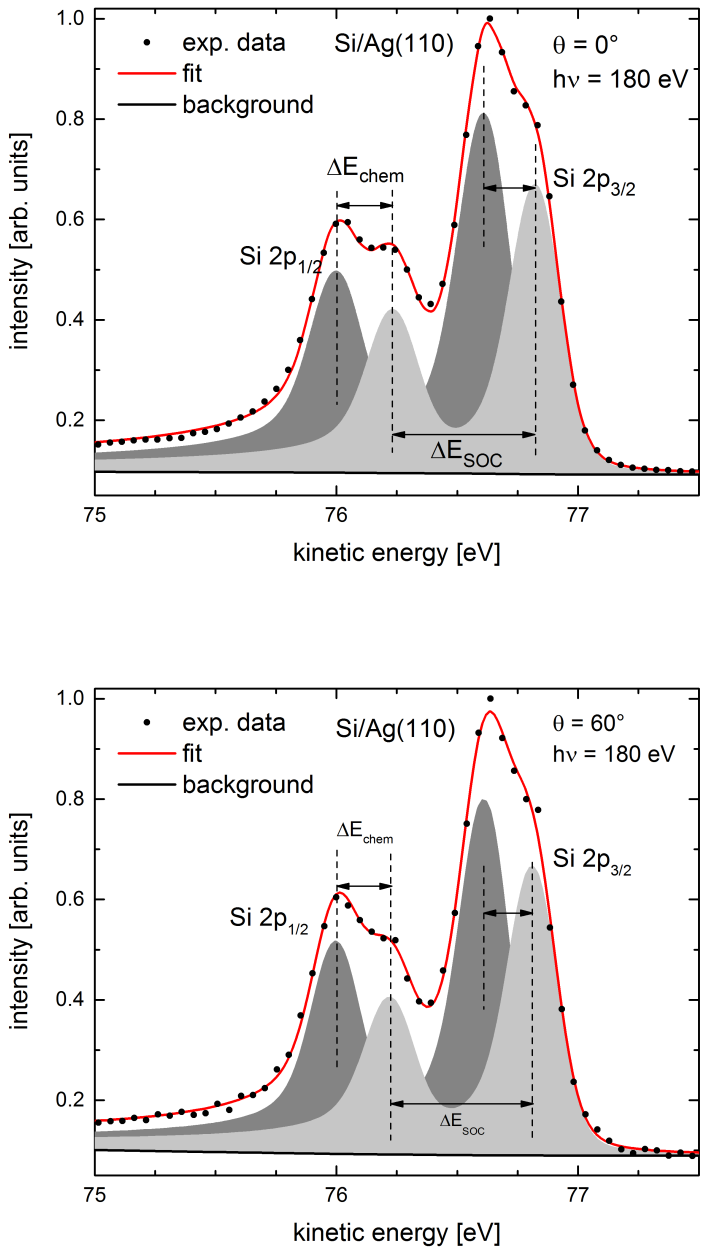

Figure 6.5: High-resolution XPS spectra of the Si 2p core-level signal after the ordered adsorption of silicon for normal emission (top) and a high polar angle of $\Theta = 60°$ (bottom). The energy of the incoming photons was $h\nu = 180\,\mathrm{eV}$ [82].

system	component	polar angle	E_{kin} (eV)	FWHM (eV)	α	SOC (eV)	height
after deposition	Si $2p_{3/2}$, C1	0	76.59	0.24	0.11	0.61	0.73
	Si $2p_{3/2}$, C2	0	76.83	0.24	0.11	0.61	0.60
	Si $2p_{3/2}$, C1	60	76.59	0.24	0.11	0.61	0.70
	Si $2p_{3/2}$, C2	60	76.78	0.24	0.11	0.61	0.56

Table 6.2: Summary of the resulting fitting parameters for the Si 2p signal after deposition of silicon.

6.2.2 XPD analysis

The atomic structure of the (1×1)-reconstructed Ag(110) surface was already determined by the analysis of an XPD pattern in chapter 6.1. For determining the structure model that describes the local order within the silicon nano-ribbons two XPD patterns of the Si 2p signal were recorded. One XPD pattern was recorded at a kinetic energy of 76.5 eV corresponding to an incoming photon energy of $h\nu = 180\,\text{eV}$. This XPD pattern is recorded for polar angles in the range $10° \leq \Theta \leq 80°$. A polar angle of $\Theta = 80°$ is the highest allowed polar angle in the experimental set-up. Since polar angles lower than 10° yield no reliable diffraction information these polar angles were not recorded. The step width of the polar angle was $\Delta\Theta = 2°$. The range of recorded azimuth angles is $0° \leq \varphi \leq 358.2°$ with an incremental step width of $\Delta\varphi = 1.8°$. The second XPD pattern was recorded at a kinetic energy of 36.5 eV corresponding to an incoming photon energy of $h\nu = 140\,\text{eV}$. The pattern is recorded in the polar angle range $10° \leq \Theta \leq 70°$. Polar angles below $\Theta = 10°$ were neglected for the same reason as for the first measured XPD pattern. The range and the step width of the azimuth angle φ is the same as for the first XPD pattern. In contrast to the first XPD pattern, the second is acquired with an increased energy resolution. This allows a deconvolution of the pattern into the individual components C1 and C2 that were reported in figure 6.5. Both measured XPD pattern are shown in figure 6.6.

The measured XPD pattern are analyzed as follows: For every proposed structure

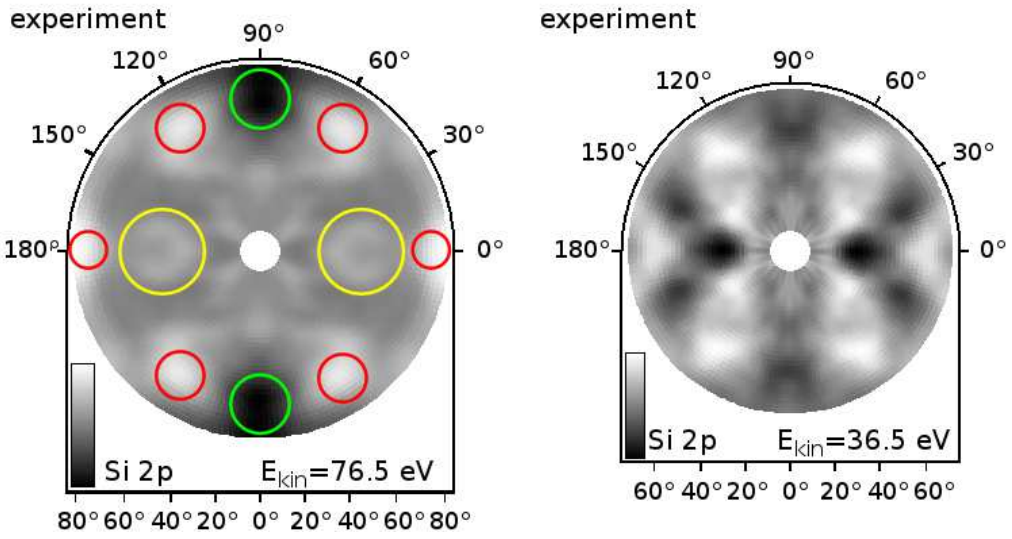

Figure 6.6: Experimental XPD pattern of silicon nano-ribbons adsorbed on Ag(110) recorded at kinetic energies of $E_{\mathrm{kin}} = 76.5\,\mathrm{eV}$ and $E_{\mathrm{kin}} = 36.5\,\mathrm{eV}$ at incoming photon energies of $h\nu = 180\,\mathrm{eV}$ (left) and $h\nu = 140\,\mathrm{eV}$ (right), respectively [82].

model the corresponding XPD pattern at a kinetic energy of 76.5 eV is simulated by the MSPHD tool and compared to the measured XPD pattern at a kinetic energy of 76.5 eV. Possible rearrangements of individual atoms or groups of atoms while preserving the characteristics of the structure model are evaluated using the genetic algorithm as explained in chapter 3.3.2. The formation of one, two, three, or four missing rows as proposed by Bernard *et al* is considered while applying the genetic algorithm [29]. In the following discussion only the result with the lowest R-factor is presented. Further, the relaxation of the topmost Ag(110) layers is taken into account. When a structure model is determined that fits to the experimental XPD pattern it is checked whether the structure model also is in accordance with the second measured XPD pattern recorded at a kinetic energy of 36.5 eV. In a last step, the high-resolution XPD pattern recorded at a kinetic energy of 36.5 eV is deconvolved into two XPD pattern, one corresponding to the component C1, and the other one corresponding to the component C2 as shown in figure 6.5. Starting with the structure that fits to both integral XPD pattern, the genetic algorithm was re-applied. The individual atoms were allowed to rearrange in the three spatial directions and the absolute maximum value of each allowed

rearrangement was 0.1 Å. The combination of the genetic algorithm and simultaneously performed permutation of emitting atoms within the unit cell reveals the origin of the two chemically shifted components C1 and C2.
The XPD pattern measured at a kinetic energy of 76.5 eV is shown in figure 6.6(left). It reveals a two-folded symmetry and two mirror axes, and it is characterized by six features corresponding to a high anisotropy value indicated in red, two features corresponding to a low anisotropy value indicated in green, and two features in "C"-shape indicated in yellow. It is not possible to deduce on the local symmetry properties of each emitting atom from the symmetry properties of the XPD pattern. The reason for this issue is the incoherent superposition of multiple scattering wave functions originating from different emitting atoms. Due to the low kinetic energies of $E_{\mathrm{kin}} = 76.5\,\mathrm{eV}$ and $E_{\mathrm{kin}} = 36.5\,\mathrm{eV}$ all of the following XPD pattern are calculated with the MSPHD tool.

Model proposed by Leandri

The XPD pattern corresponding to the structure model proposed by Leandri [24] is shown in figure 6.7 (left). There are 30 emitting silicon atoms within a unit cell each with a different structural environment and in total the cluster includes more than 1000 silicon and silver atoms. The scattering sphere was set to $r_{\mathrm{scattering}} = 7\,\mathrm{Å}$ and the maximum angular momentum was set to $l_{\mathrm{max}} = 6$. These two simulation parameters remain the same for all Si 2p XPD patterns simulated at a kinetic energy of 76.5 eV. In contrast to the EDAC tool the inner potential is calculated by a subroutine integrated within the MSPHD tool.
The experimental XPD pattern shows a two-folded symmetry and two mirror axes, whereas the simulated XPD pattern of the structure model proposed by Leandri solely reveals one mirror axes. The accordance between the simulated XPD pattern and the experimental XPD pattern is very poor as proved by an R-factor of $R_{\mathrm{Leandri}} = 0.70$. In order to improve the match between the experimental and simulated XPD pattern the genetic algorithm was applied. The allowed structural modifications include a shift of the Ag(110) substrate in [110], [001], and [$\bar{1}$10] direction relatively to the honeycomb silicon adsorbate, the variation of the value that describes the buckling in [110] direction, and the scaling of the nano-ribbon's

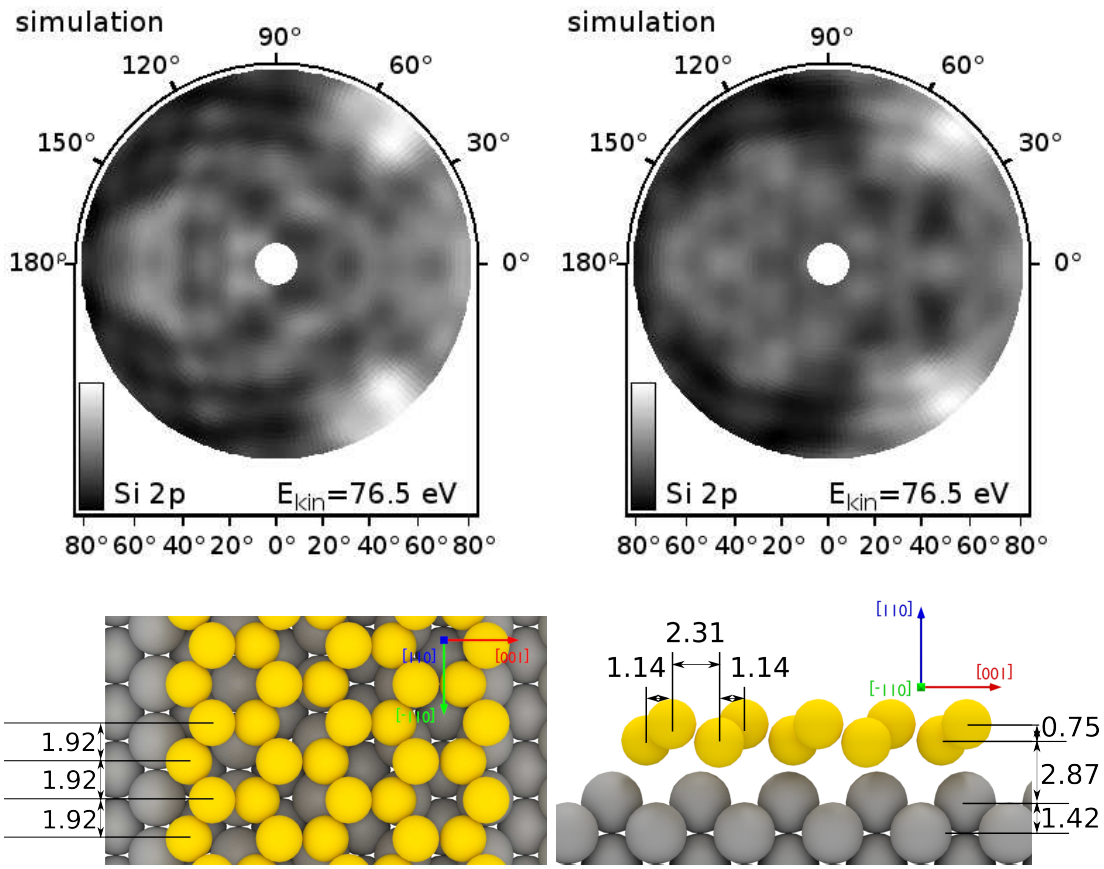

Figure 6.7: top row: Simulated XPD pattern of the structure model as proposed by Leandri [24] (left). The R-factor is $R_{\text{Leandri}} = 0.70$. Simulated XPD pattern of the structure model after the genetic algorithm was utilized to adjust the structure model (right). The resulting R-factor is $R = 0.62$. bottom row: Top (left) and side (right) view of the structure model resulted from the genetic algorithm.

width in [001] direction. The resulting structure model after the genetic algorithm was applied is shown in figure 6.7(bottom row). The corresponding simulated XPD pattern is shown in figure 6.7(top row, right). The agreement between the experimental and simulated XPD pattern is still poor as evidenced by the R-factor of $R = 0.62$. The symmetry properties remain unchanged, although the R-factor was slightly improved. Thus, the structure model proposed by Leandri is not appropriate for describing the local order within the silicon nano-ribbons.
The symmetry properties of the simulated XPD pattern can be understood by

analyzing the proposed structure model. As shown in figure 6.7(bottom row) the model proposed by Leandri solely reveals one mirror axis with its normal pointing along the $[\bar{1}10]$ direction. This is in agreement with the single mirror axis observed in the simulated XPD pattern. Even a modification of the proposed structure by either adding six silicon atoms to the unit cell or removing six silicon atoms from the unit cell does not generate a second mirror axis with its normal pointing along the [001] direction. Additionally, the width of the nano-ribbons of about 1.6 nm as deduced from STM measurements does not fit to the modified structure models as shown in figure 6.8. Further, the simulated XPD pattern results in R-factors of $R = 0.51$ and $R = 0.36$ for the extended and the reduced structure model, respectively.

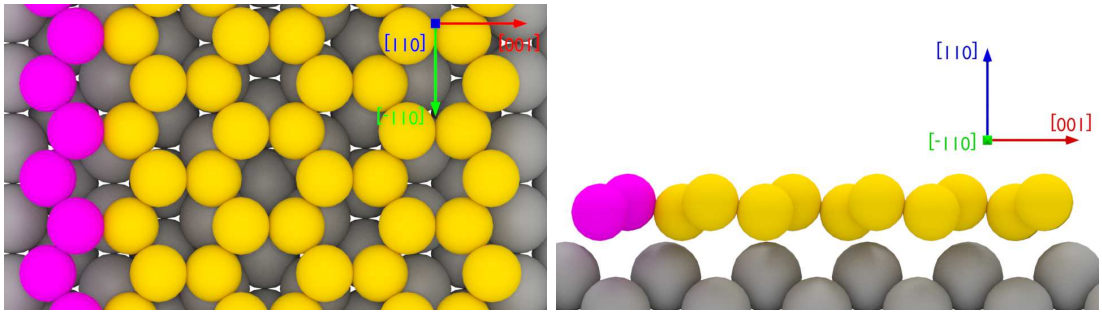

Figure 6.8: Top (left) and side view (right) of the modified structure model showing six additional atoms colored in magenta. A second mirror axis with its normal pointing along the [001] direction seems to be present in top view, but due to the buckling it becomes clear that this is not the case.

Based on the asymmetric structure model proposed by Leandri it is reasonable to assume two mirrored domains of silicon nano-ribbons following the symmetry of the (1×1)-reconstructed Ag(110) substrate. The simulated XPD pattern resulting from the structure model with two mirrored domains is shown in figure 6.9. The symmetry properties are now in agreement with the observed symmetry properties of the experimental pattern. Though, the R-factor of $R = 0.46$ still indicates poor agreement between simulated and experimental XPD pattern. Again, the genetic algorithm is utilized to rearrange the structure model and thereby care is taken that the applied rearrangements obey the symmetry properties. This resulted in

an XPD pattern shown in figure 6.9 with an R-factor of $R = 0.28$. Still the agreement is very poor.

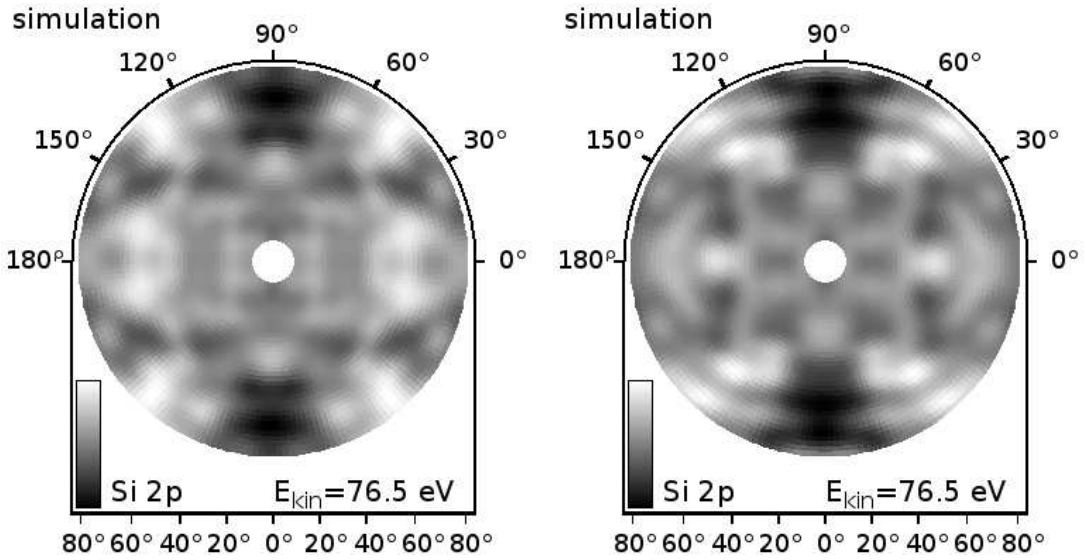

Figure 6.9: Simulated XPD pattern of the structure model as proposed by Leandri assuming two mirrored domains (left) [24]. The R-factor is $R = 0.46$. Simulated XPD pattern of the two domain structure model after the genetic algorithm was utilized (right). The resulting R-factor was $R = 0.28$.

The non-uniform corrugation along the [001] direction as proposed by Aufray *et al* also failed describing the structure of the nano-ribbons. Different types of corrugation were tried, while utilizing the genetic algorithm, i.e. sinusoidal, parabolic, gaussian, lorentzian, or voigt-type corrugation. Still, none of the presumed corrugations yielded an simulated XPD pattern that matches the experimental pattern.

Model proposed by He

The simulated XPD pattern corresponding to the most stable structure as proposed by He [25] is shown in 6.10. There are twelve emitting silicon atoms within the unit cell each with a different structural environment. In total the atomic cluster includes about 800 silicon and silver atoms. The simulated XPD pattern

shows two mirror axes and a two-folded symmetry which is in agreement with the experimental pattern. Although the symmetry properties agree between the simulated and experimental XPD pattern the R-factor of $R_{\mathrm{He}} = 0.65$ indicates poor agreement. The genetic algorithm is applied in order to improve the agreement between the simulated and experimental XPD pattern. Again, the allowed structural modifications include the shift of the Ag(110) substrate in [110], [001], and [$\bar{1}$10] direction relatively to adsorbed silicon atoms, the variation of the distance between the eight silicon atoms in the bottom layer and the two silicon dimers in the top layer in [110] direction, and the bonding length of the silicon dimers. Further, the silicon dimers are each allowed to rotate around their center of mass with the rotation axes pointing along the [110] direction. This results in the XPD pattern shown in figure 6.10(top row, right) with an R-factor of $R = 0.26$. The two-folded symmetry and two mirror axes are preserved. Four out of six features corresponding to high positive anisotropy values are rudimentary reproduced in comparison to the experimental XPD pattern, and both features corresponding to high negative anisotropy values are reproduced also. Overall, the simulated XPD patterns of the structure model proposed by He does not match the experimental data. Moreover, the R-factor resulting from the analysis of 17 further proposed structure models by He are tabulated in table 6.3. As represented by the R-factors in table 6.3 none of the proposed structure models is suitable for describing the local order within the silicon nano-ribbons.

Model proposed by Tchalala

The XPD pattern corresponding to the structure model as proposed by Tchalala *et al* is shown in figure 6.11. There are 14 emitting silicon atoms within a unit cell and in total the atomic cluster includes about 1000 silver and silicon atoms. The two-folded symmetry and the two mirror axes are in agreement with the experimental XPD pattern. Further, there exist in total six features corresponding to high positive anisotropy values which is in agreement with the experimental pattern. Though, the position of these maxima is rotated by about 90° relative to the experimental pattern. This results in an R-factor of $R_{\mathrm{Tchalala}} = 1.28$. The allowed structural modifications that are considered while utilizing the genetic algorithm include the shift of the substrate in [110], [001], and [$\bar{1}$10] direction in relation

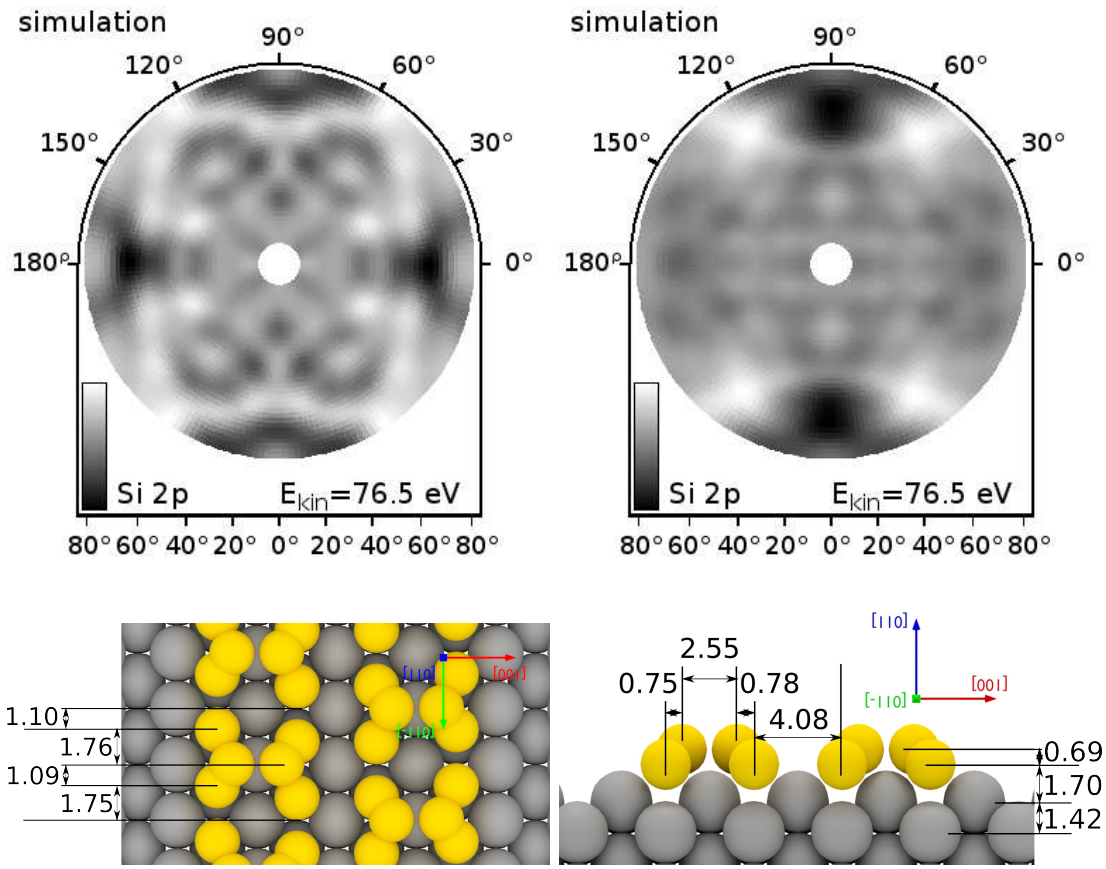

Figure 6.10: top row: Simulated XPD pattern of the structure model as proposed by He (left) [25]. The R-factor is $R_{\mathrm{He}} = 0.65$. Simulated XPD pattern of the structure model after the genetic algorithm was utilized (right) to adjust the structure model. The resulting R-factor was $R = 0.26$. bottom row: Top (left) and side view (right) of the structure model resulted from the genetic algorithm.

to the adsorbed silicon atoms. Further, the distance between the silver substrate and the adsorbed silicon atoms is varied, as well as the buckling in [110] direction, and the nano-ribbon's width in [001] direction. This results in an XPD pattern shown in figure 6.11(top row, right). The agreement between the experimental and simulated XPD pattern is still poor as indicated by an R-factor of $R = 0.84$. The structure model proposed by Tchalala *et al* is not appropriate for describing the local order within the nano-ribbons.

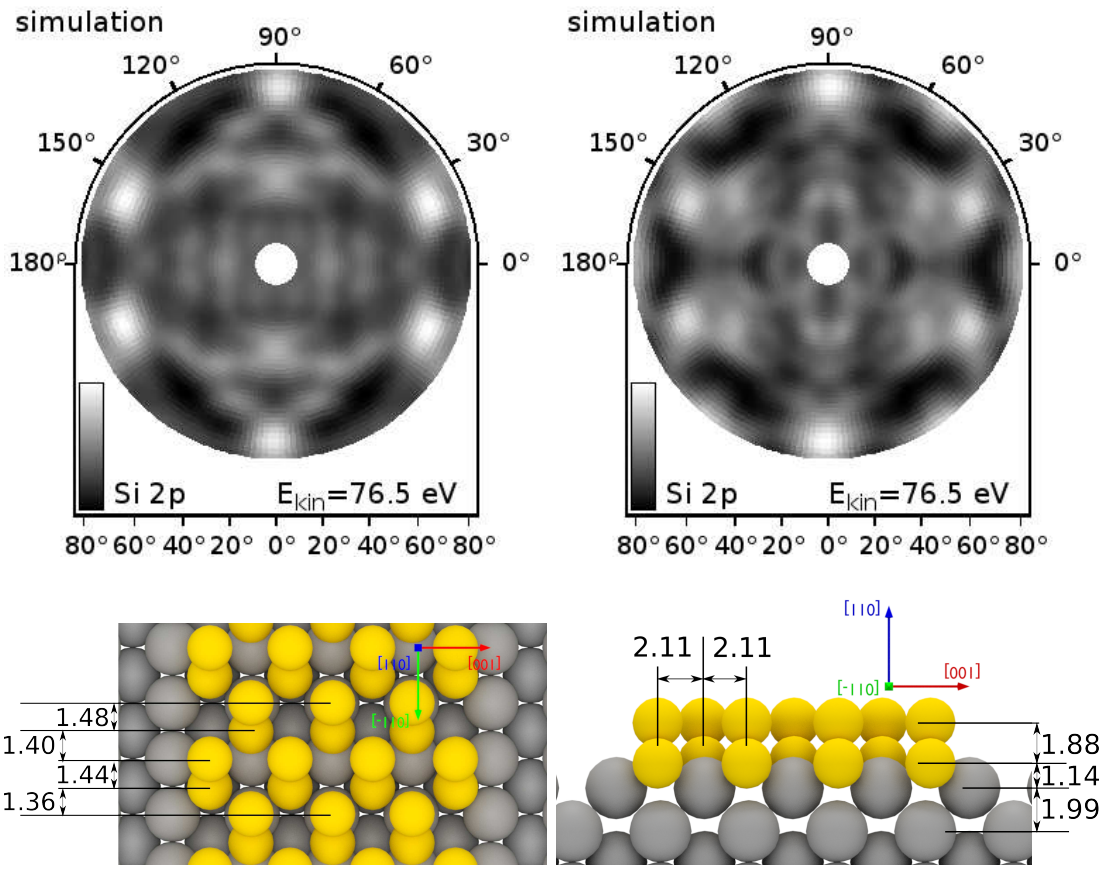

Figure 6.11: top row: Simulated XPD pattern of the structure model as proposed by Tchalala *et al* [32] (left). The R-factor is $R_{\text{Tchalala}} = 1.28$. Simulated XPD pattern of the structure model after the genetic algorithm was utilized (right) to adjust the structure model. The resulting R-factor was $R = 0.84$. bottom row: Top (left) and side view (right) of the structure model resulted from the genetic algorithm.

Model proposed by Hogan

Hogan *et al* proposed a structure model consisting of eight emitting silicon atoms within a unit cell. The corresponding XPD pattern is shown in figure 6.12. In total about 800 silicon and silver atoms are included in the atomic cluster used for the simulation. The symmetry properties of the simulated XPD pattern are in agreement with the experimental pattern. The R-factor given by a value of $R_{\text{Hogan}} = 0.83$ indicates a poor agreement. During the genetic algorithm the sub-

strate is allowed to rearrange in [110], [001], and [$\bar{1}$10] direction in relation to the adsorbed silicon atoms, the four lower lying silicon atoms are allowed to rearrange in [110] direction, and each of the four remaining silicon atoms are allowed to rearrange individually in [110], [001], and [$\bar{1}$10] direction. This results in an XPD pattern shown in figure 6.12(top row, right) with an R-factor of $R = 0.21$. The symmetry properties are preserved, indeed only two out of six features corresponding to high anisotropy values are roughly reproduced.

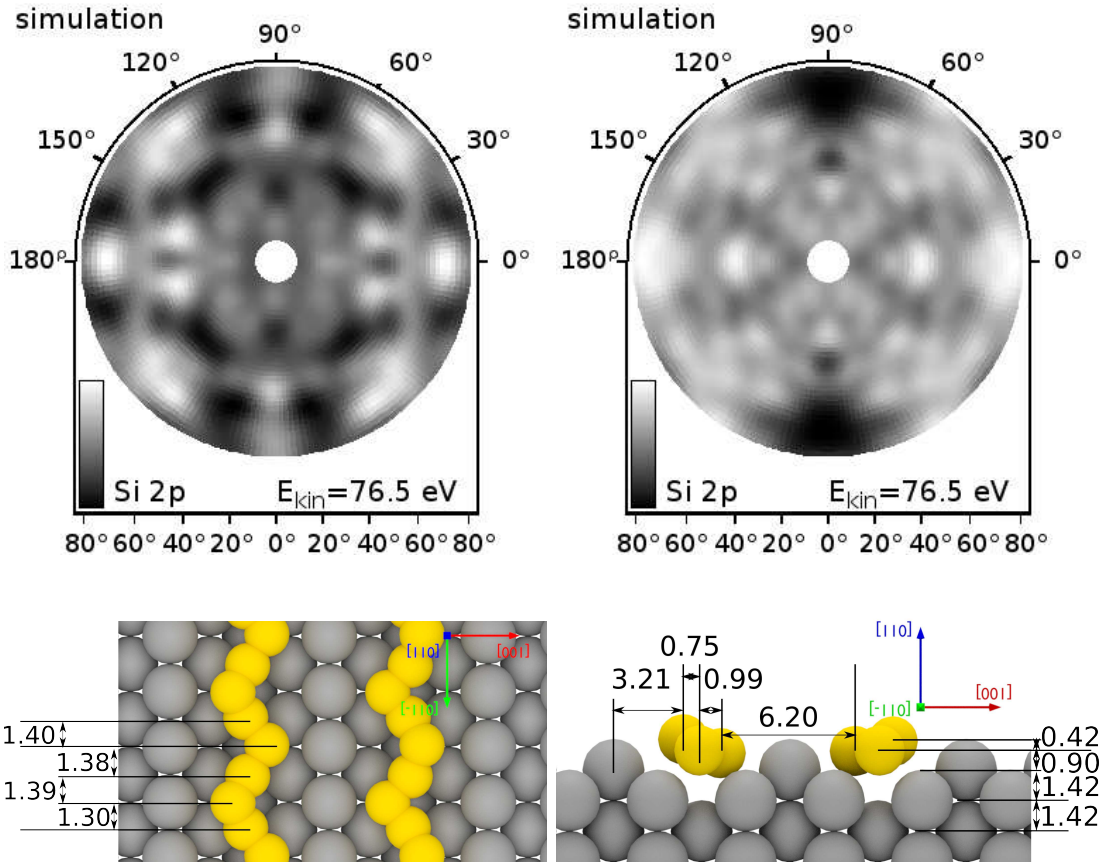

Figure 6.12: top row: Simulated XPD pattern of the structure model as proposed by Hogan *et al* [27] (left). The R-factor is $R_{\text{Hogan}} = 0.83$. Simulated XPD pattern of the structure model after the genetic algorithm was utilized (right) to adjust the structure model. The resulting R-factor was $R = 0.21$. bottom row: Top (left) and side view (right) of the structure model resulted from the genetic algorithm.

Model proposed by Prevot and Cerda

Both Prevot *et al* and Cerda *et al* propose a structure model that is characterized by a pentagonal structure. Differences between the proposed structure models include the bonding angles and distances within the pentagonal shape, the substrate to adsorbate distance, and the buckling value. Both structure models have the same orientation with respect to the substrate in $[\bar{1}10]$ and [001] direction. There are twelve emitting silicon atoms within a unit cell and in total about 800 silicon and silver atoms in the atomic cluster. The XPD patterns of the structure models proposed by Prevot *et al* and Cerda *et al* are shown in figure 6.13(top row) with an R-factor of $R_{\text{Prevot}} = 0.78$ corresponding to the structure model proposed by Prevot *et al*, and $R_{\text{Cerda}} = 0.66$ corresponding to the structure model proposed by Cerda *et al*. Applying the genetic algorithm resulted in an XPD pattern shown in figure 6.14(top row, right) and a structure model shown in figure 6.14(bottom row). The two-folded symmetry and two mirror axes are in agreement with the experimental XPD pattern. The positions of the features corresponding to both extremely high and low anisotropy values match the positions of the features within the experimental XPD pattern, accordingly the R-factor of $R = 0.09$ proves great agreement between the experimental and the simulated XPD pattern. Additionally, the "C"-shaped variations in the anisotropy of the experimental XPD pattern are perfectly reproduced by the simulated XPD pattern.

The resulting structure is characterized by two missing rows and its pentagonal nature. This is an analogy to the structure models as proposed by Prevot *et al* and Cerda *et al*. Still, significant differences between the proposed structure models and the resulting structure model after the genetic algorithm was applied are observed. Prevot *et al* give precise locations of individual silicon and silver atoms, although they explicitly claim that they are not sensitive to the orientation between the Ag(110) substrate and the silicon nano-ribbons in $[\bar{1}10]$ direction. In comparison to the proposed pentagonal structure models by Prevot *et al* and Cerda *et al*, the nano-ribbon to substrate distance in [110] direction is increased by 1.16 Å to a value of 1.91 ± 0.08 Å, the buckling is increased by 0.45 Å to 0.80 Å, and the substrate has to be shifted by 1.45 Å along the $[\bar{1}10]$ direction for matching experimental and simulated data [82].

The structure found by the analysis of the XPD pattern is in perfect agreement

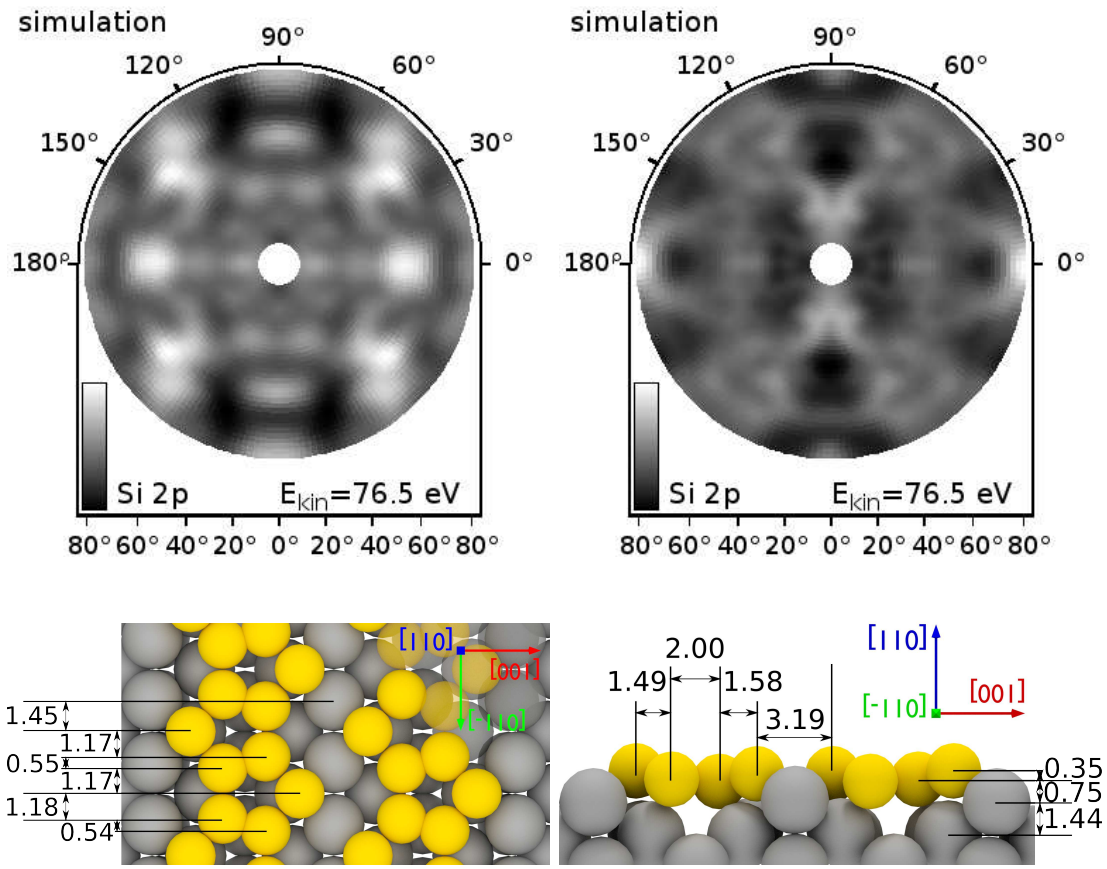

Figure 6.13: top row: Simulated XPD pattern of the structure model as proposed by Prevot *et al* [37] (left). The *R*-factor is $R_{\text{Prevot}} = 0.78$. Simulated XPD pattern of the structure model as proposed by Cerda *et al* [28] (right). The *R*-factor is $R_{\text{Cerda}} = 0.66$. bottom row: Top (left) and side view (right) of the structure model as proposed by Prevot [82].

with the results deduced from the XPS analysis in chapter 6.2.1. The distance of 1.91Å between the Ag(110) substrate and the silicon nano-ribbon indicates a weak bonding. This perfectly agrees with the unchanged line shape of the Ag 3d core-level signal before and after the deposition of silicon on the Ag(110) substrate. Further, silicon atoms with two distinct chemical environments can be found within the pentagonal structure. Four out of twelve silicon atoms within a unit cell are neighboured by two silicon atoms and eight out of twelve silicon atoms are neighboured by three silicon atoms. This perfectly fits to the two chemically shifted components within the Si 2p core-level signal.

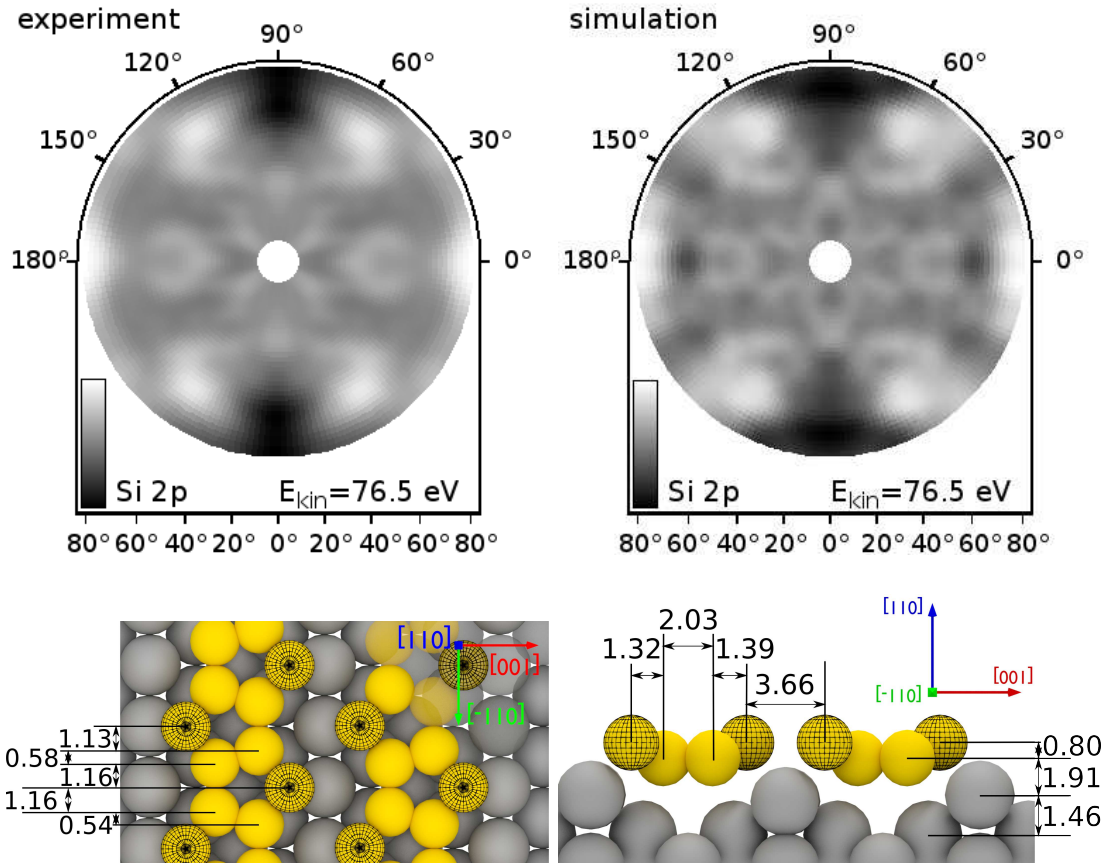

Figure 6.14: top row: Experimental XPD pattern of the Si 2p signal on Ag(110) taken at a kinetic energy of $E_{\mathrm{kin}} = 76.5\,\mathrm{eV}$ (left). Simulated XPD pattern of the pentagonal structure model after the genetic algorithm was utilized (right) to adjust the structure model. The R-factor is $R = 0.09$. bottom row: Top (left) and side view (right) of the resulting regular buckled pentagonal structure model as used for the simulated XPD patterns. The atomic locations are the averaged locations gained by the two distinct XPD pattern at incoming photon energies of $h\nu = 180\,\mathrm{eV}$ and $h\nu = 140\,\mathrm{eV}$. The silicon atoms depicted in pure yellow correspond to the component C1, and the silicon atoms depicted with an additional black wireframe correspond to the component C2 [82].

As a final proof a second XPD pattern was recorded at an incoming photon energy of $h\nu = 140\,\text{eV}$ corresponding to a kinetic energy of $E_{\text{kin}} = 36.5\,\text{eV}$. The pattern was recorded with an increased energy resolution, thus the integral XPD pattern can be deconvolved into two XPD patterns. The two patterns correspond to the chemically shifted components C1 and C2 as shown in the XPS spectra in figure 6.5.

The XPD pattern recorded at $E_{\text{kin}} = 36.5\,\text{eV}$ is shown in figure 6.15 and reveals

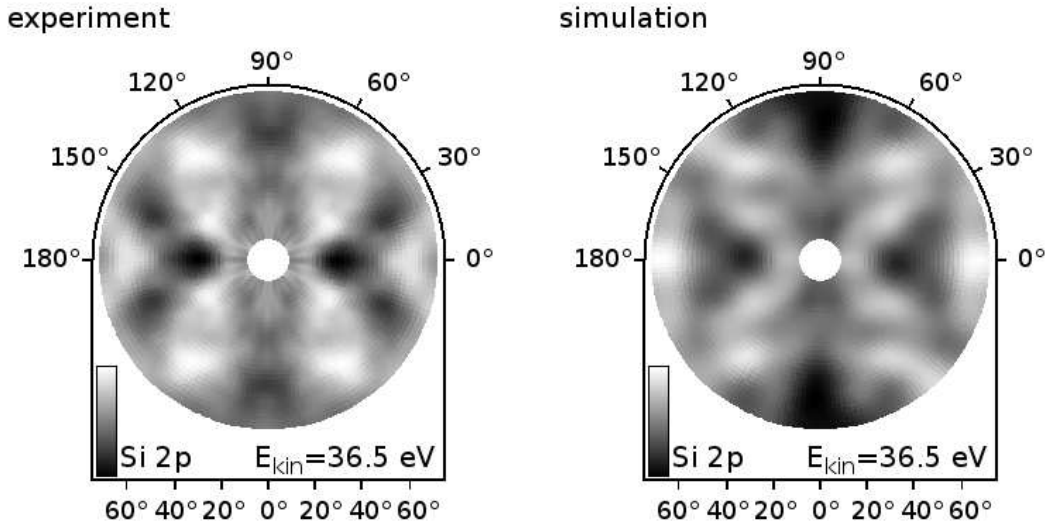

Figure 6.15: Experimental XPD pattern of the Si 2p signal on Ag(110) taken at a kinetic energy of $E_{\text{kin}} = 36.5\,\text{eV}$ (left). Simulated XPD pattern of the pentagonal structure model after the genetic algorithm was utilized (right) to adjust the structure model. The R-factor is $R = 0.10$ [82].

the same symmetry properties as the XPD pattern recorded at $E_{\text{kin}} = 76.5\,\text{eV}$. These are in particular the two-folded symmetry and two mirror axes. The two XPD pattern resulting from the deconvolution are shown in figure 6.16. The symmetry properties of the deconvolved XPD pattern are preserved, indicating that the deconvolution process yields reliable results. A genetic algorithm was re-applied in order to match experimental and simulated data after the deconvolution process. Therefore, the individual atoms are allowed to rearrange in all three spatial directions within a range of $\pm 0.1\,\text{Å}$. The pentagonal structure model with two missing rows as found by the analysis of the XPD pattern recorded at a kinetic energy of $E_{\text{kin}} = 76.5\,\text{eV}$ is the starting structure. The genetic algorithm is

combined with a permutation of the twelve different emitting silicon atoms within a unit cell in order to reveal the origin of the two chemically shifted components. This procedure finally provides three simulated XPD pattern. One XPD pattern is given by incoherent superposition of all twelve different emitting silicon atoms within the unit cell and shown in figure 6.15(right). The R-factor analysis provides a value of $R = 0.10$ indicating a perfect agreement. A second XPD pattern is given by the incoherent superposition of four emitting silicon atoms neighboured by only two silicon atoms and the corresponding pattern is shown in figure 6.16(bottom row). These silicon atoms are depicted with a black wireframe in figure 6.14. The third XPD pattern is given by the incoherent superposition of the eight remaining silicon atoms within the unit cell. These eight silicon atoms are each neighboured by three silicon atoms and the corresponding XPD pattern is shown in figure 6.16(top row). The comparison of the two deconvolved experimental XPD pattern and the two XPD pattern generated by the four or rather eight silicon atoms reveals the origin of the chemically shifted components. The R-factor describing the agreement between the XPD pattern shown in figure 6.16(top row, left) and the simulated XPD pattern generated by eight emitting silicon neighboured by three silicon atoms shown in figure 6.16(top row, right) is $R_{\mathrm{C1}} = 0.11$. The R-factor describing the agreement between the XPD pattern shown in figure 6.16(bottom row, left) and the simulated XPD pattern generated by the four emitting silicon atoms neighboured by two silicon atoms shown in figure 6.16(bottom row, right) is $R_{\mathrm{C2}} = 0.12$. Thus, the silicon atoms neighboured by only two silicon atoms correspond to component C2 from the XPS spectrum, and the silicon atoms that are neighboured by three silicon atoms correspond to component C1 from the XPS spectrum [82].

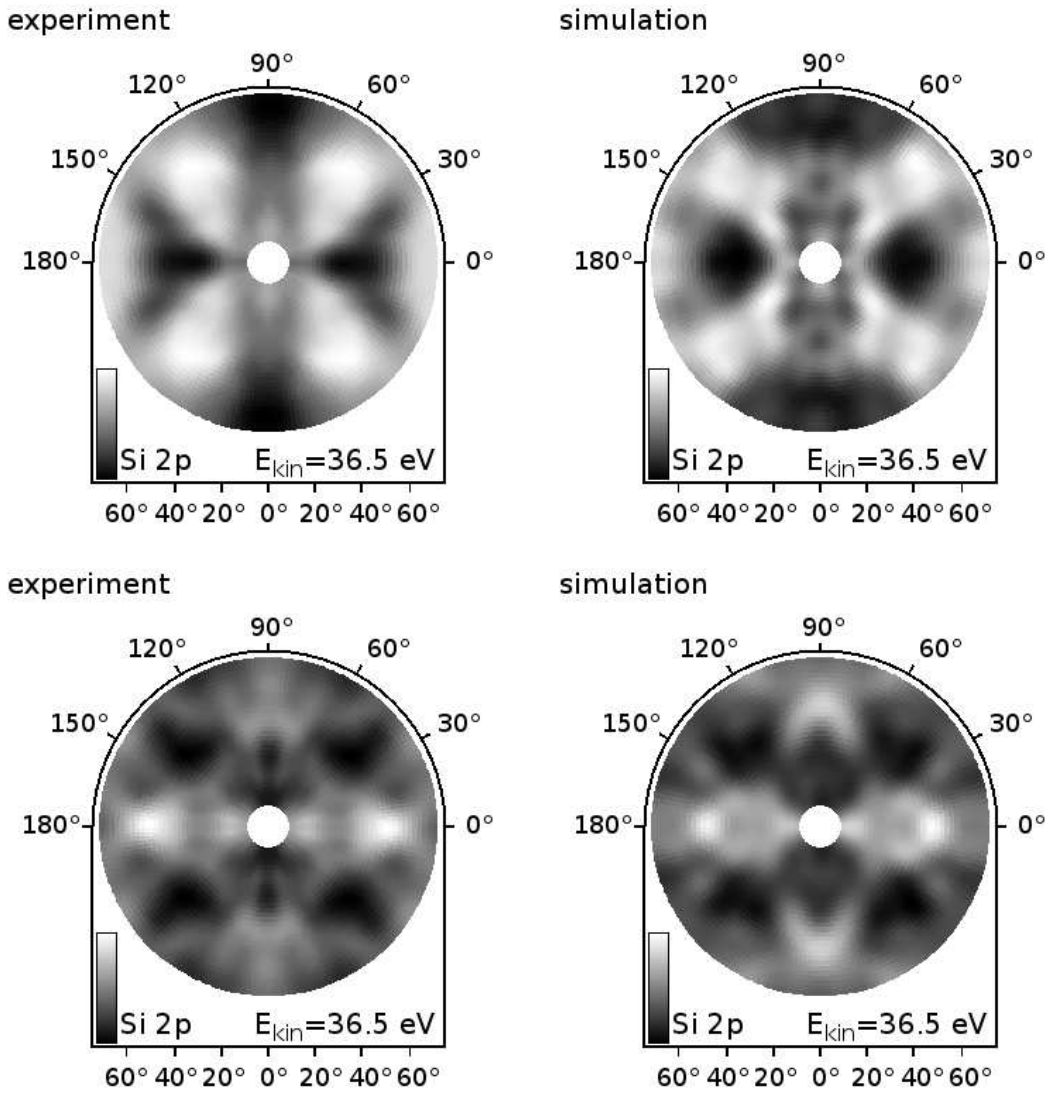

Figure 6.16: top row: Resulting XPD pattern of the deconvolution procedure for component C1 of the measured (left), and best simulated (right) XPD pattern of the Si 2p core-level signal. The R-factor is $R_{\mathrm{C1}} = 0.11$. bottom row: Resulting XPD pattern of the deconvolution procedure for component C2 of the measured (left), and best simulated (right) XPD pattern of the Si 2p core-level signal. The R-factor is $R_{\mathrm{C2}} = 0.12$. The experimental pattern was recorded with an incoming photon energy of $h\nu = 140\,\mathrm{eV}$. The best simulated XPD pattern is based on the Pentamer structure [82].

author	name	R-factor as proposed	R-factor after genetic algorithm
Leandri [24]	honeycomb, zig-zag	0.70	0.62
Leandri [24]	honeycomb, zig-zag, 2 domains	0.46	0.28
Leandri [24]	extended, +6		0.51
Leandri [24]	extended, +6, 2 domains		0.38
Leandri [24]	reduced, -6		0.36
Leandri [24]	reduced, -6, 2 domains		0.32
Aufray *et al* [26]	honeycomb, zig-zag, corrugated		0.24
He [25]	a1		0.42
He [25]	b1		0.35
He [25]	c1		0.28
He [25]	d1		0.28
He [25]	e1		0.28
He [25]	f1		0.33
He [25]	g1	0.65	0.26
He [25]	g2		0.25
He [25]	g3		0.19
He [25]	g4		0.20
He [25]	g5		0.19
He [25]	h1		0.37
He [25]	j1		0.44
He [25]	j2		0.34
He [25]	j3		0.26
He [25]	j4		0.45
He [25]	j5		0.22
He [25]	k1		0.36

Table 6.3: Summary of the R-factors of the simulated XPD pattern compared to the experimental XPD pattern recorded at an incoming photon energy of $h\nu = 180\,\mathrm{eV}$ of the structure models as proposed and after application of the genetic algorithm. See table 6.4 for continuing.

author	name	R-factor as proposed	R-factor after genetic algorithm
Tchalala *et al* [32]	arm-chair	1.28	0.84
Hogan *et al* [27]	1MR-DNR-a		0.25
Hogan *et al* [27]	1MR-DNR-b		0.37
Hogan *et al* [27]	2MR-DNR-a	0.83	0.21
Hogan *et al* [27]	2MR-DNR-b		0.26
Hogan *et al* [27]	3MR-DNR-a		0.32
Hogan *et al* [27]	BT-DNR		0.54
Hogan *et al* [27]	BT-e1		0.31
Prevot *et al* [37]	Pentamer chain	0.78	0.09
Cerda *et al* [28]	Pentamer chain	0.66	0.09

Table 6.4: Continuation from table 6.3. Summary of the R-factors of the simulated XPD pattern compared to the experimental XPD pattern recorded at an incoming photon energy of $h\nu = 180\,\mathrm{eV}$ of the structure models as proposed and after application of the genetic algorithm.

7 Conclusion and Outlook

In this thesis the successful preparation of (5 × 2)-reconstructed silicon nano-ribbons onto a (1 × 1)-reconstructed Ag(110) substrate and a comprehensive analysis of the structural and chemical properties of the sample were reported. Silicon nano-ribbons belong to the still emerging class of low-dimensional, in particular to the class of one-dimensional materials that open new perspectives for fundamental science as well as technological applications. A precise knowledge of the nano-ribbons' structural composition and its interaction with the substrate is of highest importance for an encompassing understanding. There are more than 30 structure models proposed to describe the local order within the nano-ribbon. Thus, surface sensitive XPS and XPD measurements were performed to determine the precise atomic locations and to face the interaction between the nano-ribbons and the substrate.

For this purpose, initially the (1 × 1)-reconstructed Ag(110) was analyzed by LEED, XPS, and XPD measurements. From the LEED and XPS measurements the proper preparation was deduced. The absence of signals corresponding to oxygen and carbon and the presence of surface plasmons proved the carefully cleaned Ag(110) surface. Further, the high-resolution XPS spectrum revealed a single chemical state for the Ag 3d core-level signal as the spectrum can be fitted with only one component. From the structural point of view it was concluded from the XPD measurements that there is only relaxation in $[\bar{1}10]$ direction of the three topmost layers of the Ag(110) crystal.
A distinct amount of silicon was evaporated by a direct current heater onto the (1 × 1)-reconstructed Ag(110) single crystal, throughout the Ag(110) crystal was annealed to 500 K. The deposition rate was previously specified by a QCM and the sample temperature was monitored by a pyrometer. LEED measurements showed

the characteristic (5×2)-reconstruction regarding to the bare Ag(110) substrate. Additionally, distinctive signatures of the Si 2p core-level signal and the valence band spectrum proved the successful growth of silicon nano-ribbons.
First, the interaction between the silicon nano-ribbons and the Ag(110) substrate was analyzed. Therefore, XPS signals of the Ag 3d core-level after the growth of silicon nano-ribbons were recorded. The comparison clearly showed that the line shape of the Ag 3d core-level signal remains unchanged before and after silicon deposition. Thus, it is concluded, that there is no strong chemical bonding between the silicon nano-ribbons and the Ag(110) substrate beneath.
The XPS signal of the Si 2p core-level consists of two chemically shifted components. From a comparison with literature it was concluded, that the sample is entirely covered with extremely elongated silicon nano-ribbons and no other silicon configuration was present.
Two XPD patterns of the Si 2p core-level signal were recorded at incoming photon energies of 180 eV and 140 eV in order to determine the local order within the nano-ribbons and their orientation regarding the Ag(110) substrate. Subsequently, by the comparison of simulated XPD pattern and the XPD pattern recorded at an incoming photon energy of $h\nu = 180\,\text{eV}$ more than 30 structure models were evaluated. None of the proposed structure models showed a sufficient agreement in comparison to the measured XPD pattern. Thus, structural modifications were applied to the proposed structure models while preserving their characteristic structural properties like symmetry or the number of emitting atoms within a unit cell. As a result, one structure model was presented that perfectly fits to the recorded XPD pattern. The structure can be characterized by its exceptional pentagonal shape and formation of two missing rows. Thus, one third of the silicon atoms are neighboured by two silicon atoms, and two third of the silicon atoms are neighboured by three silicon atoms. Further, the distance between the Ag(110) substrate and the silicon nano-ribbons was determined to be 1.91 Å. This large distance validates the weak bonding between the Ag(110) substrate and the silicon nano-ribbons which is in agreement with the analysis of the Ag 3d core-level signals.
Hiraoka *et al* reported the lifting of a silicon nano-ribbon from a Ag(110) surface by a STM tip [42,43]. Feng *et al* reported the disappearance of the nano-ribbons after mild annealing of the sample to about 700 K [34]. Both observations are explained

by the weak bonding between the nano-ribbons and the Ag(110) substrate. This provides a major insight into the system as comparable systems like silicon nano-ribbons on Au(110), silicene sheets on Ag(111), or germanene sheets on Au(111) reveal a strong bonding between the adsorbate and the substrate [173–175].
Finally, the Si 2p XPD pattern recorded at an incoming photon energy of $h\nu = 140\,\mathrm{eV}$ were deconvolved into the two chemically shifted components C1 and C2. Thus, by combining the chemical information from the XPS spectra and the structural information from the XPD pattern it was possible to assign the origin of the two chemically shifted components. The component C1 originates from silicon atoms with three neighbours and the component C2 originates from silicon atoms with two neighbours.
The local order of silicon nano-ribbons is of highest interest from a fundamental point of view. Currently, the research in carbon-based buckyballs that are partly build from pentagons received great attention due to its high degree of spin polarization [176]. Owing to the higher mass of silicon and compared to carbon even larger spin-orbit enhanced effects are expected and will open new routes for accessing exotic phenomena [28]. Since silicon nano-ribbons are actually the only known silicon allotrope that is solely composed of pentagons it can potentially serve as an ideal model system for larg spin-orbit induced effects.
Further, the unexpected pentagonal nature of silicon nano-ribbons revives the discussion of the nano-ribbons' band structure. Only very few works dealing with the nano-ribbons' band structure are reported yet and the drawn conclusions are based on hexagonally arranged nano-ribbons [71, 177]. Keeping the pentagonal structure and weak bonding to the substrate in mind the reported band structure will be seen in a new light. The structure model presented in this thesis provides precise atomic locations and therefore, yields a reliable framework for theoretical calculations aiming on electronic, magnetic, and spin-orbit based effects.
Finally, the presented results are of utmost importance for the development of applications. The result of weakly bonded silicon nano-ribbons to the Ag(110) substrate will enhance the interest in transferring the nano-ribbons to an insulating substrate. The transfer is necessary for the fabrication of electronic devices since metallic substrates like Ag(110) are unsuitable templates for electronic devices. Comparable systems like two-dimensional silicene sheets on Ag(111) have been transferred to insulating substrates already [178]. The deduced weak inter-

action will pave the way for the transfer of silicon nano-ribbons to an insulating substrate.

The similarities between silicon and germanium on the one hand, and Ag(110) and Au(110) on the other hand rises interest in composite structures comparable to one-dimensional silicon nano-ribbons on Ag(110). The growth of silicon nano-ribbons on Au(110) has been reported already [174]. Though, it is not known whether the nano-ribbons on Au(110) share their structural characteristics with silicon nano-ribbons on Ag(110).
The growth of germanium nano-ribbons on any substrate has not been reported yet. Thus, a successful growth of these germanium nano-ribbons would break new ground. Keeping the structural characteristics of nano-ribbons built of carbon and silicon in mind, the research on germanium nano-ribbons can provide a more encompassing insight into the system of growth of nano-ribbons built from group IV elements.

Bibliography

[1] K. S. Novoselov, A. K. Geim, S. V. Morozov, D. Jiang, Y. Zhang, S. V. Dubonos, I. V. Grigorieva and A. A. Firsov, *Electric Field Effect in Atomically Thin Carbon Films*, Science **306**, 666 (2004).

[2] J. Moser, A. Barreiro and A. Bachtold, *Current-induced cleaning of graphene*, Applied Physics Letters **91**, 163513 (2007).

[3] C. Lee, X. Wei, J. W. Kysar and J. Hone, *Measurement of the Elastic Properties and Intrinsic Strength of Monolayer Graphene*, Science **321**, 385 (2008).

[4] R. R. Nair, P. Blake, A. N. Grigorenko, K. S. Novoselov, T. J. Booth, T. Stauber, N. M. R. Peres and A. K. Geim, *Fine Structure Constant Defines Visual Transparency of Graphene*, Science **320**, 1308 (2008).

[5] S. Bae, H. Kim, Y. Lee, X. Xu, J.-S. Park, Y. Zheng, J. Balakrishnan, T. Lei, H. R. Kim, Y. I. Song, Y.-J. Kim, K. S. Kim, B. Özyilmaz, J.-H. Ahn, B. H. Hong and S. Iijima, *Roll-to-roll production of 30-inch graphene films for transparent electrodes*, Nature Nanotechnology **5**, 574 (2010).

[6] S.-J. Han, A. V. Garcia, S. Oida, K. A. Jenkins and W. Haensch, *Graphene radio frequency receiver integrated circuit*, Nature Communications **5**, 3086 (2014).

[7] Y. Shao, J. Wang, H. Wu, J. Liu, I. Aksay and Y. Lin, *Graphene Based Electrochemical Sensors and Biosensors: A Review*, Electroanalysis **22**, 1027 (2010).

[8] S. S. Varghese, S. Lonkar, K. Singh, S. Swaminathan and A. Abdala, *Recent advances in graphene based gas sensors*, Sensors and Actuators B: Chemical **218**, 160 (2015).

[9] A. H. Castro Neto, F. Guinea, N. M. R. Peres, K. S. Novoselov and A. K. Geim, *The electronic properties of graphene*, Reviews of Modern Physics **81**, 109 (2009).

[10] L. Shi and T. Zhao, *Recent advances in inorganic 2D materials and their applications in lithium and sodium batteries*, Journal of Materials Chemistry A **5**, 3735 (2017).

[11] G. R. Bhimanapati, Z. Lin, V. Meunier, Y. Jung, J. Cha, S. Das, D. Xiao, Y. Son, M. S. Strano, V. R. Cooper, L. Liang, S. G. Louie, E. Ringe, W. Zhou, S. S. Kim, R. R. Naik, B. G. Sumpter, H. Terrones, F. Xia, Y. Wang, J. Zhu, D. Akinwande, N. Alem, J. A. Schuller, R. E. Schaak, M. Terrones and J. A. Robinson, *Recent Advances in Two-Dimensional Materials beyond Graphene*, ACS Nano **9**, 11509 (2015).

[12] D. Jariwala, T. J. Marks and M. C. Hersam, *Mixed-dimensional van der Waals heterostructures*, Nature Materials **16**, 170 (2017).

[13] K. F. Mak, C. Lee, J. Hone, J. Shan and T. F. Heinz, *Atomically Thin MoS_2: A New Direct-Gap Semiconductor*, Physical Review Letters **105**, 136805 (2010).

[14] B. Aufray, B. Ealet, H. Jamgotchian, J.-H. Hoarau, J.-P. Biberian and H. Maradj, Growth of Silico Nano-ribbons on Ag(110): State of the Art, in *Silicene: Structure, Properties and Applications*, pages 183–202, Springer, Switzerland, 1st edition, 2016.

[15] S. Kravchenko, *Strongly Correlated Electrons in Two Dimensions*, Pan Stanford, Singapore, 1st edition, 2017.

[16] Y. Song, S. Chang, S. Gradecak and J. Kong, *Visibly-Transparent Organic Solar Cells on Flexible Substrates with All-Graphene Electrodes*, Advanced Energy Materials **6**, 1600847 (2016).

[17] M. Y. Han, B. Özyilmaz, Y. Zhang and P. Kim, *Energy Band-Gap Engineering of Graphene Nanoribbons*, Physical Review Letters **98**, 206805 (2007).

[18] Q. Cao, J. Tersoff, D. B. Farmer, Y. Zhu and S.-J. Han, *Carbon nanotube transistors scaled to a 40-nanometer footprint*, Science **356**, 1369 (2017).

[19] S. A. Wolf, D. D. Awschalom, R. A. Buhrman, J. M. Daughton, S. von Molnár, M. L. Roukes, A. Y. Chtchelkanova and D. M. Treger, *Spintronics: A Spin-Based Electronics Vision for the Future*, Science **294**, 1488 (2001).

[20] F. Iacopi, J. Boeckl and C. Jagadish, *2D Materials*, Academic Press, Cambridge, 1st edition, 2016.

[21] C. E. Nebel, *Valleytronics: Electrons dance in diamond*, Nature Materials **12**, 690 (2013).

[22] P. D. Padova, C. Ottaviani, F. Ronci, S. Colonna, B. Olivieri, C. Quaresima, A. Cricenti, M. E. Dávila, F. Hennies, A. Pietzsch, N. Shariati and G. L. Lay, *Mn-silicide nanostructures aligned on massively parallel silicon nanoribbons*, Journal of Physics: Condensed Matter **25**, 014009 (2013).

[23] M. Hortamani, L. Sandratskii, P. Kratzer and I. Mertig, *Searching for Si-based spintronics by first principles calculations*, New Journal of Physics **11**, 125009 (2009).

[24] C. Leandri, G. L. Lay, B. Aufray, C. Girardeaux, J. Avila, M. Dávila, M. Asensio, C. Ottaviani and A. Cricenti, *Self-aligned silicon quantum wires on Ag(110)*, Surface Science **574**, L9 (2005).

[25] G.-m. He, *Atomic structure of Si nanowires on Ag(110): A density-functional theory study*, Physical Review B **73**, 035311 (2006).

[26] B. Aufray, A. Kara, S. Vizzini, H. Oughaddou, C. Léandri, B. Ealet and G. L. Lay, *Graphene-like silicon nanoribbons on Ag(110): A possible formation of silicene*, Applied Physics Letters **96**, 183102 (2010).

[27] C. Hogan, S. Colonna, R. Flammini, A. Cricenti and F. Ronci, *Structure and stability of Si/Ag(110) nanoribbons*, Physical Review B **92**, 115439 (2015).

[28] J. I. Cerdá, J. Sławińska, G. L. Lay, A. C. Marele, J. M. Gómez-Rodríguez and M. E. Dávila, *Unveiling the pentagonal nature of perfectly aligned single- and double-strand Si nano-ribbons on Ag(110)*, Nature Communications **7**, 13076 (2016).

[29] R. Bernard, T. Leoni, A. Wilson, T. Lelaidier, H. Sahaf, E. Moyen, L. Assaud, L. Santinacci, F. Leroy, F. Cheynis, A. Ranguis, H. Jamgotchian, C. Becker, Y. Borensztein, M. Hanbücken, G. Prévot and L. Masson, *Growth of Si ultrathin films on silver surfaces: Evidence of an Ag(110) reconstruction induced by Si*, Physical Review B **88**, 121411 (2013).

[30] P. Lagarde, M. Chorro, D. Roy and N. Trcera, *Study by EXAFS of the local structure around Si on silicene deposited on Ag(110) and Ag(111) surfaces*, Journal of Physics: Condensed Matter **28**, 075002 (2016).

[31] C. Lian and J. Ni, *The structural and electronic properties of silicon nanoribbons on Ag(110): A first principles study*, Physica B: Condensed Matter **407**, 4695 (2012).

[32] M. R. Tchalala, H. Enriquez, A. J. Mayne, A. Kara, G. Dujardin, M. A. Ali and H. Oughaddou, *Atomic structure of silicene nanoribbons on Ag(110)*, Journal of Physics: Conference Series **491**, 012002 (2014).

[33] H. Sahaf, C. Léandri, E. Moyen, M. Macé, L. Masson and M. Hanbücken, *Growth of Co nanolines on self-assembled Si nanostripes*, Europhysics Letters **86**, 28006 (2009).

[34] B. Feng, H. Li, S. Meng, L. Chen and K. Wu, *Structure and quantum well states in silicene nanoribbons on Ag(110)*, Surface Science **645**, 74 (2016).

[35] A. Kara, S. Vizzini, C. Leandri, B. Ealet, H. Oughaddou, B. Aufray and G. LeLay, *Silicon nano-ribbons on Ag(110): a computational investigation*, Journal of Physics: Condensed Matter **22**, 045004 (2010).

[36] S. Cahangirov, M. Topsakal and S. Ciraci, *Armchair nanoribbons of silicon and germanium honeycomb structures*, Physical Review B **81**, 195120 (2010).

[37] G. Prévot, C. Hogan, T. Leoni, R. Bernard, E. Moyen and L. Masson, *Si Nanoribbons on Ag(110) Studied by Grazing-Incidence X-Ray Diffraction,*

Scanning Tunneling Microscopy, and Density-Functional Theory: Evidence of a Pentamer Chain Structure, Physical Review Letters **117**, 276102 (2016).

[38] R. Qin, C.-H. Wang, W. Zhu and Y. Zhang, *First-principles calculations of mechanical and electronic properties of silicene under strain*, AIP Advances **2**, 022159 (2012).

[39] T.-C. Wang, C.-H. Hsu, Z.-Q. Huang, F.-C. Chuang, W.-S. Su and G.-Y. Guo, *Tunable magnetic states on the zigzag edges of hydrogenated and halogenated group-IV nanoribbons*, Scientific Reports **6**, 39083 (2016).

[40] S. M. Aghaei, M. M. Monshi, I. Torres and I. Calizo, *Edge functionalization and doping effects on the stability, electronic and magnetic properties of silicene nanoribbons*, RSC Advances **6**, 17046 (2016).

[41] P. F. Yuan, Z. H. Zhang, Z. Q. Fan and M. Qiu, *Electronic structure and magnetic properties of penta-graphene nanoribbons*, Physical Chemistry Chemical Physics **19**, 9528 (2017).

[42] R. Hiraoka, *Effect of the contact states on electron transport of single molecule systems within an STM junction*, Dissertation, The University of Tokyo, 2015.

[43] R. Hiraoka, C.-L. Lin, K. Nakamura, R. Nagao, M. Kawai, R. Arafune and N. Takagi, *Transport characteristics of a silicene nanoribbon on Ag(110)*, Beilstein Journal of Nanotechnology **8**, 1699 (2017).

[44] G. Prévot, R. Bernard, H. Cruguel, A. Curcella, M. Lazzeri, T. Leoni, L. Masson, A. Ranguis and Y. Borensztein, *Formation of silicene on silver: Strong interaction between Ag and Si*, physica status solidi (b) **253**, 206 (2016).

[45] C. Westphal, *The study of the local atomic structure by means of X-ray photoelectron diffraction*, Surface Science Reports **50**, 1 (2003).

[46] D. Woodruff, *Adsorbate structure determination using photoelectron diffraction: Methods and applications*, Surface Science Reports **62**, 1 (2007).

[47] C. S. Fadley, The Study of Surface Structures by Photoelectron Diffraction and Auger Electron Diffraction, in *Synchrotron Radiation Research: Advances in Surface and Interface Science Techniques*, pages 421–518, Springer, Boston, 1st edition, 1992.

[48] A. Schuler, M. Greif, A. P. Seitsonen, G. Mette, L. Castiglioni, J. Osterwalder, and M. Hengsberger, *Sensitivity of photoelectron diffraction to conformational changes of adsorbed molecules: Tetra-tert-butylazobenzene/Au(111)*, Structural Dynamics **4** (2017).

[49] M. Greif, L. Castiglioni, A. P. Seitsonen, S. Roth, J. Osterwalder and M. Hengsberger, *Photoelectron diffraction in the x-ray and ultraviolet regime: Sn-phthalocyanine on Ag(111)*, Physical Review B **87**, 085429 (2013).

[50] L. H. de Lima, D. Handschak, F. Schonbohm, R. Landers, C. Westphal and A. de Siervo, *The atomic structure of a bare buffer layer on SiC(0001) chemically resolved*, Chemical Communications **50**, 13571 (2014).

[51] H. Matsui, F. Matsui, N. Maejima, T. Matsushita, T. Okamoto, A. N. Hattori, Y. Sano, K. Yamauchi and H. Daimon, *Local atomic configuration of graphene, buffer layer, and precursor layer on SiC(0001) by photoelectron diffraction*, Surface Science **632**, 98 (2015).

[52] D. Ferrah, J. Penuelas, C. Bottela, G. Grenet and A. Ouerghi, *X-ray photoelectron spectroscopy (XPS) and diffraction (XPD) study of a few layers of graphene on 6H-SiC(0001)*, Surface Science **615**, 47 (2013).

[53] L. H. de Lima, A. de Siervo, R. Landers, G. A. Viana, A. M. B. Goncalves, R. G. Lacerda and P. Häberle, *Atomic surface structure of graphene and its buffer layer on SiC(0001): A chemical-specific photoelectron diffraction approach*, Physical Review B **87**, 081403 (2013).

[54] D. Y. Kim, S. Stefanoski, O. O. Kurakevych and T. A. Strobel, *Synthesis of an open-framework allotrope of silicon*, Nature Materials **14**, 169 (2014).

[55] J. Gryko, P. F. McMillan, R. F. Marzke, G. K. Ramachandran, D. Patton, S. K. Deb and O. F. Sankey, *Low-density framework form of crystalline silicon with a wide optical band gap*, Physical Review B **62**, R7707 (2000).

[56] H. I. T. Hauge, M. A. Verheijen, S. Conesa-Boj, T. Etzelstorfer, M. Watzinger, D. Kriegner, I. Zardo, C. Fasolato, F. Capitani, P. Postorino, S. Kölling, A. Li, S. Assali, J. Stangl and E. P. A. M. Bakkers, *Hexagonal Silicon Realized*, Nano Letters **15**, 5855 (2015).

[57] J. Tang, J.-L. Maurice, F. Fossard, I. Florea, W. Chen, E. V. Johnson, M. Foldyna, L. Yu and P. R. i Cabarrocas, *Natural occurrence of the diamond hexagonal structure in silicon nanowires grown by a plasma-assisted vapour-liquid-solid method*, Nanoscale **9**, 8113 (2017).

[58] Y. Qiu, H. Bender, O. Richard, M.-S. Kim, E. V. Besien, I. Vos, M. de Potter de ten Broeck, D. Mocuta and W. Vandervorst, *Epitaxial diamond-hexagonal silicon nano-ribbon growth on (001) silicon*, Scientific Reports **5**, 12692 (2015).

[59] Y. Wang, K. Scheerschmidt and U. Gösele, *Theoretical investigations of bond properties in graphite and graphitic silicon*, Physical Review B **61**, 12864 (2000).

[60] G. G. Guzmán-Verri and L. C. L. Y. Voon, *Electronic structure of silicon-based nanostructures*, Physical Review B **76**, 075131 (2007).

[61] H. Nakano, T. Mitsuoka, M. Harada, K. Horibuchi, H. Nozaki, N. Takahashi, T. Nonaka, Y. Seno and H. Nakamura, *Soft Synthesis of Single-Crystal Silicon Monolayer Sheets*, Angewandte Chemie International Edition **45**, 6303 (2006).

[62] P. Vogt, P. De Padova, C. Quaresima, J. Avila, E. Frantzeskakis, M. C. Asensio, A. Resta, B. Ealet and G. Le Lay, *Silicene: Compelling Experimental Evidence for Graphenelike Two-Dimensional Silicon*, Physical Review Letters **108**, 155501 (2012).

[63] B. Feng, Z. Ding, S. Meng, Y. Yao, X. He, P. Cheng, L. Chen and K. Wu, *Evidence of Silicene in Honeycomb Structures of Silicon on Ag(111)*, Nano Letters **12**, 3507 (2012).

[64] C.-L. Lin, R. Arafune, K. Kawahara, N. Tsukahara, E. Minamitani, Y. Kim, N. Takagi and M. Kawai, *Structure of Silicene Grown on Ag(111)*, Applied Physics Express **5**, 045802 (2012).

[65] H. Jamgotchian, Y. Colignon, N. Hamzaoui, B. Ealet, J. Y. Hoarau, B. Aufray and J. P. Bibérian, *Growth of silicene layers on Ag(111): unexpected effect of the substrate temperature*, Journal of Physics: Condensed Matter **24**, 172001 (2012).

[66] D. Chiappe, C. Grazianetti, G. Tallarida, M. Fanciulli and A. Molle, *Local Electronic Properties of Corrugated Silicene Phases*, Advanced Materials **24**, 5088 (2012).

[67] S. Cahangirov, H. Sahin, G. L. Lay and A. Rubio, *Introduction to the Physics of Silicene and other 2D Materials*, Springer, Switzerland, 1st edition, 2017.

[68] P. De Padova, C. Quaresima, P. Perfetti, B. Olivieri, C. Leandri, B. Aufray, S. Vizzini and G. Le Lay, *Growth of Straight, Atomically Perfect, Highly Metallic Silicon Nanowires with Chiral Asymmetry*, Nano Letters **8**, 271 (2008).

[69] H. Sahaf, L. Masson, C. Léandri, B. Aufray, G. L. Lay and F. Ronci, *Formation of a one-dimensional grating at the molecular scale by self-assembly of straight silicon nanowires*, Applied Physics Letters **90**, 263110 (2007).

[70] F. Ronci, S. Colonna, A. Cricenti, P. De Padova, C. Ottaviani, C. Quaresima, B. Aufray and G. Le Lay, *Low temperature STM/STS study of silicon nanowires grown on the Ag(110) surface*, physica status solidi (c) **7**, 2716 (2010).

[71] P. D. Padova, C. Quaresima, C. Ottaviani, P. M. Sheverdyaeva, P. Moras, C. Carbone, D. Topwal, B. Olivieri, A. Kara, H. Oughaddou, B. Aufray and G. L. Lay, *Evidence of graphene-like electronic signature in silicene nanoribbons*, Applied Physics Letters **96**, 261905 (2010).

[72] P. D. Padova, C. Quaresima, B. Olivieri, P. Perfetti and G. L. Lay, *Strong resistance of silicene nanoribbons towards oxidation*, Journal of Physics D: Applied Physics **44**, 312001 (2011).

[73] P. D. Padova, C. Leandri, S. Vizzini, C. Quaresima, P. Perfetti, B. Olivieri, H. Oughaddou, B. Aufray and G. L. Lay, *Burning Match Oxidation Process of Silicon Nanowires Screened at the Atomic Scale*, Nano Letters **8**, 2299 (2008).

[74] E. Salomon, T. Angot, C. Thomas, J.-M. Layet, P. Palmgren, C. Nlebedim and M. Göthelid, *Etching of silicon nanowires on Ag(110) by atomic hydrogen*, Surface Science **603**, 3350 (2009).

[75] E. Salomon and T. Angot, *Modification of Physical Properties of Silicon Nanowires, Grown Onto Ag(110), by Selective Adsorption: From Atomic Hydrogen to Molecules*, Science of Advanced Materials **3**, 354 (2011).

[76] E. Salomon and A. Kahn, *One-dimensional organic nanostructures: A novel approach based on the selective adsorption of organic molecules on silicon nanowires*, Surface Science **602**, L79 (2008).

[77] N. N. Greenwood and A. Earnshaw, *Chemistry of the Elements*, Butterworth-Heinemann, Oxford, 2nd edition, 1997.

[78] Y. Kuk and L. C. Feldman, *Oscillatory relaxation of the Ag(110) surface*, Physical Review B **30**, 5811 (1984).

[79] E. Holub-Krappe, K. Horn, J. Frenken, R. Krans and J. V. D. Veen, *Multi-layer relaxation at the Ag(110) surface*, Surface Science **188**, 335 (1987).

[80] H. Terrones, R. Lv, M. Terrones and M. S. Dresselhaus, *The role of defects and doping in 2D graphene sheets and 1D nanoribbons*, Reports on Progress in Physics **75**, 062501 (2012).

[81] H. Sahaf, F. Dettoni, C. Léandri, E. Moyen, L. Masson and M. Hanbücken, *Self-assembled Si nanostripe grating at the molecular scale as a template for 1D growth*, Surface and Interface Analysis **42**, 687 (2010).

[82] P. Espeter, C. Keutner, P. Roese, K. Shamout, U. Berges and C. Westphal, *Facing the interaction of absorbed silicon nano-ribbons on silver*, Nanotechnology **28**, 455701 (2017).

[83] M. E. Becquerel, *Recherches sur les effets de la radiation chimique de la lumiére solaire, au moyen des courants électriques*, Comptes rendus de l'Académie des sciences **9**, 145 (1839).

[84] M. E. Becquerel, *Mémoire sur les effets électriques produits sous l'influence des rayons solaires*, Comptes rendus de l'Académie des sciences **9**, 561 (1839).

[85] H. Hertz, *Ueber einen Einfluss des ultravioletten Lichtes auf die electrische Entladung*, Annalen der Physik **267**, 983 (1887).

[86] W. Hallwachs, *Ueber die Electrisirung von Metallplatten durch Bestrahlung mit electrischem Licht*, Annalen der Physik **270**, 731 (1888).

[87] W. Hallwachs, *Ueber den Einfluss des Lichtes auf electrostatisch geladene Körper*, Annalen der Physik **269**, 301 (1888).

[88] P. Lenard, *Erzeugung von Kathodenstrahlen durch ultraviolettes Licht*, Annalen der Physik **307**, 359 (1900).

[89] M. Planck, *Ueber irreversible Strahlungsvorgänge*, Annalen der Physik **306**, 69 (1900).

[90] M. Planck, *Ueber das Gesetz der Energieverteilung im Normalspectrum*, Annalen der Physik **309**, 553 (1901).

[91] A. Einstein, *Über einen die Erzeugung und Verwandlung des Lichtes betreffenden heuristischen Gesichtspunkt*, Annalen der Physik **322**, 132 (1905).

[92] R. A. Millikan, *A Direct Photoelectric Determination of Planck's h*, Physical Review **7**, 355 (1916).

[93] F. de Groot and A. Kotani, *Core Level Spectroscopy of Solids*, CRC Press, Boca Raton, 1st edition, 2008.

[94] P. Auger, *Sur l'effet photoélectrique composé*, Journal de Physique et le Radium **6**, 205 (1925).

[95] L. Meitner, *Über die β-Strahl-Spektra und ihren Zusammenhang mit der γ-Strahlung*, Zeitschrift für Physik A Hadrons and Nuclei **11**, 35 (1922).

[96] J. F. W. Herschel, *On a Case of Superficial Colour Presented by a Homogeneous Liquid Internally Colourless*, Philosophical Transactions of the Royal Society of London **135**, 143 (1845).

[97] G. G. Stokes, *On the Change of Refrangibility of Light*, Philosophical Transactions of the Royal Society of London **142**, 463 (1852).

[98] F. Schönbohm, *Temperaturverhalten und Strukturbestimmung dünner Metalloxidschichten auf Siliziumoberflächen*, Dissertation, Technische Universität Dortmund, 2013.

[99] M. P. Seah and W. A. Dench, *Quantitative electron spectroscopy of surfaces: A standard data base for electron inelastic mean free paths in solids*, Surface and Interface Analysis **1**, 2 (1979).

[100] H. Shinotsuka, S. Tanuma, C. J. Powell and D. R. Penn, *Calculations of electron inelastic mean free paths. X. Data for 41 elemental solids over the 50 eV to 200 keV range with the relativistic full Penn algorithm*, Surface and Interface Analysis **47**, 871 (2015).

[101] S. Tanuma, C. J. Powell and D. R. Penn, *Calculations of electron inelastic mean free paths. III. Data for 15 inorganic compounds over the 50–2000 eV range*, Surface and Interface Analysis **17**, 927 (1991).

[102] M. Inokuti, *Inelastic Collisions of Fast Charged Particles with Atoms and Molecules - The Bethe Theory Revisited*, Reviews of Modern Physics **43**, 297 (1971).

[103] J. C. Ashley, *Energy-loss probabilities for electrons, positrons, and protons in condensed matter*, Journal of Applied Physics **69**, 674 (1991).

[104] D. Sarid and W. Challener, *Modern Introduction to Surface Plasmons*, Cambridge University Press, Cambridge New York, 1st edition, 2010.

[105] S. Hofmann, *Auger- and X-Ray Photoelectron Spectroscopy in Materials Science*, Springer, Berlin Heidelberg, 1st edition, 2013.

[106] D. A. Shirley, *High-Resolution X-Ray Photoemission Spectrum of the Valence Bands of Gold*, Physical Review B **5**, 4709 (1972).

[107] S. Tougaard and B. Jørgensen, *Absolute background determination in XPS*, Surface and Interface Analysis **7**, 17 (1985).

[108] S. Tougaard, *Quantitative analysis of the inelastic background in surface electron spectroscopy*, Surface and Interface Analysis **11**, 453 (1988).

[109] S. Tougaard and P. Sigmund, *Influence of elastic and inelastic scattering on energy spectra of electrons emitted from solids*, Physical Review B **25**, 4452 (1982).

[110] R. Hesse, M. Weiß, R. Szargan, P. Streubel and R. Denecke, *Comparative study of the modelling of the spectral background of photoelectron spectra with the Shirley and improved Tougaard methods*, Journal of Electron Spectroscopy and Related Phenomena **186**, 44 (2013).

[111] C. Fadley, Basic Concepts of X-ray Photoelectron Spectroscopy, in *Electron Spectroscopy: Theory, Techniques and Applications*, pages 2–157, Academic Press, London, 1st edition, 1978.

[112] S. Hüfner, *Photoelectron Spectroscopy, Principles and Applications*, Springer, Berlin Heidelberg, 3rd edition, 2003.

[113] S. Doniach and M. Sunjic, *Many-electron singularity in X-ray photoemission and X-ray line spectra from metals*, Journal of Physics C: Solid State Physics **3**, 285 (1970).

[114] S. Hagström, C. Nordling and K. Siegbahn, *Electron spectroscopy for chemical analyses*, Physics Letters **9**, 235 (1964).

[115] G. Ekspong, *Nobel Lectures in Physics, (1981-1990) (Nobel Lectures, Including Presentation Speeches and Laureate)*, World Scientific Publishing Company, Singapore, 1st edition, 1993.

[116] U. Gelius, E. Basilier, S. Svensson, T. Bergmark and K. Siegbahn, *A high resolution ESCA instrument with X-ray monochromator for gases and solids*, Journal of Electron Spectroscopy and Related Phenomena **2**, 405 (1973).

[117] C. Fadley, *X-ray photoelectron spectroscopy: Progress and perspectives*, Journal of Electron Spectroscopy and Related Phenomena **178–179**, 2 (2010).

[118] M. Henzler and W. Göpel, *Oberflächenphysik des Festkörpers*, B. G. Teubner Stuttgart, 1st edition, 1991.

[119] H. Haken and H. C. Wolf, *Atom- und Quantenphysik*, Springer, Berlin Heidelberg, 8th edition, 2004.

[120] S. Dreiner, *Untersuchung von Ober- und Grenzflächen mittels niederenergetischer Photoelektronenbeugung*, Dissertation, Westfälischen Wilhelms-Universität Münster, 2002.

[121] A. M. Ferraria, A. P. Carapeto and A. M. B. do Rego, *X-ray photoelectron spectroscopy: Silver salts revisited*, Vacuum **86**, 1988 (2012).

[122] K. Siegbahn, U. Gelius, H. Siegbahn and E. Olson, *Angular distribution of electrons in ESCA spectra from a single crystal*, Physics Letters A **32**, 221 (1970).

[123] C. Fadley and S. Bergström, *Angular distribution of photoelectrons from a metal single crystal*, Physics Letters A **35**, 375 (1971).

[124] D. P. Woodruff, D. Norman, B. W. Holland, N. V. Smith, H. H. Farrell and M. M. Traum, *Diffraction of Photoelectrons Emitted from Core Levels of Te and Na Atoms Adsorbed on Ni(001)*, Physical Review Letters **41**, 1130 (1978).

[125] S. Kono, C. S. Fadley, N. F. T. Hall and Z. Hussain, *Azimuthal Anisotropy in Deep Core-Level X-Ray Photoemission from an Adsorbed Atom: Oxygen on Copper(001)*, Physical Review Letters **41**, 117 (1978).

[126] S. D. Kevan, D. H. Rosenblatt, D. Denley, B. C. Lu and D. A. Shirley, *Normal Photoelectron Diffraction of the Se* 3*d Level in Se Overlayers on Ni(100)*, Physical Review Letters **41**, 1565 (1978).

[127] C. S. Fadley, *Diffraction and holography with photoelectrons and Auger electrons: some new directions*, Surface Science Reports **19**, 231 (1993).

[128] C. A. Lucas, Surface Structure Determination by Interference Techniques, in *Surface Analysis - The Principal Techniques*, pages 391–478, John Wiley & Sons, Hoboken, 2nd edition, 2009.

[129] A. Liebsch, *Theory of Angular Resolved Photoemission from Adsorbates*, Physical Review Letters **32**, 1203 (1974).

[130] M. Scheffler, K. Kambe and F. Forstmann, *Angle resolved photoemission from adsorbates: Theoretical considerations of polarization effects and symmetry*, Solid State Communications **23**, 789 (1977).

[131] F. J. García de Abajo, M. A. Van Hove and C. S. Fadley, *Multiple scattering of electrons in solids and molecules: A cluster-model approach*, Physical Review B **63**, 075404 (2001).

[132] S. Goldberg, R. Baird, S. Kono, N. Hall and C. Fadley, *Explanation of XPS core-level angular distributions for single-crystal copper by two-beam Kikuchi-band theory*, Journal of Electron Spectroscopy and Related Phenomena **21**, 1 (1980).

[133] S. Nishikawa and S. Kikuchi, *Diffraction of Cathode Rays by Calcite*, Nature **122**, 726 (1928).

[134] S. Nishikawa and S. Kikuchi, *Diffraction of Cathode Rays by Mica*, Nature **121**, 1019 (1928).

[135] W. F. Egelhoff Jr., *X-Ray photoelectron and auger electroo forward scattering: A new tool for surface crystallography*, Critical Reviews in Solid State and Materials Sciences **16**, 213 (1990).

[136] M.-L. Xu, J. J. Barton and M. A. Van Hove, *Electron scattering by atomic chains: Multiple-scattering effects*, Physical Review B **39**, 8275 (1989).

[137] M. Schürmann, *Strukturbestimmung an ultradünnen SiO2-Filmen auf 4H-SiC(0001) mittels Photoelektronenspektroskopie und -beugung*, Dissertation, Technische Universität Dortmund, 2005.

[138] R. Gunnella, F. Solal, D. Sébilleau and C. Natoli, *MSPHD: A full multiple scattering code for low energy photoelectron diffraction*, Computer Physics Communications **132**, 251 (2000).

[139] C. R. Natoli, M. Benfatto, C. Brouder, M. F. R. López and D. L. Foulis, *Multichannel multiple-scattering theory with general potentials*, Physical Review B **42**, 1944 (1990).

[140] A. Gonis and W. H. Butler, *Multiple Scattering in Solids*, Springer, New York, 1st edition, 2000.

[141] J. C. Slater, *Wave Functions in a Periodic Potential*, Physical Review **51**, 846 (1937).

[142] J. Zabloudil, R. Hammerling, L. Szunyogh and P. Weinberger, *Electron Scattering in Solid Matter: A Theoretical and Computational Treatise*, Springer, Berlin New York, 1st edition, 2005.

[143] L. Hedin and B. I. Lundqvist, *Explicit local exchange-correlation potentials*, Journal of Physics C: Solid State Physics **4**, 2064 (1971).

[144] C. Westphal, U. Berges, S. Dreiner, R. Follath, M. Krause, F. Schäfers, D. Schirmer and M. Schürmann, *The plane-grating monochromator beamline at the U55 undulator for surface and interface studies at DELTA*, Journal of Electron Spectroscopy and Related Phenomena **144**, 1117 (2005).

[145] J. B. Pendry, *Reliability factors for LEED calculations*, Journal of Physics C: Solid State Physics **13**, 937 (1980).

[146] K.-M. Schindler, V. Fritzsche, M. C. Asensio, P. Gardner, D. E. Ricken, A. W. Robinson, A. M. Bradshaw, D. P. Woodruff, J. C. Conesa and A. R. González-Elipe, *Structural determination of a molecular adsorbate by photoelectron diffraction: Ammonia on Ni{111}*, Physical Review B **46**, 4836 (1992).

[147] D. P. Woodruff and A. M. Bradshaw, *Adsorbate structure determination on surfaces using photoelectron diffraction*, Reports on Progress in Physics **57**, 1029 (1994).

[148] T. Lühr, *Messung und Simulation von XPD-Mustern der Si(110)/SiO2-Grenzschicht*, Diplomarbeit, Technische Universität Dortmund, 2005.

[149] R. Döll and M. V. Hove, *Global optimization in LEED structure determination using genetic algorithms*, Surface Science **355**, L393 (1996).

[150] C. Flüchter, A. de Siervo, D. Weier, M. Schürmann, A. Beimborn, S. Dreiner, M. Carazzolle, R. Landers, G. Kleiman and C. Westphal, *Structure determination of three-dimensional hafnium silicide nano structures on Si(100) by means of X-ray photoelectron diffraction*, Surface Science **602**, 3647 (2008).

[151] H. Lüth, *Solid Surfaces, Interfaces and Thin Films*, Springer, New York, 5th edition, 2010.

[152] L. Vattuone, M. Rocca, C. Boragno and U. Valbusa, *Initial sticking coefficient of O2 on Ag(110)*, The Journal of Chemical Physics **101**, 713 (1994).

[153] J. T. Yates Jr., *Experimental Innovations in Surface Science: A Guide to Practical Laboratory Methods and Instruments*, Springer, Switzerland, 2nd edition, 2015.

[154] C. Davisson and L. H. Germer, *Diffraction of Electrons by a Crystal of Nickel*, Physical Review **30**, 705 (1927).

[155] E. J. Scheibner, L. H. Germer and C. D. Hartman, *Apparatus for Direct Observation of Low Energy Electron Diffraction Patterns*, Review of Scientific Instruments **31**, 112 (1960).

[156] D. Krull, *Determination of the interface structures of the multilayer system MgO/Fe/GaAs(001) - An x-ray photoelectron spectroscopy and diffraction study*, Dissertation, Technische Universität Dortmund, 2015.

[157] J. B. Pendry, *Low energy electron diffraction*, Academic Press, London, 1st edition, 1974.

[158] G. Held, Low-Energy Electron Diffraction (LEED), in *Surface and Thin Film Analysis*, pages 93–109, Wiley VCH Verlag GmbH & Co. KGaA, Weinheim, 2nd edition, 2011.

[159] D. Briggs and M. Seah, *Practical Surface Analysis by Auger and X-ray Photoelectron Spectroscopy*, John Wiley & Sons, Chichester New York, 1st edition, 1983.

[160] M. Höner, *Investigation of Transient Processes at the DELTA Electron Storage Ring Using a Digital Bunch-by-Bunch Feedback System*, Dissertation, Technische Universität Dortmund, 2015.

[161] U. Berges, C. Sternemann, M. Tolan, C. Westphal, T. Weis and K. Wille, *Status of the Synchrotron Light Source DELTA*, AIP Conference Proceedings **879**, 30 (2007).

[162] K. Wille, *The Physics of Particle Accelerators: An Introduction*, Clarendon Press, Oxford New York, 1st edition, 2000.

[163] U. Berges, M. Krause, M. Schürmann, S. Dreiner, R. Follath, F. Schäfers and C. Westphal, *The PGM Beamline at the Undulator U55 at DELTA*, AIP Conference Proceedings **705**, 424 (2004).

[164] XR 50 X-Ray Source, User manual, SPECS Surface Nano Analysis GmbH, 2015.

[165] J. Leiro, E. Minni and E. Suoninen, *Study of plasmon structure in XPS spectra of silver and gold*, Journal of Physics F: Metal Physics **13**, 215 (1983).

[166] T. Tang, Z. Zhang, Z. Ding and H. Yoshikawa, *Deriving Effective Energy Loss Function for Silver from XPS Spectrum*, Physics Procedia **32**, 165 (2012).

[167] Z. Zengming, T. Koshikawa, T. Iyasu, R. Shimizu and K. Goto, *Comparison of energy-loss functions from REELS spectra with surface and bulk energy loss functions for Ag*, Surface and Interface Analysis **35**, 403 (2003).

[168] M. Rocca, *Low-energy EELS investigation of surface electronic excitations on metals*, Surface Science Reports **22**, 1 (1995).

[169] C. Godet, D. David, H. Sabbah, S. Ababou-Girard and F. Solal, *Bulk and surface plasmon excitations in amorphous carbon measured by core-level photoelectron spectroscopy*, Applied Surface Science **255**, 6598 (2009).

[170] A. C. Simonsen, F. Yubero and S. Tougaard, *Analysis of angle-resolved electron energy loss in XPS spectra of Ag, Au, Co, Cu, Fe and Si*, Surface Science **436**, 149 (1999).

[171] R. G. Coppertwhaite, O. A. Kunze, J. Lloyd, J. A. Neely and W. Tuma, *Surface Analysis of InSb by X-Ray Photoelectron Spectroscopy (XPS)*, Zeitschrift für Naturforschung A **33**, 523 (1978).

[172] A. Goswami and N. D. Lisgarten, *The measurement of inner potentials for copper, silver and gold*, Journal of Physics C: Solid State Physics **15**, 4217 (1982).

[173] M. E. Dávila and G. Le Lay, *Few layer epitaxial germanene: a novel two-dimensional Dirac material*, Scientific Reports **6**, 20714 (2016).

[174] M. R. Tchalala, H. Enriquez, A. J. Mayne, A. Kara, S. Roth, M. G. Silly, A. Bendounan, F. Sirotti, T. Greber, B. Aufray, G. Dujardin, M. A. Ali and H. Oughaddou, *Formation of one-dimensional self-assembled silicon nanoribbons on Au(110)-(2×1)*, Applied Physics Letters **102**, 083107 (2013).

[175] Y. Du, J. Zhuang, J. Wang, Z. Li, H. Liu, J. Zhao, X. Xu, H. Feng, L. Chen, K. Wu, X. Wang and S. X. Dou, *Quasi-freestanding epitaxial silicene on Ag(111) by oxygen intercalation*, Science Advances **2**, e1600067 (2016).

[176] S. Liang, R. Geng, B. Yang, W. Zhao, R. Chandra Subedi, X. Li, X. Han and T. D. Nguyen, *Curvature-enhanced Spin-orbit Coupling and Spinterface Effect in Fullerene-based Spin Valves*, Scientific Reports **6**, 19461 (2016).

[177] P. D. Padova, C. Quaresima, B. Olivieri, P. Perfetti and G. L. Lay, *sp2-like hybridization of silicon valence orbitals in silicene nanoribbons*, Applied Physics Letters **98**, 081909 (2011).

[178] L. Tao, E. Cinquanta, D. Chiappe, C. Grazianetti, M. Fanciulli, M. Dubey, A. Molle and D. Akinwande, *Silicene field-effect transistors operating at room temperature*, Nature Nanotechnology **10**, 227 (2015).

Publications

Articles

[A1] P. Roese, C. Keutner, U. Berges, P. Espeter, and C. Westphal, *Photoemission Electron Microscopy as a Tool for Studying Steel Grains*, Metallurgical and Materials Transactions A **48**, 1484 (2017)

[A2] C. Keutner, A. von Bohlen, U. Berges, P. Espeter, D.J. Keavney, C.M. Schneider, and C. Westphal, *Photoemission electron microscopy and scanning electron microscopy of Magnetospirillum magnetotacticum's magnetosome chains*, Analytical Chemistry **86**, 9590 (2014)

[A3] P. Espeter, C. Keutner, P. Roese, K. Shamout, U. Berges, and C. Westphal, *Facing the interaction of absorbed silicon nano-ribbons on silver*, Nanotechnology **28**, 455701 (2017)

[A4] K. Shamout, P. Espeter, P. Roese, U. Berges, and C. Westphal, *Revealing the interfaces of the hybrid system MgO/Co/GaAs(001): A structural and chemical investigation by photoelectron spectroscopy and diffraction*, (submitted)

Conference contributions

[C1] P. Espeter, D. Handschak, C. Keutner, P. Roese, U. Berges, and C. Westphal, *XPS study of mecanical exfoliated molybdenum disulphide*, DPG-Frühjahrstagung, Berlin, 2015

[C1] C. Keutner, A. von Bohlen, U. Berges, P. Espeter, C. M. Schneider and C. Westphal, *Insight into bacteria: magnetosomes chains under photoemission electron and scanning electron microscopes*, NSTI-Nanontech, Washington, 2015

[C1] P. Espeter, S. Döring, M. Eschbach, M. Gehlmann, C. Keutner, C. Kohlmann, D. Krull, L. Plucinski, U. Berges, C. M. Schneider, and C. Westphal, *A XPS/XPD study of the topological insulator BiTe*, DPG-Frühjahrstagung, Regensburg, 2016

[C1] P. Espeter, C. Keutner, F. Kleimeier, P. Roese, K. Shamout, G. Wenzel, U. Berges, H. Zacharias and C. Westphal, *Structure determination of Si on Ag(110)*, nanomat 2D-Materials, Dübendorf, 2016

[C1] P. Espeter, C. Keutner, N. F. Kleimeier, P. Roese, K. Shamout, G. Wenzel, U. Berges, H. Zacharias, and C. Westphal, *Structure determination of silicon nano-ribbons on Ag(110)*, DPG-Frühjahrstagung, Dresden, 2017

[C1] P. Espeter, C. Keutner, N. F. Kleimeier, P. Roese, K. Shamout, G. Wenzel, U. Berges, H. Zacharias, and C. Westphal, *Structure determination of silicene nanoribbons on Ag(110)*, NSTI-Nanotech, Washington, 2017

[C1] P. Espeter, C. Keutner, N. F. Kleimeier, P. Roese, K. Shamout, G. Wenzel, U. Berges, H. Zacharias, and C. Westphal, *Atomic Structure of Silicon Nano-Ribbons*, ICMAT, Singapur, 2017

Danksagung

Ganz besonders möchte ich mich an dieser Stelle bei Prof. Dr. Carsten Westphal bedanken für das Ermöglichen dieser Dissertation. Für die wertvollen Anregungen und konstruktiven Diskussionen möchte ich mich herzlich bedanken.

Außerdem möchte ich mich bei Prof. Dr. Dr. Wolfgang Rhode bedanken für das Übernehmen des Zweitgutachtens für diese Dissertation.

Bei der gesamten Arbeitsgruppe E1b bedanke ich mich für die produktive wie angenehme Zusammenarbeit im Büro sowie im Labor und ebenso für die anregenden und kritischen Fragen rund um diese Arbeit. Ein beonderes Dankeschön geht dabei an Peter und Karim aus unserem XPS-Büro, in dem wir viele wissenschaftliche und manchmal auch unwissenschaftliche Fragestellungen klären konnten. Außerdem danke ich Christoph und Ulf, die mir bei vielen physikalischen sowie technischen Fragestellungen eine große Hilfe waren.

Mein Dank gilt außerdem Dirk Schemionek und Gisela Pike für das Läppen, Orientieren und Polieren von nicht nur einem Silberkristall.

Bei dem Personal von DELTA möchte ich mich für jedes einzelne zur Verfügung gestellte Photon bedanken.

Meiner Familie und meinen Freunden möchte ich Dank sagen für eben jene Zeit, die ich mit ihnen anstatt mit der Physik verbringen konnte.
Mein besonderer Dank geht an meine Frau Nina, die immer an meiner Seite ist und mich auch in schwierigen Zeiten aufbaut und ermutigt weiterzumachen.